Dissertation
submitted to the
Combined Faculty of Natural Sciences and Mathematics
of the Ruperto Carola University Heidelberg, Germany
for the degree of
Doctor of Natural Sciences

Presented by
M.Sc. Dimitri Kromm
born in: Novosibirsk, Russian Federation
Oral examination: 17.12.2021

Pushing Light-Sheet Microscopy to Greater Depths

Referees: Prof. Dr. Joachim Wittbrodt

Dr. Robert Prevedel

Abstract

Light-sheet fluorescence microscopy (LSFM) has established itself as an irreplaceable imaging technique in developmental biology over the past two decades. With its emergence, the extended recording of *in toto* datasets of developing organisms across scales became possible. Remarkably, LSFM opened the door to new spatio-temporal domains in biology, offering cellular resolution on the one hand, and temporal resolution on the order of seconds on the other hand. As in any fluorescence microscopy technique, LSFM is also affected by image degradation at greater tissue depths. Thus far, this has been addressed by the suppression of scattered light, use of fluorophores emitting in the far red spectrum, multi-view detection and fusion, adaptive optics, as well as different illumination schemes. In this work, I investigate for the first time *in vivo* optical aberration reduction via refractive index matching in LSFM. Examples are shown on common model organisms as *Arabidopsis thalina*, *Oryzias latipes*, *Mus musculus*, as well as *Drosophila*. Additionally, I present a novel open-top light-sheet microscope, tailored for high-throughput imaging of mammalian samples, such as early stage mouse embryos. It is based on a three objective geometry, encompassing two opposing detection objective lenses with high light collection efficiency, and an invertedly mounted illumination lens. It bridges the spatial scale between samples by employing an extendible light-sheet illumination via a tunable acoustic gradient index lens. Both parts of this work improve the image quality across the 3D volume of specimens, paving the way for more quantitative recordings at greater tissue depths.

Zusammenfassung

Lichtblatt-Fluoreszenzmikrosopie (LSFM, vom Englischen) hat sich in den letzten beiden Jahrzehnten als essentielle Technik zur Bildgebung in der Entwicklungsbiologie etabliert. Mit ihrer Existenz sind ausgedehnte, sowie Skalen überbrückende *in toto* Aufnahmen von sich entwickelnden Organismen möglich geworden. Bemerkenswerterweise hat LSFM die Tür für eine neue raum-zeitliche Domäne in der Biologie geöffnet, indem sie einerseits zelluläre Auflösung, und andererseits zeitliche Auflösung im Sekundenbereich bietet. So wie jede Fluoreszenzmikroskopie-Technik, ist auch LSFM von einer Bildverschlechterung in größeren Gewebstiefen betroffen. Bisher wurde dies durch Unterdrücken von Streulicht, Verwendung von Fluorophoren, die im nahinfraroten Spektrum emittieren, Detektion von verschiedenen Seiten und anschließender Daten-Fusion, adaptiver Optik und verschiedenen Beleuchtungsstrategien adressiert. In dieser Arbeit, untersuche ich zum ersten Mal die *in vivo* Verringerung von optischen Aberrationen mittels Brechungsindex-Anpassung in LSFM. Es werden Beispiele an üblichen Modellorganismen wie *Arabidopsis thaliana*, *Oryzias latipes*, *Mus musculus*, sowie *Drosophila melanogaster* gezeigt. Zusätzlich präsentiere ich ein neuartiges, nach oben geöffnetes Lichtblatt-Mikroskop, das speziell für Hochdurchsatz-Aufnahmen von Säugetier-Proben, wie z.B. frühen Mausembryonen, zugeschnitten ist. Es basiert auf der Geometrie dreier zueinander angeordneter Objektive, bestehend aus zwei gegenüberliegenden Detektions-Objektiven mit einer hohen Lichtaufnahme-Effizienz, sowie einer invertiert montierten Beleuchtungslinse. Das Mikroskop überbrückt die räumliche Skala zwischen unterschiedlichen Proben, indem es eine ausdehnbare Lichtblatt-Beleuchtung mittels einer steuerbaren akustischen Gradientenindex-Linse verwendet. Beide Teile dieser Arbeit verbessern die Bildqualität in den aufgenommenen 3D Volumen der Proben, und ebnen damit den Weg zu quantitativeren Aufnahmen in größeren Gewebstiefen.

Contents

List of Figures

List of Abbreviations

In most instances abbreviations are introduced where they first appear in this work, but to aid the reader a short list of the most important abbreviations is presented here.

2D	two dimensional
3D	three dimensional
BFP	back focal plane
BPM	beam propagation method
CCD	charge coupled device
CLSM	confocal laser scanning microscopy
CMOS	complementary metal oxide semiconductor
DCT	discrete cosine transform
DFT	discrete Fourier transform
DSLM	digitally scanned light-sheet microscopy
eCSD	electronic confocal slit detection
FEP	fluorinated ethylene propylene
FN	field number
FOV	field of view
FPGA	field programmable gate array
fps	frames per second
FWHM	full width at half maximum
GVS	galvanometric scan mirror
GFP	green fluorescent protein
GPU	graphics processing unit
LSFM	light-sheet fluorescence microscopy
MuVi-SPIM	Multiview SPIM

NA	numerical aperture
OTF	optical transfer function
PEEK	polyether ether ketone
PSF	point spread function
PBS	phosphate-buffered saline
RI	refractive index
RESOLFT	reversible saturable optical fluorescence transitions
ROI	region of interest
sCMOS	scientific CMOS
SMLM	single molecule localization microscopy
SNR	signal to noise ratio
SPIM	single plane illumination microscope
STED	stimulated Emission Depletion
TAG	tunable accoustic gradient

1 Introduction

Who has not spent some time during a clear night, staring at the night sky, stargazing and simply wondering? Modern humans and likely our ancestors have been doing so for hundreds of thousands of years before us. Nature itself made this possible by equipping us with a powerful optical system: our pair of eyes. Of course our fascination with the universe never stopped, and from observing planets, suns, and galaxies with our naked eye, we humans went on to operate telescopes in space and even sent drones and vehicles to other planets. Somewhat in the shadow, on the dark side of the moon so to speak, a different curiosity of humans started to rise: the interest in the small things in life. Beyond what our eyes can naturally detect, a full micro-cosmos was hidden from us. Today, starting with single cells, their organelles, viruses, proteins, molecules, and even atoms, we have managed to observe and record the whole repertoire of life's building blocks. This achievement rests on the shoulders of the telescope's smaller cousin: the microscope, and all if its recent developments. With the current advancements in technology we are reaching an age, where in parallel to the opening question, we may ask: Who has not spent some time looking at life under the microscope, '*cellgazing*'?

The microscope's journey in enriching our knowledge about the micro-cosmos started in the 17^{th} century with Robert Hooke who identified cells [1], and Antoni van Leeuwenhoek who for the first time observed bacteria [2]. This time marked the dawn of microbiology and enabled studies of previously unseen life processes. Apart from technical limitations, the diffractive nature of electro-magnetic waves, such as visible light, presented a clear boundary to the microscopes' resolution limit. This fundamental limitation to approximately half the wavelength of the detected light was first formulated by Ernst Abbe in 1873 [3]. Thus, ever shorter wavelengths found their application in microscopy, leading to ultraviolet [4] and X-ray microscopy [5]. But not only photons were used to interact with biological samples in the hunt for higher resolution. Electron microscopy, developed in 1931 [6], became a prominent tool that lead us to resolve structures down to the Ångström level.

However, despite reaching ever higher spatial resolution, advances in the resolution of biol-

ogy's temporal domain were lagging. This is either due to the needed sample preparation in electron microscopy, *e.g.* coating for scanning electron microscopy, the required vacuum, or simply the high power electro-magnetic waves which deposit lethal energy dosages in the sample. Therefore, light-microscopy remained the method of choice to study dynamic processes in cells and organisms.

Light-microscopy however, remained mostly two dimensional due to a lack of optical sectioning capabilities. Nonetheless, it profited from a number of technological advancements, starting with improved manufacturing techniques, the invention of the laser - a coherent light source [7], the discovery of fluorescent proteins [8], and the ever growing palette of genetic tools, *e.g.* the CRISPR-Cas9 gene editing [9][10], as well as the advancement in camera technology backed by a consumer market. These and other developments propelled the capabilities of modern microscopes and possibilities to study biological samples to a new level. An important milestone belongs to the invention of the confocal scanning microscope, a point scanning system including a pinhole for out of focus light discrimination [11]. It enabled researchers to finally record optically sectioned 3D data sets near Abbe's resolution limit. Around the turn of the millennium, another milestone was reached, when two different fluorescence light-microscopy techniques surpassed Abbe's limit with the use of special photo-convertible dyes [12][13]. Primarily these techniques are applied to single fixed cells, and help to study structures and protein-protein interactions, as well as identify protein locations within the cell's subvolume with precisions below 10 nm.

A third milestone was reached in 2004, with the introduction of selective plane illumination microscopy (SPIM) to biology [14]. For the first time, a microscopy technique was used to record extended 3D datasets of developing organism with previously unknown spatio-temporal resolution. While other microscopy techniques were focussing on spatial resolution improvements throughout the years, SPIM closed the gap on the temporal scale. In this microscopy technique, the authors applied a previously reported [15] orthogonal illumination scheme with a thin sheet of light. Such a light-sheet optically sections the live sample, only illuminating it in one plane. Modern light-sheet fluorescence microscopy (LSFM), an alternative name for SPIM, found its application in developmental biology [16][17] and soon after into classical cell biology [18][19], and now spans across a multitude of studies [20][21][22]. Its main advantages over scanning microscopes is the far superior speed and higher photon efficiency: Due to the quasi-instantaneous illumination of an entire plane and its simultaneous detection, the rather slow scanning process is omitted. Further, the otherwise necessary light-cone, entering and exiting

the sample near the focus of the scanned focus, does not exist in light-sheet microscopy. This reduces the light-dosage for standard samples, such as developing embryos, 100 to 1000-fold [16]. Despite the many advantages, light-sheet microscopy also harbours its own challenges, many stemming from the fact that the samples are comparatively large ($> 100\,\mu$m) and their optical properties can vary in space and time.

To this day, only a handful of studies around LSFM addressed the optical properties of the samples, and their refractive index distribution which causes optical aberrations on the illumination, but also on the detection side. The negative influence on contrast and resolution can inhibit quantitative readouts as the optically aberrated signal needs to be carefully compared to the less aberrated, *e.g.* on the surface of the sample.

A promising solution is presented by adaptive optics (AO), originally developed for telescopes in astronomy [23][24]. In this technique an adaptive optical element corrects for irregularities of the light, after interacting with the sample, to re-establish a diffraction limited focus. This approach is rather complicated in microscopy, requires a large budget and is not implementable on many commercial systems. An alternative and not mutually exclusive approach to reduce aberrations, is given by refractive index matching, usually applied for fixed samples. It can however, with limitations, also be applied for live microscopy [25] and reduce imaging artefacts.

Additionally, the concept of multi-view imaging [26][27][28] in light-sheet microscopy is a possible approach to compensate for signal deterioration at larger depths. In this approach the sample is recorded from multiple directions, either simultaneously by at least two detection objective lenses, or via sample rotation and recording from a different angle. Computational post-processing then generates a more isotropically resolved dataset.

This work

This thesis presents a first study of live refractive index matching in light-sheet microscopy to reduce optical aberrations and restore image contrast at greater tissue depths. Further, a novel light-sheet microscope for mammalian multi-sample imaging, based on a thus far unexplored objective arrangement in high throughput light-sheet microscopy, will be presented. The *de novo* imaging system employs a second detection lens, therefore doubling the light collection efficiency. The second detection lens is also used to compensate the opposing objective's signal loss and image quality degradation at larger imaging depths. The system also offers flexibility around the sample size, which is supported by a rearrangable dual-color detection path, as well as a tunable light-sheet profile.
These two topics share a common aim, which is to advance live light-sheet microscopy to greater depths, in the spatial and quantitative context.

Structure

This work is structures as follows:

Chapter 1 introduces the reader to the context of this work and outlines its aims.

Fluorescence microscopy will be introduced in the 2nd chapter, where I highlight its important concepts as well as different imaging approaches. The second half of this chapter focusses on light-sheet fluorescence microscopy and lays the basis for the subsequent chapters.

Chapter 3 will discuss the concept of refractive index matching in SPIM, show theoretical predictions which are backed up by experiments with phantom samples, as well as recordings in *Drosophila melanogaster*, *Arabidopsis thaliana*, *Oryzias latipes*, and *Mus musculus*. The 4th chapter presents the novel high-throughput light-sheet fluorescence microscope for mammalian samples. It discusses the creation and theoretical advantages of flexible, extended *'pushed'* light-sheets. Simulations and experimental results around the light-sheets are presented. Further the advantage of the dual detection scheme for mammalian samples, is exemplified.

2 Fluorescence Microscopy

Today, fluorescence microscopy is a well established tool in the field of life sciences, benefiting from our capabilities to label specific proteins of interest. Its foundations were laid in beginning of the 20th century, before specific labeling with dyes and fluorophores was available, when between 1908 and 1911 August Köhler, Henry Wilhelm Siedentopf, Heinrich Lehmann, and Otto Heimstädt developed the first fluorescence microscopes based on UV-excitation [29][30]. Immunofluorescene, discovered in the early 1940s by Albert Coons [31], allowed scientist to perform targeted fluorescent labelling. Another milestone was reached in the 1960s when Osamu Shimomura isolated the *Green Fluorescent Protein* (GFP) [8]. A few decades later biologists where able to express GFP in other organisms [32][33], therefore opening the door for specific labelling.

The process of fluorescence itself can be best described with the particle view of photons. Light of wavelength λ consists of photons with energy

$$E = h\nu = h\frac{c}{\lambda} \tag{2.1}$$

Here, h is the Planck constant, ν is the light's frequency, and c the speed of light. Before dyes, fluorophores or other materials can emit fluorescence, energy needs to be provided extrinsically, *e.g.* via the excitation by a light source. In this case, excitation photons with energy E are absorbed by an electron, usually in its ground state. It is lifted to a excited state at which it only resides for a matter of ns before it releases its surplus in energy and falls back to its ground state. This surplus of energy E' is transported off by an emitted photon of wavelength $\lambda' = hc/E'$. These photons make up the detectable fluorescence. Typically, the materials' emitted wavelength range is shifted to the red (less energy) compared to the excitation light. This so-called *Stokes shift* lies in the range of at least a few nm (*cf.* Fig. 2.1). Apart from the transition from ground to excited state and vice versa, there can additionally be vibrational states present. Because of their existence, excitation can occur with wavelengths below and above the ideal excitation

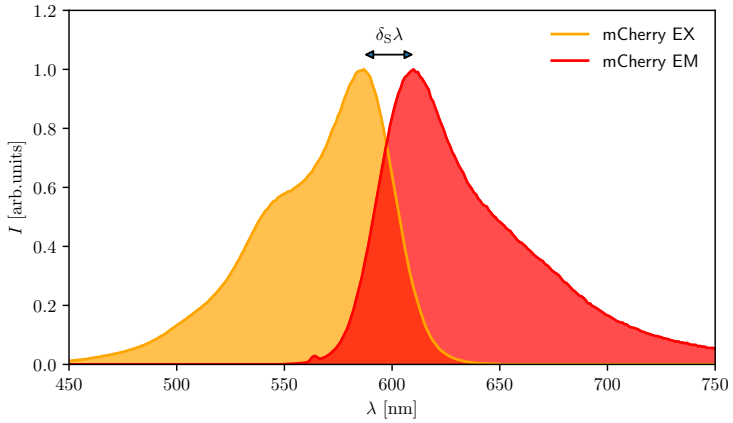

Figure 2.1: Fluorescence Spectra of mCherry. A typical absorption (yellow) and emission (red) spectrum is plotted for the fluorescent protein *mCherry*. Its absorption peak lies at 587 nm whereas the emission peak is shifted to 610 nm. The distance labeled as $\delta_S\lambda$ between the two peaks is the so-called *Stokes Shift*. The spectra were accessed from *FPbase* [35], originally published by Shaner et al. [36].

wavelength. Emitted photons then typically exhibit higher wavelengths, or lower energy. These processes around the electronic states of an atom or molecule can be summarized in a so-called Jablonski diagram [34]. The excitation and emission wavelengths of a fluorescent molecule are typically described via a spectrum, and the molecule's excitation and emission peaks are determined. These spectra are known as the absorption spectrum and the emission spectrum of a dye or fluorophore.

The existence of the Stokes shift allows for the use of fluorescence filter, which block or reflect light used for excitation while transmitting or reflecting light from the emitting fluorophores.

Ideally, a fluorophore cycles back and forth between an excited state and the ground state by emitting photons which make up the total fluorescence. An excited electron in the fluorophore has however the possibility to also change its spin. Should this occur, the probability or relaxation to the original ground state is strongly decreased. This results in a longer life-time in the excited state ($\geq \mu$s compared to ns). In this excited orbit, the electron has a higher probability of being excited into even higher states by absorbing other photons. Photochemical reactions become more likely in which bleaching or phototoxicity can be the end result [37]. Such processes are to be avoided in live imaging as they can destroy the fluorophore, and harm the sample. This effectively means, that with a finite amount of fluorophores or dyes present in a live sample, an excitation photon budget exists. Upon surpassing of this budget, damage in the sample and

signal degradation due to bleaching are the consequence.

2.1 Widefield Microscopy

The simplest fluorescence microscope, a *widefield microscope*, also known as an *epifluorescence microscope*, uses one objective lens to illuminate the specimen and to collect emitted light at the same time (*cf.* Fig. 2.2). Normally, a wavelength band of the excitation light, from a laser or a light source with a broad spectrum, is selected for spectrally with the help of a filter. The light of selected spectrum is then reflected by a dichroic mirror[1] towards the objective. For a homogeneous illumination of the sample, the light is focussed into the back focal plane of the objective. Photons emitted after fluorescent excitation are collected by the objective lens and pass the dichroic mirror. A tube lens in combination with a detector are used to generate an image.

The optical properties of such a microscope depend mostly on the opening angle of the detection objective lens (2α, *cf.* Fig. 2.2) and the light's vacuum wavelength (λ_0). As a rule of thumb one can say that the lateral resolving power of such a microscope lies in the range of the used wavelength (*cf.* Ch. 2.2). Next to the opening angle, the refractive index of the immersion medium n contributes to the light collection efficiency and ergo, can affect the resolution as well. A helpful measure to describe an objective's optical properties is therefore the *numerical aperture*:

$$\mathrm{NA} = n \sin \alpha \tag{2.2}$$

Higher numerical apertures allow to collect light from larger angles and therefore more light in total. The magnification of the system is given by the proportion of the focal lengths of the objective lens and the used tube lens:

$$M = \frac{f_{\mathrm{TL}}}{f_{\mathrm{obj}}}$$

As the entire FOV is flooded with excitation light, widefield microscopy best performs for thinner samples, as less signal from volumes away from the focal plane contribute to the overall

[1] Essentially, a dichroic mirror can also be seen as a filter, characterized by the wavelengths it reflects rather than the ones it lets pass.

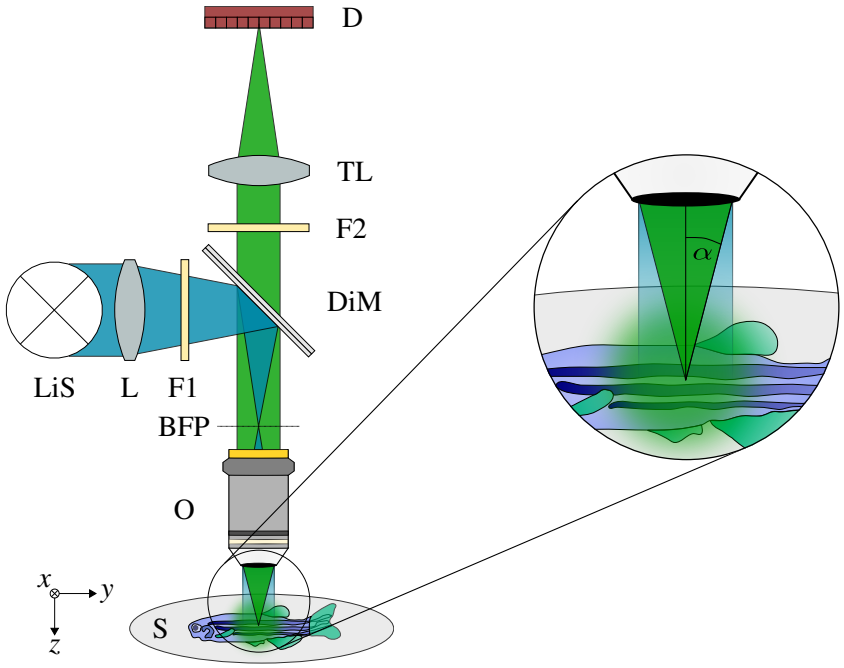

Figure 2.2: Sketch of a widefield fluorescence microscope. In epifluorescence microscopy the sample can be excited with different light-sources (LiS), e.g. a broadband gas-arc lamp. The excitation light is typically expanded and collimated (not shown) before it is focused via a lens (L) onto the back focal plane (BFP) of the objective (O). An excitation Filter (F1) is used to select the desired illumination spectrum. The dichroic mirror (DiM) reflects the light towards the objective where it is focused into the specimen (S). The fluorescence emitted from the sample is collected by the objective with a maximum detection angle of 2α (*cf.* inset zoom on the right). In the form of a detection beam, the fluorescence passes the DiM and an additional detection filter (F2) before it becomes focussed onto the area detector, e.g. CMOS camera, where the image is formed (image plane). Note that only one point was selected to illustrate the image formation. As the illumination is homogeneous across the field of view, one needs to imagine a great number of such cones being collected by the objective simultaneously, from the plane of the objective's focus, from above and from bellow. Further, the here shown BFP outside of the objective housing is only an illustration as in many objectives it is found inside the housing. Adapted in parts from [38].

detected fluorescence. Therefore, no meaningful optical sectioning is performed with the widefield microscope, and 3D reconstructions of the imaged volume will appear blurred out in the z-dimension. The fast readout of the area detector and the simultenously fully illuminated FOV allow for rapid recordings on the other hand.

The following section will introduce the concept of resolution before discussing a microscope system which in contrast excels at providing optically sectioned 3D volumes.

2.2 Point Spread Function and Optical Resolution

When observing a point like object, e.g. a light emitting flourophore or a distant star, with an optical system as our eyes, a microscope or a telescope, that system will generate a blurred, spread out image of this object. This is due to the diffraction of light propagating through an opening such as an iris or lens. This spread is called *point spread function* (PSF) and defines the optical performance of an imaging system. The intensity distribution $I(\boldsymbol{r})$ of an object with coordinate $\boldsymbol{r}$ detected by the observer can be described mathematically through a convolution with the PSF $H(\boldsymbol{r})$:

$$I(\boldsymbol{r}) = O(\boldsymbol{r}) * H(\boldsymbol{r}) \tag{2.3}$$

Note that the PSF can vary across different coordinates and therefore the dependence on $\boldsymbol{r}$ is included above. The PSF's shape and extent further define the optical resolution as will be illustrated below. It is therefore important to understand the limitations of the PSF as it defines what can be observed with a microscope. Following the scalar diffraction theory (polarization ignored) as summarized by *Born and Wolf* [39, p. 484 *ff.*] of a point being imaged by a lens, the lens generates the following intensity PSF at magnification $M = 1$ (*cf.* also [40, p. 23 *f.*])

$$H(u, v) = C_0 \left| \int_0^1 J_0(v\rho) \exp\left(-\frac{1}{2} \mathrm{i} u \rho^2\right) \rho \, d\rho \right|^2 \tag{2.4}$$

with the dimensionless *optical coordinates*

$$u = \frac{8\pi}{\lambda_0} n z \sin^2\left(\frac{\alpha}{2}\right) \tag{2.5}$$

and

$$v = \frac{2\pi}{\lambda} n \rho \sin\alpha \tag{2.6}$$

Here, C_0 is a normalization factor for unity, J_0 is the zero order Bessel function, ρ is the radial coordinate with $\rho = \sqrt{x^2 + y^2}$. With the 3D intensity distribution around the focus, it is now possible to investigate the cross-sectional profiles along the radial coordinate and along z. In the

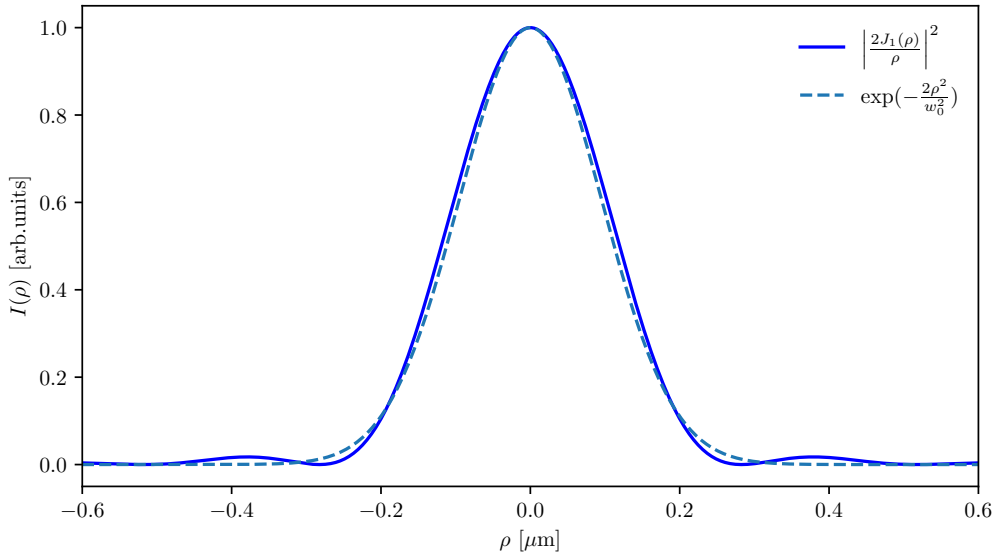

Figure 2.3: Radial Airy pattern. An example Airy disk as described by Eq. 2.8 is plotted here for $\lambda_0 = 510\,\text{nm}$, NA = 1.1 (solid line). Note the minor rise in the function beyond the first minimum. This results in a low intensity ring in the image plane. Additionally, a Gaussian approximation is plotted (dotted line). The approximation was made by letting both function intersect at $1/e^{-2}$ intensity. with $w_0 = 0.19\,\mu\text{m}$.

image plane ($z = u = 0$) the intensity PSF becomes

$$H(u = 0, v) = C_0 \left| \int_0^1 J_0(v\rho)\rho \, d\rho \right|^2 \tag{2.7}$$

$$= I_0 \left(\frac{2J_1(v)}{v} \right)^2 \tag{2.8}$$

with J_1 being the 1st order Bessel function and $I_0 = H(0, 0)$ is the intensity at the geometrical focus.

The intensity distribution follows one main central peak with concentric side rings of ever lower intensities at larger radii. It is known as the *Airy pattern* or *Airy disk*, first described by Airy in 1835 [41]. Its first minimum occurs at $v = 3.83$. Solving Eq. 2.6 for ρ and using

$\mathrm{NA} = n \sin\alpha$, we get

$$\rho\Big|_{H(0,\,3.83)} = \frac{3.83}{2\pi}\frac{\lambda_0}{\mathrm{NA}} \tag{2.9}$$

$$= 0.61\frac{\lambda_0}{\mathrm{NA}} =: \delta_{xy,\,\mathrm{Rayleigh}} \tag{2.10}$$

Analogously, we can proceed to calculate the axial extent to the intensity PSF by setting $\nu = 0$ (*cf.* [39, 490 *f.*]:

$$H(u, \nu = 0) = I_0\left(\frac{\sin u/4}{u/4}\right)^2 \tag{2.11}$$

This PSF function is proportional to $(\sin(x)/x)^2$ and has its first zero for $u/4 = \pm\pi$ at (using Eq. 2.6 & $\sin(\alpha/2) \approx 1/2\sin(\alpha)$ for small angles)

$$z\Big|_{H(\pm 4\pi,\,0)} = \pm\frac{2\lambda_0}{n\sin^2(\alpha)} \tag{2.12}$$

$$= \pm\frac{2\lambda_0 n}{\mathrm{NA}^2} =: \delta_{z,\,\mathrm{Rayleigh}} \tag{2.13}$$

A set of different measures exists throughout the literature on how to define resolution. But generally it is the ability to distinguish two points in close proximity to each from each other. In Eqs. 2.10 and 2.13 the definitions for the lateral and axial resolutions according to the *Rayleigh criterion* [42] have already been indicated. The definitions state that two points with intensity spreads following the above described intensity distributions can be distinguished from one another, if the intensity peak of one point is at least as far away the second point's first intensity minimum. Interestingly, Ernst Abbe was the first to report on the resolution limit achievable with light microscopy in 1873 [3], but without having followed the here presented mathematical derivations. He found that the minimum distance at which two points can be distinguished from one another follows:

$$\delta_{xy,\,\mathrm{Abbe}} = \frac{\lambda}{n \cdot \sin\alpha} \tag{2.14}$$

Apart from a prefactor, this equals Eq. 2.10. Throughout this work, as more commonly used

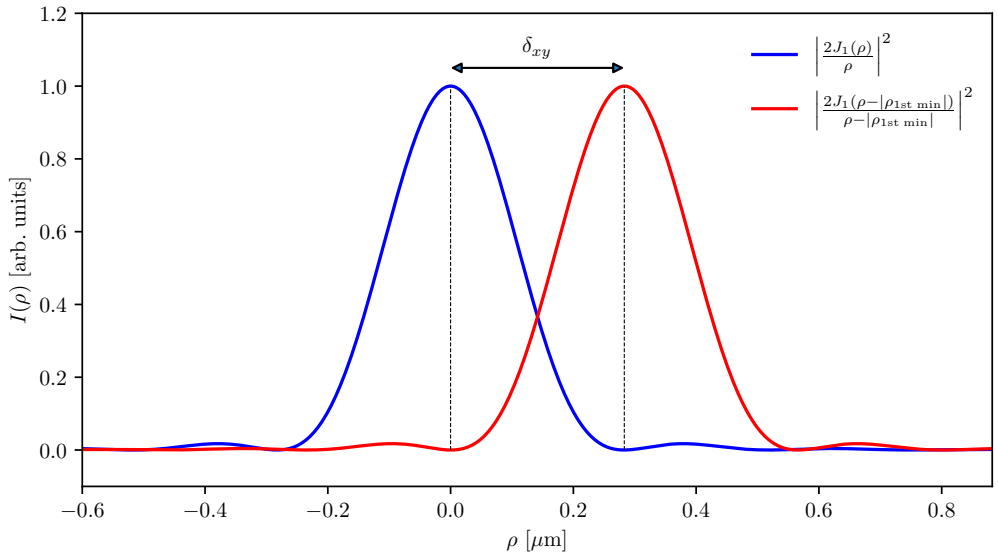

Figure 2.4: Rayleigh Resolution Criterion. The graph shows two Airy disks as in Fig. 2.3, with one pattern being displaced by the distance of the first minimum ($\rho_{1\text{st min}}$) from the central peak. This results in the peak of one function overlapping with the first minimum of the other pattern. As the two peaks can be well distinguished from one another, this is a usefull definition of resolution δ_{xy} and is known as the *Rayleigh criterion* (*cf.* Eq. 2.10 & Eq. 2.15).

today, the resolution limit as defined with Rayleigh criterion will be used. We will refer to the lateral resolution δ_{xy} and the axial resolution δ_z of an optical system, e.g. an objective lens, with the help of

$$\delta_{xy} = 0.61 \frac{\lambda_0}{\text{NA}} \tag{2.15}$$

$$\delta_z = 2 \frac{n\lambda_0}{\text{NA}^2} \tag{2.16}$$

As can be seen from Eqs. 2.15 & 2.16, the lateral and axial resolution depend differently on the numerical aperture, and therefore on the angle α. Their behaviour for smaller and larger NAs, as well as the changing ratio between them is shown in Fig. 2.5 (a) & (b).

The axial resolution is always lower than the lateral resolution, typically by a factor of $\sim$ 4-9 for detection objectives used in this work. Especially for objectives of lower numerical aperture, these formulas provide a good estimate. A more precise treatment of the resolution for high angle objective lenses, based on the uncertainty principle of electromagnetic waves, can be found in [43].

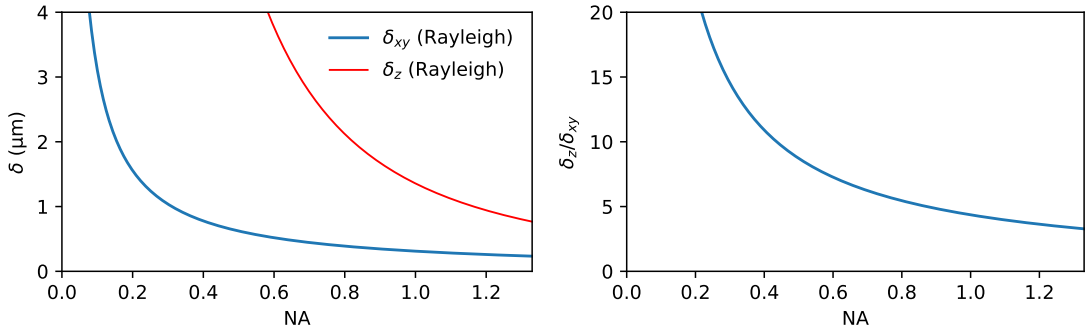

(a) (b)

Figure 2.5: Optical resolution of a widefield microscope. Plot (a) shows the lateral (δ_{xy}) and the axial (δ_z) resolutions defined by Eqs. 2.15 & 2.16 for a widefield microscope in dependence of the numerical aperture NA = $n \sin(\alpha)$. The axial resolution is always worse than the lateral resolution. Higher numerical apertures improve the axial resolution stronger than the lateral resolution which is illustrated by the ratio between the two (δ_z/δ_{xy}) in (b). For calculations, a wavelength of $\lambda_0 = 510\,\text{nm}$ and a refractive index $n = 1.33$ were chosen.

Above, we have assumed an emitting point being imaged by a perfect thin lens to find the best possible performance of a microscope. For fluorescence microscopy however, the illumination and detection PSFs (H_{ill} & H_{det}) can be different, e.g. because of different wavelengths or because of different NAs. The probability to detect a photon from the illuminated point in the sample, depends on the probability of an illumination photon reaching the point as well as the probability of an emitted photon from that point to reach the detector. Therefore the system's intensity PSF (H_{sys}) can analogously be expressed as a multiplication of the two intensity PSFs:

$$H_{\text{sys}} = H_{\text{ill}} \cdot H_{\text{det}} \tag{2.17}$$

Reducing one of the two PSFs will result in a reduction in the total PSF, which in turn improves the resolution. The following section will introduce one such concept based on one objective alone before moving on to the concept of decoupled illumination and detection in light-sheet microscopy. The choice of optical components, their possible misalignment as well as sample and medium induced aberrations all can negatively impact the PSF and therefore reduce the resolution capabilities of a microscope. More information about optical aberrations and their minimization can be found in Ch. 3.

2.3 Confocal Microscopy

In the above described widefield microscope setup, the desired FOV is illuminated approximately evenly by a collimated beam with the help of the objective. Fluorophores are excited along the entire three dimensional illumination profile and therefore fluorescence is detected from planes above and below the focal plane of the objective, leading to blur and background signal in the detected image. One effective way to suppress photons from the out-of-focus planes to reach the detector, is the use of a pinhole at the focus of the tube lens. Photons that were emitted below or above the focal plane pass the objective under different angles and reach the image plane at different positions where they are then blocked by the pinhole aperture. A detected spot of higher contrast is the result. However, as the fluorophores from the proximity of the detected spot are also affected by the aperture, widefield illumination is not further feasible. Instead a point like illumination is more efficient. To then generate an image the sample requires scanning by such an excitation spot. Theoretically this can be done mechanically by displacing the sample, but a faster and more efficient way to limit the mechanical movement to the direction of the optical axis, is to instead scan the spot with optical elements, such as galvanometric scan mirrors (GSMs) in the focal plane. Further, an area detector is no longer required and instead a photo-multiplier is used. Finally, to ensure positional stability in the image plane and optimal usage of the pinhole, the emitted fluorescence is descanned with the same scanning elements that are employed in the illumination, e.g. a pair of GSMs. The result is an optically sectioned image from a single plane spanning the axial extent of the PSF. For 3D acquisitions the sample is displaced in z, the optical axis of the objective lens. This sort of setup is called a *confocal laser scanning microscope* (CLSM) (*cf.* Fig. 2.6). To increase imaging speed, spinning-disk microscopes use an array of pinholes that move at high speed while the image is recorded on an area detector, allowing the recording of several points simultaneously.

In terms of resolution, the confocal microscope benefits from the fact that both, the illumination and detection PSFs need to be considered for the system's effective PSF and therefore its resolution (*cf.* Eq. 2.17). The pinhole further increases the contrast and gives the confocal microscope the capability to perform optical sectioning in 3D specimens. Following [44] and approximating the individual intensity PSF extents as Gaussian functions, both axially and laterally, the system's total PSF size can be approximated by

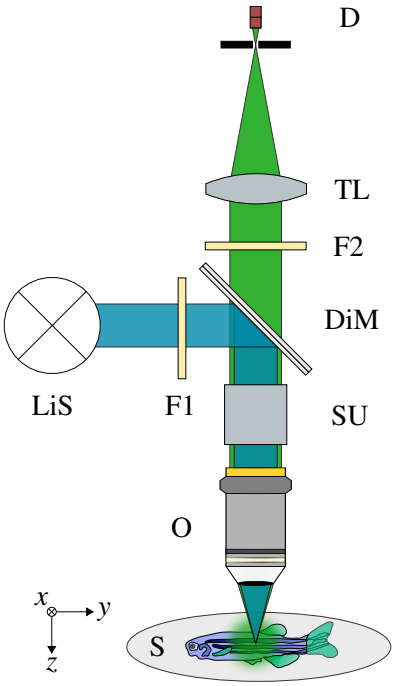

Figure 2.6: Sketch of a confocal fluorescence microscope. Light from the light-source (LiS), typically a laser, is expanded (not shown), spectrally selected via filter F1 and then reflected by the dichroic mirror (DiM). The beam is then coupled into the scan unit (SU) which allows for *xy* movement of the focus. This can be achieved by conjugating two galvanometric mirrors to the BFP of the objective lens (O). The rotation of the scan mirrors is then translated into a focus displacement in the focal plane. The emitted fluorescence is captured by the objective at full NA, then descanned inside the SU, transmitted by the DiM and spectrally filtered via filter F2. The tube lens (TL) focusses the fluorescence beam onto the image plane where a pinhole (P) is located. Scattered light, light from above or below the focus as well as most other photons, that are not originating from the focus of the objective, are not passing the pinhole and therefore do not reach the detector (D). The signal of the point detector is then mapped upon the position the position of the focus inside the sample (S). By movement of the specimen along the *z*-axis a 3D dataset can be recorded. Adapted from [38].

$$\frac{1}{\sigma_{\text{sys}}^2} = \frac{1}{\sigma_{\text{ill}}^2} + \frac{1}{\sigma_{\text{det}}^2} \tag{2.18}$$

Here, σ_{ill} represents the illumination intensity PSF's extent while σ_{det} represents the detection intensity PSF's extent. Both can be calculated as before (*cf.* Eqs. 2.15 & 2.16). With the refractive index and the focussing angle assumed as constant, the system's PSF extent becomes solely dependent on the illumination and detection wavelengths λ_{ill} and λ_{det}. As for most fluorophores the Stokes shift introduces only a change of few percent between λ_{ill} and λ_{det}, it is justified to

approximate $\sigma_{\text{ill}} \approx \sigma_{\text{det}}$ and use an average wavelength $\overline{\lambda} = (\lambda_{\text{ill}} + \lambda_{\text{det}})/2$. This leads to:

$$\sigma_{\text{sys}} = \frac{\sigma_{\text{det}}(\overline{\lambda})}{\sqrt{2}} \tag{2.19}$$

Hence, under ideal conditions, confocal microscopy offers a reduced detected spot size with a factor of $1/\sqrt{2}$. It directly translates to an equal improvement in resolution:

$$\delta_{xy,\,\text{conf}} = 0.61\frac{\overline{\lambda}}{\sqrt{2}\text{NA}} \approx 0.4\frac{\overline{\lambda}}{\text{NA}} \tag{2.20}$$

$$\delta_{z,\,\text{conf}} = 2\frac{n\overline{\lambda}}{\sqrt{2}\text{NA}^2} \approx 1.4\frac{n\overline{\lambda}}{\text{NA}^2} \tag{2.21}$$

Albeit improving axial and lateral resolution at the same time, confocal microscopy does not change the undesirable ratio between the two (*cf.* Fig. 2.5). To improve the axial resolution the illumination path can be decoupled from the detection path, e.g. by arranging the two perpendicular to each other. Such a *confocal θ-fluorescence microscope* provides a more isotropic point spread function since both PSFs, detection and illumination, are elongated perpendicularly to one another. While enhancing each other in the center their intensities cancel each other out off-center[2]. Illustrations and a precise description of the confocal θ-fluorescence microscope can be found in [45].

[2] See also Fig. 4.9 as an example of possible axial PSF extent decrease.

2.4 Super-Resolution Techniques

The two thus far introduced fluorescence microscopy methods share resolutions in the range of Abbe's resolution limit (*cf.* Eqs. 2.15 & 2.16). Within the last two decades a number of techniques surpassed Abbe's limit by a factor of 10 or greater. These so-called *super-resolution microscopes* rely on special fluorophores with photo-convertible properties and can broadly be categorized into two families, the point-scanning or PSF engineering family, and the single emitter localization family. The first group is based on the RESOLFT (REversible Saturable OpticaL Fluorescence Transitions) concept with its best known representative, STED (Stimulated Emission Depletion) microscopy [12][46]. In this concept, comparatively high input powers are used to selectively suppress fluorophores in the vicinity of the focus, effectively reducing the volume from which detectable photons are emitted. In the localization family, with their representatives PALM (Photoactivated Localization Microscopy) [13] and STORM (Stochastic Optical Reconstruction Microscopy) [47], the stochastic emission properties of the fluorophores and dyes are utilized. In these methods blinking single molecules or probes are detected over the period of acquisition such that a super-resolution image can be reconstructed mathematically. The advances in the field of super-resolution microscopy were particularly pushed by Eric Betzig, W.E. Moerner and Stefan Hell who together have been honoured the Nobel Prize in Chemistry in 2014 [48]. Super-resolution brings great benefits into the investigation of small samples, like protein complexes in single cell volumes. However, for studies of multi-cellular dynamics, e.g. embryonic development of animals, these techniques are hardly suited due to the comparatively long recording time, the specially needed chemical treatment of the specimens, and the high energy deposited into the sample.

2.5 Light-Sheet Fluorescence Microscopy

Light-sheet fluorescent microscopy (LSFM), also known as *Selective Plane Illumination Microscopy* with its commonly used acronym SPIM, dates back more than a century when Zsigmondy and Siedentopf used sunlight to create a microscopic corridor of light to illuminate nanometer sized gold particles [15]. Voie *et al.* used a cylindrical lens to create a *light-sheet* and an orthogonal detection to image the inner ear cochlea of guinea pig [49]. Similarly, Jan Huisken in the group of Ernst Stelzer at the EMBL Heidelberg, used a cylindrical lens to illuminate live developing embryos across selected planes for the first time and showed that SPIM is an exceptional tool to study embryology across species [14][50].

For 3D recordings, a single or selected plane of the sample, orthogonal to the direction of detection, is illuminated and then displaced until the desired volume has been scanned and recorded plane-wise. Today, for this purpose, typically at least two objectives are placed orthogonally to each other. Illumination is usually performed via a low NA objective while the illuminated plane is imaged with a higher NA objective. An example setup of a classic SPIM based on the use of a cylindrical lens is illustrated in Fig. 2.7.

For efficient optical sectioning, the light-sheet needs to be aligned to the focal plane of the detection objective. This way only fluorophores from and nearby the focal plane are excited. The spatially confined excitation results in an image of high contrast, especially when compared to a widefield microscope as signal from fluorophores away from the excitation plane do not contribute to blur or unwanted background intensity. Particularly, the axial resolution is better than that of a widefield microscope and can be in the range of a confocal microscope. For information on how this is achieved, see Ch. 2.5.3. Another important attribute of SPIM stems from the conventional widefield detection: An entire illuminated plane can be recorded simultaneously and is only limited by the camera speed and the fluorescence intensity. As a result, high imaging speeds with up to $\sim$ 100 frames per second (fps) and more are possible. The fact that recording speeds are so high and only one plane at a time is illuminated, leads to another important advantage of light-sheet microscopy: It is a gentle imaging technique, meaning that the specimen is exposed to less light and thus less energy. A vast reduction in bleaching and phototoxicity are the result, laying the foundation for recordings of several hours or even days without significantly interfering with the specimen [14][16][51].

2.5.1 Components and Design in SPIM

In a standard implementation of a LSFM, the following components are used:

- light source (typically a laser)
- cylindrical lens or a galvanometric scan mirror for light-sheet generation
- illumination objective lens
- sealed specimen chamber for immersion medium
- movable specimen mount
- detection objective lens
- fluorescence filter
- tube lens
- area detector (e.g. sCMOS/CCD camera)
- hardware and software control devices

A possible arrangement of the optical components is depicted in Fig. 2.7 and matches the conventional SPIM configuration.

Numerous custom microscope setups based on light-sheet illumination have been realized over the last two decades and while it is beyond the scope of this chapter to cover them all, I want to give a brief overview over some of the design concepts, as well as the more often found configurations. Generally speaking, the design, and with it the geometrical arrangement of the objectives, of a LSFM regularly stems from the biological requirements. One example could be the imaging of plant embryos where regular stimulation by an extra light-source as well as correct orientation along the gravitational pull is desired [52]. At later stages, the leaves should also be able to reside outside of any liquid medium which is in contrast to the roots of the plant, which should be submerged. Conventional microscopes oftentimes cannot provide such experimental conditions and custom adaptations are required, if at all possible. With a microscope being built from the ground up, revolving around a certain biological model organism so to say, unorthodox solutions tend to arise. Fig. 2.8 summarizes commonly found objective lens arrangements in light-sheet microscopy.

Historically, light-sheet (fluorescence) microscopy began with one illumination and one detection objective lens as seen in Fig. 2.8 [15][49][65][14]. As scattering, absorption and aberration effects have a negative impact on the sampling and image quality of the recording, a first step was to ensure a more homogeneous illumination through multiple illumination directions [53].

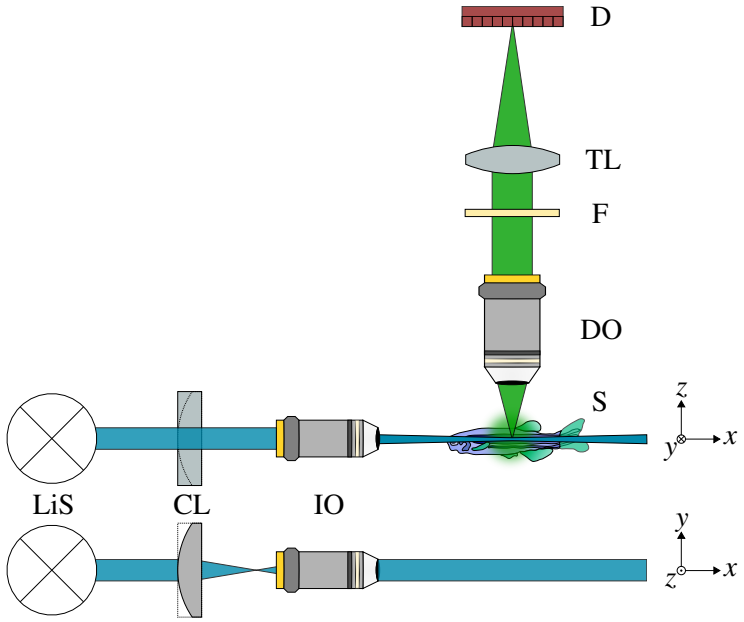

Figure 2.7: Basic SPIM setup with a cylindrical lens. The sketch depicts a basic light-sheet fluorescence microscope based on a cylindrical lens (CL) and an illumination objective (IO) to generate a light-sheet in the focal plane of the detection objective (DO). See also Fig. 2.9 for a more detailed light-sheet description. The fluorescence is collected by the detection objective (DO), spectrally separated from the excitation light with a filter (F) and finally focused by the tube lens (TL) onto the area detector (D). Note that the detection arm is essentially the same as in a epifluorescence setup (*cf.* Fig. 2.2). It is common to define the detection axis as the z-axis of the system, leaving the x-axis as the propagation axis of the illumination beam. For 3D acquisition the sample (S) can be moved along the z-axis. Alternatively, the light-sheet can be scanned along z in combination with refocussing on the detection arm. Adapted from [38].

The addition of a second detection objective lens (*cf.* Fig. 2.8 d) & e)) which allowed for faster recordings and shorter exposure times, was then realized multiple times for different embryological recordings across species, e.g. *Drosophila melanogaster* [55][56], *Danio rerio* [66], and *mus musculus* [67]. These four lens geometries benefit from sophisticated 3D-fusion algorithms with which a more isotropic recording of the sample is achieved. Typically, these geometries are based on a cylindrical mounting environment (*cf.* Ch. 3), such as plastic tubing or gel protruding out of a capillary, to allow for optical access from different angles. In essence, such multi-view setups are the favoured platform for quantitative live recordings of singular comparatively large specimens that can be mounted in a cylindrical and transparent environments. Specimens that are optically either less challenging, e.g. single cells [18][68], or demand special mounting conditions [60], or where out of simplicity a glass coverslip is preferred [18][17][68], fall back

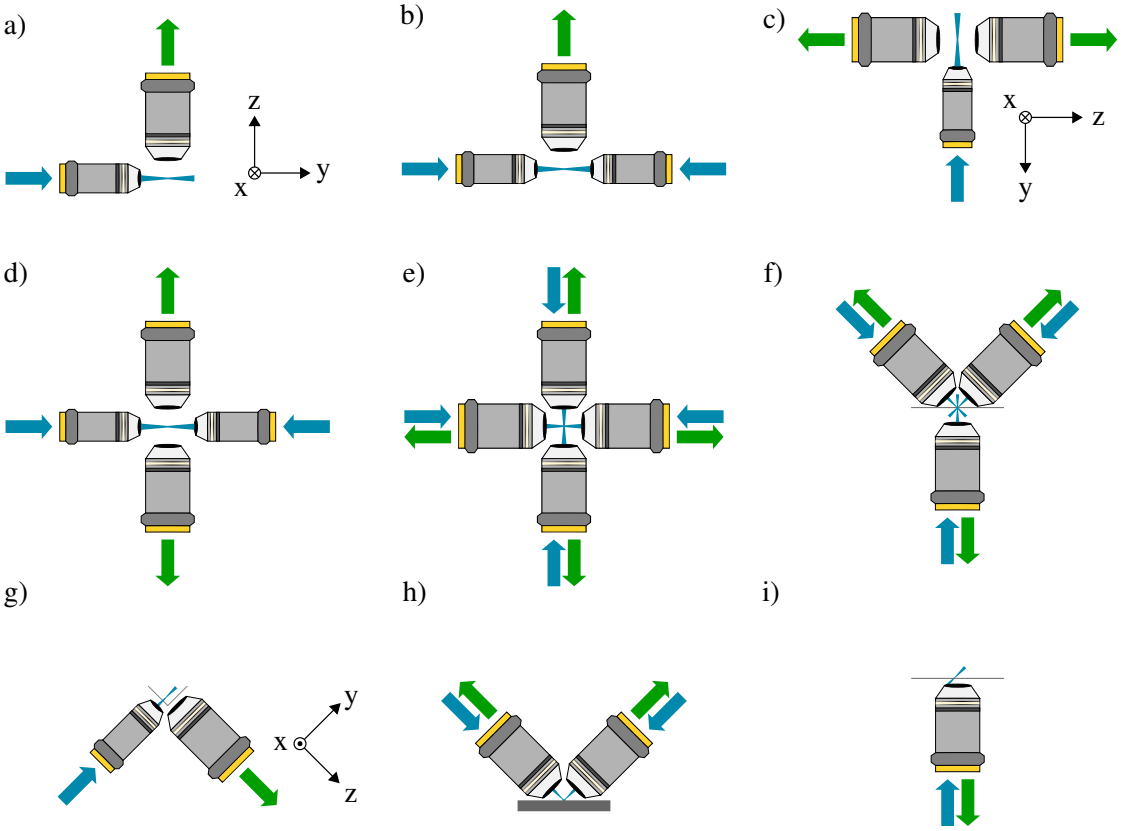

Figure 2.8: Realized SPIM geometries. Some of the more prominent light-sheet microscope geometries are presented here. The beginning of LSFM was marked by a single illumination and a single detection axis as shown in a) [14][16]. A second illumination objective can reduce scattering and absorption artefacts, shown in b) [53][54]. The configuration based on two detection objectives and one illumination objective, as found in c), will be discussed in chapter 4. The setups in d) [55][56] and e) [57] have an additional objective that allows for simultaneous dual or even quadruple detection. The triple objective configuration as shown in f) improves the angular sampling and with the right fusion approach the effective resolution [58][59]. The inverted geometry in g) offers an open-top design for easier sample handling. Additionally, this configuration is typically used for higher through-put imaging [60][61]. When the sample can be imaged on a coverslip or on a similarly easy to mount substrate, a configuration as in h), with one illumination and one detection arm [18][17] or by dual-illumination & dual detection through two objectives [62] can be a feasible solution. Finally, the single objective configuration in i) belongs to the family of the oblique light-sheet illumination microscopes, e.g. [63] & [64], where a tilted light-sheet is created via a high NA lens and swept through the sample. The sheared 3D volume is later "unsheared" in the detection path. Note that only the light-sheets are sketched in this overview schematic while the detection cones are omitted. Blue arrows indicate the illumination direction and green arrows show the direction of detection. Expanded upon [38].

onto a dual objective configuration. Also other geometries have been explored, e.g. using three lenses for better angular sampling [58][59], where the orthogonal orientation of the objectives is no longer present. A currently trending approach is the use of a single illumination objective paired with a oblique light-sheet illumination, as introduced by [63] and [64]. Regular coverslip mounting is easily possible with such configurations and long established culturing methods, e.g. for single cells, do not need to be adapted for new geometries and materials. In the single objective light-sheet configuration however, the 3D volumes are recorded under a sheared view which in the following detection path needs to be sheared back to the reference frame of the detection objective lens. Depending on this method and the objective lens, a percentage of the original detection signal is lost, and resolution anisotropies can arise. Thus far mostly the resolution and isotropic sampling has been the theme of this overview. One more important aspect to consider in the light-sheet microscope design, is the number of samples to be recorded and the means of mounting them.

The developmental time of a mouse embryo, until it reaches its 64 cell stage for example, takes $\sim$ 3 days. As not every embryo develops representatively or even successfully, neither *in vivo* nor *in vitro*, it is not ideal to record single embryos per imaging session. Rather a multi-sample mounting approach is needed. This has been realized by Strnad et al. [60] and successfully used for acini studies by Alladin et al. [69]. Another take on an an open-top microscope for more regular mounting has been explored by [70][71][61]. A novel approach of an open-top system for high-throughput imaging under multi-view detection as depicted in Fig. 2.8 c), is described in chapter 4.

2.5.2 The Light-Sheet

The name giving mode of illumination in SPIM is the light-sheet with which only a single plane is illuminated during the exposure time. There are two classic ways to create a sheet of light which are depicted in Fig. 2.9. The most straightforward method to generate an illumination pattern that is confined in one dimension but extended in the other, is the use of a cylindrical lens [14]. Upon illumination with a radially symmetric Gaussian beam, it breaks that symmetry and creates an elliptical Gaussian beam. The thinner profile is then attributed to the light-sheet thickness, while the more extended part of the ellipse is defining the light-sheet height. The other classic approach is the scanning of a beam along the plane of detection during the camera exposure, creating a *digitally scanned light-sheet* (DSLS). As the scanning is controlled via a signal,*e.g.* voltage, supplied to the scan mirror, this illumination method offers more flexibility, easier alignment, and can be combined with other beam profiles. Also, less energy is lost in the creation of the beam. as usually a part of the elliptical beam profile gets clipped at the objective housing for an evenly distributed energy profile across the FOV.

The light-sheet dimensions are further defined by the beam profile of the light-source, e.g. of the laser. The standard beam profile from commercially available lasers is the Gaussian beam profile. In the following paragraphs the characteristics of such beams, their key parameters, and the resulting properties of Gaussian beam based light-sheets will be introduced. I mostly follow here the summary provided by B. E. A. Saleh and M. C. Teich [72, p. 77 *ff.*]. Note that for the description of the beams, the axis of propagation is along z. In the light-sheet microscope depicted in Fig. 2.7 that axis would be along x. Mathematically, a Gaussian beam can be described by its electric field amplitude which is a solution of the paraxial Helmholtz equation

$$U(\mathbf{r}) = A_0 \cdot \frac{w_0}{w(z)} \cdot \exp\left(-\frac{\rho^2}{w^2(z)}\right) \cdot \exp\left(-i\phi(\rho, z)\right) \tag{2.22}$$

with

$$\phi(\rho, z) = kz + \frac{k\rho^2}{2R(z)} - \zeta(z) \tag{2.23}$$

A_0 is the field amplitude, $w_0 = w(0)$ is the beam's smallest waist size, $\rho = \sqrt{x^2 + y^2}$ is the radial position from the beam axis while z is the coordinate on the propagation axis. The beam radius along the propagation axis is a function $w(z)$ of the axial position. The phase function is

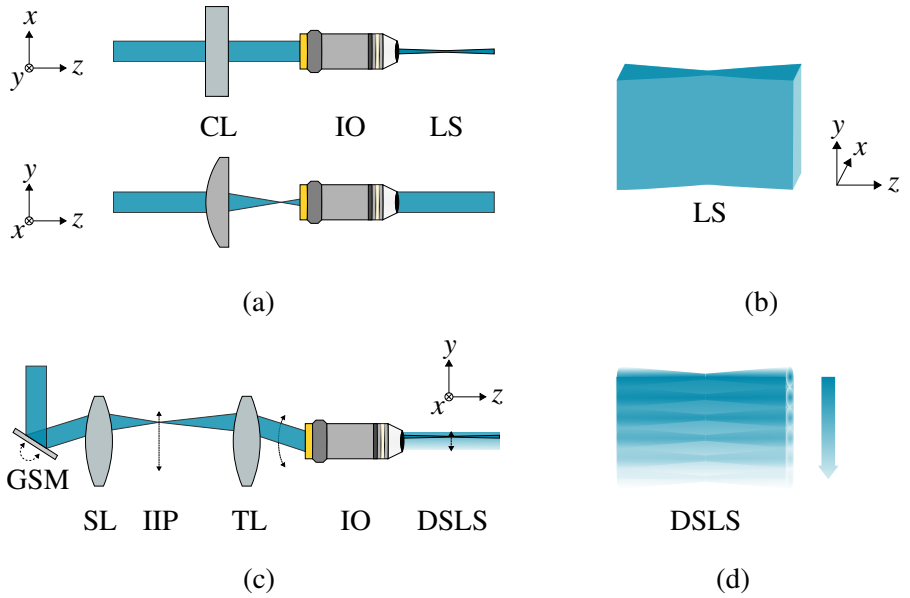

Figure 2.9: Static and scanned light-sheet concepts. The illustration depicts the two methods typically used to create light-sheets. The method employing a cylindrical lens (CL) to create a static light-sheet (LS) after the illumination objective (IO) is shown in (a). While the cylindrical lens behaves like a piece of glass in the xz-plane, it focusses the incoming beam in the yz-plane. As the focus of the CL lies at the BFP of the IO, analogously to the widefield microscope, the intensity is evenly distributed in a collimated fashion after the objective. In the other dimension, similarly as in the fully illuminated BFP of the confocal microscope, the beam gets focussed by the illumination objective. The result is a beam with an elliptical intensity profile in the xy-plane, propagating along z. This profile is abstractly illustrated in (b). To create a digitally scanned light-sheet (DSLS) [16][51], first a scan lens (SL) is used to translate the galvanometric scan mirror's (GMS's) rotation into a scanning motion in y. This is done in the intermediate image plane (IIP) which in turn is then demagnified via the tube lens (TL) and illumination objective (IO). The final result is a DSLS in the image plane, abstractly sketched in (d), with the color gradient and the arrow indicating the movement of the beam. The concept in (c) is following [16]. Adapted from [38].

summarized by $\phi(\rho, z)$. During the detection of such a beam, only the beam intensity $I(x, y, z) = |U(x, y, z)|^2$ can be seen by the observer. The phase vanishes under complex multiplication and does not have to be considered for the following calculations. The beam intensity is then given by

$$I(\rho, z) = |A_0|^2 \cdot \left(\frac{w_0}{w(z)}\right)^2 \cdot \exp\left(-\frac{2\rho^2}{w^2(z)}\right) \tag{2.24}$$

An important trait of Gaussian beams is the parabolic relation between the beam waist $w(z)$ and

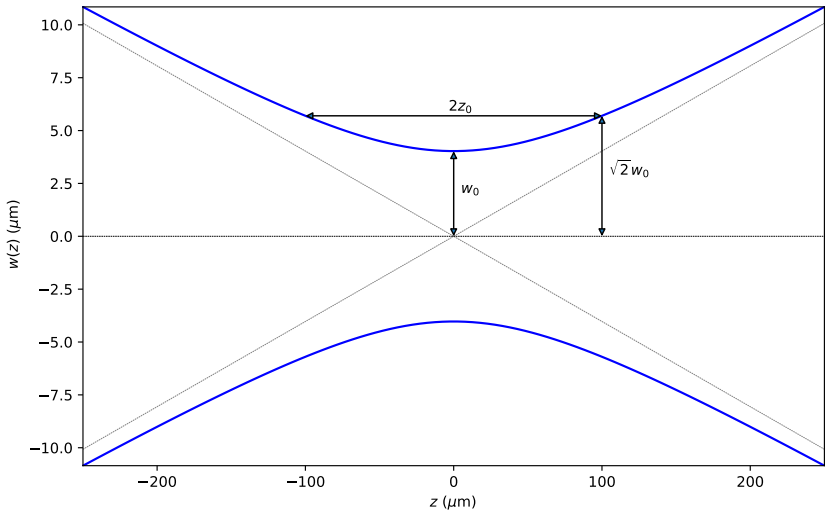

Figure 2.10: Gaussian beam profile along its propagation axis z. The plot displays a Gaussian beam with a Rayleigh range of 100 μm and a minimum beam waist size w_0 of $\sim 4\,\mu$m. Both, the beam length $2z_R$ and the smallest waist w_0 are indicated by arrows. The refractive index of the medium in which the beam propagates was set to $n = 1$ and the wavelength used, is $\lambda_0 = 488$ nm. The beam has diverged to $\sqrt{2}w_0$ after 100 μm, indicated by an arrow. The gray asymptotes passing through $(0, 0)$ indicate the divergence of the beam for large z. For $z \gg z_R$ one can express $w(z) \simeq w_0 \frac{z}{z_R}$.

the propagation distance z:

$$w(z) = w_0 \sqrt{1 + \left(\frac{z}{z_R}\right)^2} \tag{2.25}$$

A useful measure to describe the axial dimension of a Gaussian beam is the so called *Rayleigh range*. It is the distance from the smallest waist w_0 to a position where the Gaussian beam has diverged to $\sqrt{2}w_0$. The Rayleigh range is therefore given by

$$z_R = \frac{n\pi w_0^2}{\lambda_0} \tag{2.26}$$

Small minimum waist sizes will inevitably lead to a small Rayleigh ranges. From the upper relation follows that focussing a beam to a small diameter, introduces a strong beam divergence. It can be expressed as:

$$\alpha = \frac{\lambda_0}{n\pi w_0} \tag{2.27}$$

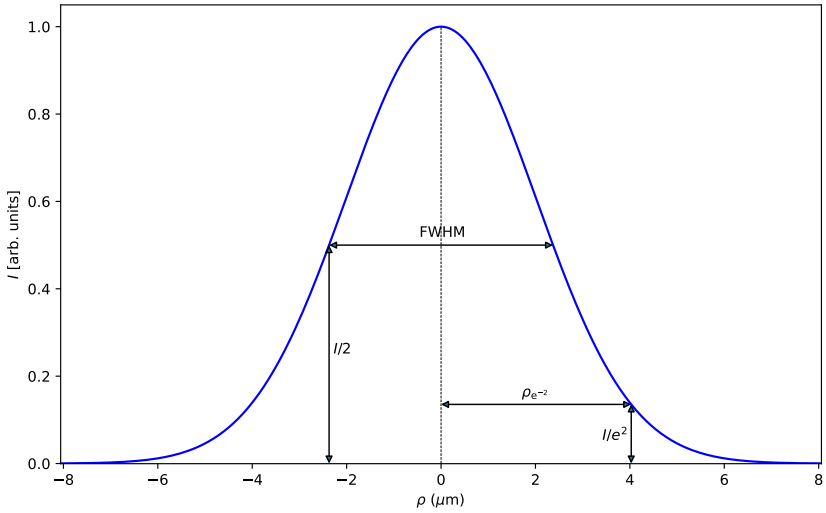

Figure 2.11: Radial intensity profile of a Gaussian beam. The plot depicts the key parameters of the radial intensity profile $I(\rho, z = 0)$ of the same beam as shown in Fig. 2.10. At the minimum waist size $\rho = w_0 \simeq 4\,\mu$m the intensity $I(\rho, z)$ of the beam has dropped to I/e^2. This radius $w_0 = \rho_{e^{-2}}$ is the typical radius to describe the beam size. Alternatively, the full width at half maximum (FWHM), which measures the entire width of the beam at half its intensity, can be used.

The beam divergence is given by the angle (in radians) between the propagation axis z and the waist size $w(z)$ for $z \gg z_R$. Note that these definitions are paraxial approximations and do not hold true when w_0 is in the range of the light's wavelength λ. The beam waist $w(z)$ as well as the here described key parameters are illustrated in Fig. 2.10. Using Eq. 2.24, we further find for the intensity at $\rho = w_0$:

$$I(w_0, 0) = e^{-2} I(0, 0) \simeq 0.135\, I(0, 0) \tag{2.28}$$

This means that the beam carries 86 % of its total power within the diameter $2\rho_{exp^{-2}}$ which corresponds to the definition of $w(z)$ [72, p. 79]. As this definition of the radius accounts for the vast majority of the beam's power, it is commonly used across the literature. Alternatively, the full width at half maximum (FWHM) is commonly used as well. Fig. 2.11 illustrates both measures.

The fundamental divergent nature of Gaussian beams has to be borne in mind when applying them for illumination. Other laser beams with different intensity profiles, axially and radially, exist and therefore Gaussian beams are not the only type of illumination profiles used in light-

sheet microscopy. More information on beam shaping and other illumination patterns can be found in Ch. 4.3.

2.5.3 Light-Sheet Design and Resolution

In light-sheet microscopy the extent of the sample or the desired FOV dictates the dimensions of the light-sheet. To assure homogeneous illumination, the light-sheet length ($2\,z_\mathrm{R}$) should be chosen to match the specimen's dimensions. As this oftentimes corresponds to the imaged FOV, we restrict ourselves to only refer to the FOV in the following. Across the here described microscopes only scanned light-sheets were used. I will therefore not discuss the choice of cylindrical lenses in depth here, but refer to the appendix (*cf.* Ch. 7.1). In the case of scanned light-sheets, the vertical extent of the light-sheet can be controlled via the GSM. The laser beam is rotated by the GSM and then imaged by the combination of a scan lens, a tube lens and the illumination objective. Rotation in the back focal plane of the illumination objective leads to a translation in the specimen chamber and in the focal plane of the detection objective. The rapidly translated Gaussian beam thus makes up the DSLS. Fig. 2.9 (c & d) illustrates the creation of such a scanned light-sheet. Additionally to the flexibility gained from the DSLS, the advantage of the rolling shutter feature of modern sCMOS cameras, such as the Hamamatsu *Orca Flash4.0 V2* or the *pco.panda 4.2 bi*, can be exploited. The rolling shutter enables software controlled confocal line detection, synchronized to the movement of the laser beam. Only a line of few pixels in height is read out on the sensor in parallel to the scanned beam. Light that reaches the sensor and does not match the beam's temporal position is therefore rejected. This feature helps to reduce background light and strongly scattered light. The rejected photons have been scattered, therefore carry only limited information and would rather blur the image if detected. The final result is an image of better contrast and less noise. Technical details and a set of examples can be found in [73].

As mentioned above, best imaging properties are achieved when the light-sheet length matches the desired extent of the FOV. In Ch. 2.3 we saw that an illumination PSF of similar size as the detection PSF can improve the system's effective PSF. This is due to the multiplication of the two intensity PSFs. In light-sheet microscopy, like in theta confocal microscopy, the perpendicular illumination PSF can affect the system's resolution $\delta_{z,\,\mathrm{SPIM}}$ positively. This is typically the case as long as the light-sheet thickness $[w_0;\,\sqrt{2}w_0]$ is on the order of the axial extent of the widefield detection PSF $\sigma_{z,\,\mathrm{det}}$ of the detection arm. The lateral resolution $\sigma_{xy,\,\mathrm{SPIM}}$ is not

affected by the light-sheet thickness. Therefore, analogously to the confocal microscope, the system's resolution can be estimated via [28]:

$$\delta_{xy,\,\mathrm{SPIM}} = \delta_{xy,\,\mathrm{det}} \tag{2.29}$$

$$\delta_{z,\,\mathrm{SPIM}} = \frac{1}{\sqrt{1/\delta^2_{z,\,\mathrm{ill}} + 1/\delta^2_{z,\,\mathrm{det}}}} \tag{2.30}$$

The axial resolution of illumination $\sigma_{z,\,\mathrm{ill}}$ corresponds to the radial extent of the light-beam coming from the illumination objective[3]. Ultimately the used NA of the illumination objective lens defines the beam thickness. The wider the illumination beam in the BFP of the illumination objective, the more of the possible NA is used. This equals a more confined focus or in other words, a thinner but shorter light-sheet. For low NAs the angle of the light-cone is well described by the divergence of the Gaussian beam ($\alpha \propto 1/w_0$, see Eq. 2.27). Beginning with a desired FOV of size $\mathrm{fov}_x \cdot \mathrm{fov}_y$, the light-sheet length is given by

$$2z_\mathrm{R} = \mathrm{fov}_x \tag{2.31}$$

Using Eq. 2.26, the beam diameter $b = 2w_0$ and the beam's waist w_0 can be calculated via

$$w_0 = \sqrt{\frac{\lambda_0}{2n\pi}\mathrm{fov}_y} \tag{2.32}$$

Assuming the field number (FN) of the detection objective and the installed magnification $M = f_\mathrm{obj}/f_\mathrm{TL}$ match the camera sensor size ($\mathrm{FOV}_\mathrm{cam}$) with

$$\mathrm{FOV} = \frac{\mathrm{FOV}_\mathrm{cam}}{M} \tag{2.33}$$

An example of the here presented parameter estimations can be found in Ch. 4.3. In the end, best imaging results will be achieved with light-sheet lengths tailored specifically to the biological question present. Apart from the choice of objectives, and light-sheet parameters, the optical performance inside the specimens will affect the final image quality and resolution. Highly light-absorbing, scattering or aberrating samples, but also photo-inefficient fluorophores and

[3] In respect to the previously described light-sheet coordinates (*cf.* Fig. 2.9 or the Gaussian beam, the x and z axes need to be swapped.)

dyes have a strong impact on the achievable contrast and resolution across the 3D volume. The following two chapters will focus on approaches how to mitigate aberration effects (*cf.* Ch. 3) and on how to increase contrast and resolution in a high-throughput system via dual-detection and usage of extended *'pushed'* light-sheets (*cf.* Ch. 4).

3 Refractive Index Matching in Live Light-Sheet Microscopy

Throughout the two decades during which light-sheet microscopy has been used to study biological samples, only few studies addressed a common problem in microscopy, which is optical aberrations. It is, next to light-scattering absorption, and auto-fluorescence, one of the main reasons for resolution and signal loss, as well as a reduction in contrast or image quality. While well characterized theoretically, commonly dealt with in astronomy and in other microscopy methods via adaptive optics, light-sheet microscopy has yet to see feasible implementations and methods that allow for long-term aberration correction across scales. An important contribution to the field has recently been achieved by Liu *et al.* who implemented adaptive optics to correct for aberrations [74]. The authors' system however is of limited reproducibility, due to its size, complexity, and costs. Another drawback is given by the comparatively small FOV that the authors were able to correct per acquisition. The work nonetheless highlighted the usefulness and need for aberration correction in tissues, as not only single cells, but intracellular events were observable in deep tissue layers. The field of microscopy, especially the light-sheet community, would greatly benefit from resolution and image quality improvements across temporal and spatial domains. There is after all, the need for a pragmatic, cost efficient, and reproducible method to improve resolution and image quality. Piercing optically into greater depths and having more confidence in the signal readout would be the outcome.

This chapter deals with a novel approach for light-sheet microscopy, based on refractive index (RI) matching on live samples, which enabled me to minimize aberrations and restore the resolution and image quality across scales. First, I will introduce the concept of aberrations and their link to the sample's RI closer. With the concept at hand, I will show possible effects of RI mismatch based on simulations of small volumes. Next, the microscope setup used for *in vivo* refractive index matching is presented and an application example based on gel samples is shown. From there I will show five examples across four different model organisms on which

RI adjustments were performed. The adjustments success is evaluated by a custom pipeline revolving around spectral analysis of the image content.

3.1 Optical Aberrations

In short, aberrations in optics mean that an optical system deviates from its ideal optical performance, *e.g.* the theoretically calculated PSF is not reached. A multitude of reasons can cause such suboptimal performance, often times going back to the misalignment of parts of the microscope, low quality or damaged optical components, but also to the sample and its surroundings.

If one considers the sample as an optical element itself, through which light propagates, it is obvious that an imperfect sample will affect the light propagation negatively. Extending this thought, an asymmetrical specimen, or an inhomogeneous distribution of refractive indices (RIs) inside of it, can introduce light-path differences, ultimately leading to aberrations. For best optical performance and the most quantitative imaging however, it is crucial to be aware of the mechanisms behind sample induced aberrations and how to minimize or correct them. Therefore, I want to shed some light onto the sources of aberrations and how to possibly minimize them by considering the refractive index.

In microscopy, we can broadly categorize optical aberrations, which are based on refractive effects, according to their origin:

1. sample (internal)
2. sample to media (interface)
3. media to detection lens (interface)
4. optical system

Present aberrations in the optical system, translate into optical path length differences between light-rays. If the phase of the propagating light-waves is considered, aberrations manifest themselves in wavefront distortions, *e.g.* non-spherical wavefronts arriving at the objective, or non-plane waves in the pupil plane. Figure 3.1 illustrates the idea of rays exhibiting path length differences in a) and wavefront distortions induced by refractive index mismatch and inhomogeneity in b). Note that the two descriptive approaches to aberrations, based on rays or waves, are complementary to one another.

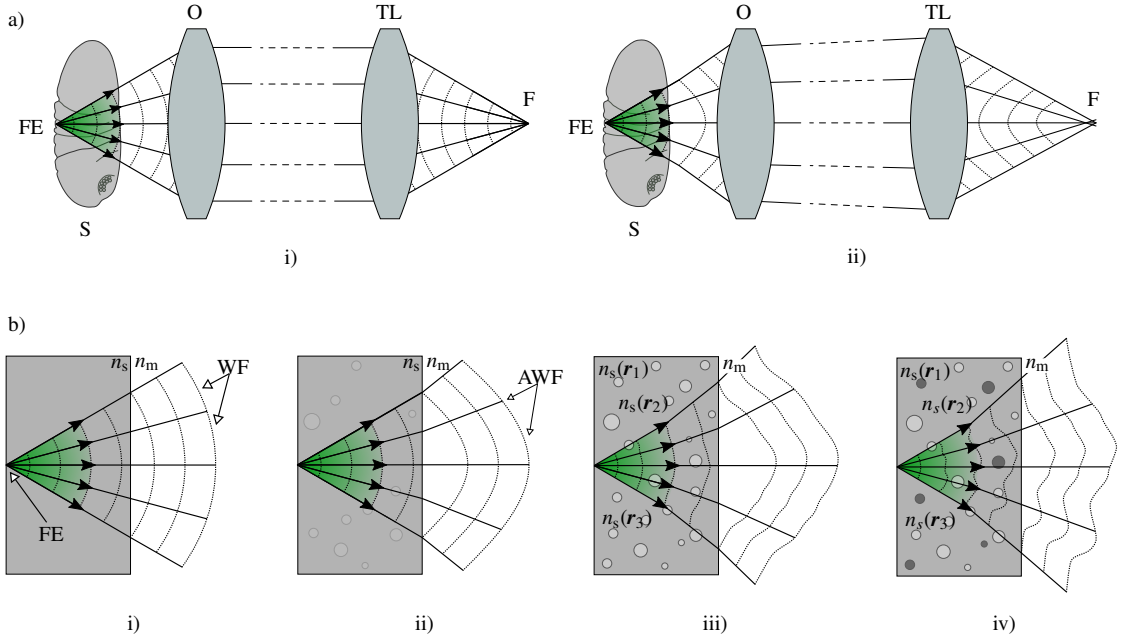

Figure 3.1: Conceptual sketch of sample induced aberrations. The sketch in a) depicts a perfect imaging system in i) and an aberrated system in ii). In both cases the sample (S) has a point-like fluorescent emitter (FE) which is imaged by an objective lens (O) and a tube lens (TL). In the idealized scenario shown in i), no aberrations are present, and the point-like fluorescence is perfectly relayed into the focus (F) of the TL. In the case of a refractive index change between sample and medium, the light-rays and wavefronts do not follow their original path any longer. This is shown in ii), where these aberrations lead to a blurred focus, illustrated by non-spherical wavefronts and by rays which intersect before the focus. In b) four possible domains of hypothetical biological specimens are sketched. The ideal scenario, where the sample's refractive index $n_s = n_m$, introduces no aberrations to the wavefront as it remains spherical upon passing the sample-to-medium interface. With minor differences between $n_s \approx n_m$, shown in ii), a small gain in curvature can be observed in the now aberrated wavefront (AWF). A heterogeneous refractive index distribution, depicted by $n_s(\mathbf{r_i})$ in iii), causes the wavefront to accumulate aberrations before it reaches the sample-to-medium interface. There it gains additional curvature, further adding to the amount of total aberration present. Finally in iv), if the light accumulated significant amounts of aberration before reaching the surface of the sample, *e.g.* because of a highly heterogeneous distribution of refractive indices within the sample, the difference at the sample-to-medium interface will appear insignificant.

Microscopes are ideally designed such, that they can under ideal conditions, perform diffraction limited from the point of the objective lens back to the light-source or the detector. Therefore, I will not address the category of the optical system itself regarding aberrations. Equally, the sample itself is in live microscopy barely accessible, and therefore its properties are usually given. The interface between the mounting medium and the objective lens is geometrically defined by the lens design. Correcting for different immersion liquids is possible, and usually is performed via a correction collar. The category of sample to medium interface however, is a

degree of freedom that can be manipulated via medium exchange.

The amplitude of wavefront distortion and ergo aberration varies with the tissue, the depth, and the light's directionality, *i.e.* angle of incidence. Should the light's, *e.g.* emitted fluorescence, accumulated aberrations from within the sample outweigh the sample-to-interface aberrations, no significant improvement in signal or image quality is to be expected. This case is depicted in Fig. 3.1 b) iv). For small to medium internal aberration accumulations (case ii) & iii)), an adjustment of the medium's RI is expected to lead to resolution and image quality improvements.

In light-sheet microscopy, aberrations are present on both, the illumination and detection side, and it is important to understand which contributions the two different arms can play for the resulting image quality. After all, the usually low NA illumination is expected to show different results than the high NA detection.

With the aim of reducing present aberrations on the sample-to-medium interface laid out, measuring present aberrations in a system, and their possible reduction, is not necessarily straightforward. This is especially the case when imaging a volume or an area comprised of multiple light-sources, *e.g.* multiple emitting fluorophores across a FOV. This is inherently the case when line-scanning illumination and widefield detection is at the core of the microscope system. In the case of a present point-source, as the sketched fluorescent emitter in Fig. 3.1, it is possible to readout the wavefront after the infinity-corrected detection objective, and before the focussing tube lens.

A common tool to measure the wavefront is the so-called *Shack-Hartmann sensor*[1] [75]. In essence, it uses an array of micro-lenses to create an array of images on a camera from which the wavefront can be estimated. In this approach it is crucial to have a point-like emitter that generates a strong signal that can be recorded via an area detector. This is not always possible in live samples, and different solutions have been suggested. For example, the introduction of a multi-photon excitation source to limit the excitation and therefore fluorescence emission to a confined volume, has recently been shown in light-sheet microscopy [74]. Instead of going the complicated route of introducing single point-like sources in live samples, implementing an extra sensor, and installing a special light-source for the point-like excitation, we decided to investigate image quality or contrast[2] across the recorded 3D volumes instead. No readout of the wavefront is performed this way, but a corrected wavefront, *i.e* of more spherical shape after

[1] Ideally, a 4f relay system images the pupil plane of the detection objective onto the Shack-Hartmann sensor.
[2] Image quality and contrast are used interchangeably throughout this work.

exiting the specimen (*cf.* Fig. 3.1), will lead to an improved focus on the camera sensor. This equals an improved PSF at the detected subvolume. Therefore, if aberrations are corrected by any means, and other effects as *e.g.* scattering do not dominate the present image degradation, an improvement in image quality can be detected.

A regular practice when comparing image quality and contrast is a showcasing of intensity line plots across a feature of interest, *e.g.* a cell membrane. Ideally, the intensities differ and a better quality can be claimed. While this can be a useful assessment tool, if specific regions and areas are of interest, it is not suited to give a general overview of a recorded 3D volume. Possible alternatives are given by spectral image analysis in which the image is transformed into its frequency components, *e.g.* via a Fourier transformation. In the frequency domain it is then possible to interpret the highest sampling frequencies in the image, which are related via the optical transfer function to the microscope's PSF.

An in-depth introduction and discussion of image quality metrics goes beyond the scope of this chapter and I therefore refer to the Appendix (*cf.* App. 7.2) for more detailed information. In short, I chose to implement such a frequency domain based analysis approach based on the discrete cosine transform (DCT). Similar metrics have recently also been applied by Truong *et al.* [76], Royer *et al.* [66] and Preusser *et al.* [77] to evaluate the best possible focus and image quality in light-sheet microscopy. The biggest difference to the publications mentioned here, is the normalization of the measured spectral metric to that of a given image, ideally a background image with no fluorescence signal, *e.g.* the camera's noise image. I therefore will refer to the metric as background normalized DCT (BGN-DCT) metric.

A few final comments about the role of the biological sample itself for the here described picture of sample induced aberrations: Every biological sample exhibits a unique refractive index distribution across its 3D volume. Considering that young organisms, as developing embryos, consist mostly of water, proteins, nucleic acids, lipids, and carbohydrates, the average refractive index $\overline{n}$ is greater than 1.33, the refractive index of water. Depending on the chemical composition of the organism and its cellular heterogeneity, subregions of varying size of similar refractive index distributions exist. Organelles for example are typically dense structures with a high content of dry mass and ergo exhibit on average a higher refractive index than the cytoplasm [78]. The nucleus in contrast, has been found to have a lower refractive index in multiple cell lines [79]. Many observed samples in light-sheet microscopy belong to the category of early developing embryos, whose cells only begin to differentiate after multiple rounds of division. In terms of RI distribution this means that it is rather homogeneous among the cells and can

be a beneficial trait for imaging. Further, the sample's geometry can factor into the type and amplitude of aberrations as it affects the refraction on the sample-to-medium interface. Light propagating into or out of the observed specimen, therefore has to travel through regions of varying refractive indices. The longer the path length through the imaged tissue, the more aberrations will be accumulated and eventually, for large enough depths, the wavefront is distorted so strongly, that no meaningful image or focus can be achieved any longer.

Extrapolating the above described RI dependencies of light-propagation in live developing embryos or homogeneous tissues, I propose that adjusting the refractive index of the mounting medium to the sample's average refractive index (near the surface), will result in a reduction of aberrations which will show in image quality improvements.

3.2 Simulations of Refractive Index Mismatch in Light-Sheet Microscopy

As hinted upon above, aberrations can be modelled via ray optics and/or wave optics [80]. In the ray approximation, the cause of aberrations is linked to different path length differences of the travelled light. For example, imagine two rays originating from the same point, passing through an otherwise geometrically symmetric path, but with a different refractive index distributions, after which they are focused by an ideal lens. As the two rays will exhibit different levels of refraction before they reach the lens, they will not meet in the same focal spot any longer. The otherwise ideal focal spot will appear smeared and depending on the location of the intersection, can lead to a misinterpretation of the light rays' origin.

In terms of wave optics, one can consider the wavefront of the illumination or detection light. It is accessible in the pupil plane of an objective relayed out via a 4f system[3]. Under ideal conditions, the pupil plane is homogeneously illuminated and light reaching it, holds the shape of a plane wave. This light can then be focused by the lens to generate an image of the sample. This is the scenario depicted in Ch. 2.2, where I described the origin of the point spread function. However, if the wavefront is not spherical, the intensity distribution in the focus of the lens will not follow the previously described Airy pattern (*cf.* Fig. 2.3) any longer, and lead to a wider intensity distribution. If this is the case, aberrations are present in the system and it is no longer *diffraction limited*. As we saw, the resolution is directly linked to the shape of the PSF, and

[3]The pupil plane is typically located inside the objective housing and therefore physically not accessible.

therefore an optical system suffering from optical aberrations, does not reach its theoretical resolution limit.

Thus far, aberrations have been discussed from the perspective of detection, but they exist also on the illumination side, following the same rules and ideas. Take a laser beam, being focussed into a biological tissue, as an example: An approximately spherical wavefront travels from the lens to the sample, possibly through a mounting medium of refractive index n_{m}, which does not match the sample's refractive index n_s. According to Snell's law, the rays spanning the beam, will diffract and change their angle. In terms of wavefront, this means, that it will no longer be spherical. The focus inside the sample will therefore be of larger size and possibly shifted.

As touched upon earlier, light propagation can be described and modelled with rays, the so-called *ray tracing*, and/or with waves. Generally speaking, ray tracing is used best, when the diffractive behaviour of the modelled light beams is not of the highest importance [81][80, p. 16ff]. Otherwise the calculation of the Huygens-Fresnel integral can be used to gain insight into the diffractive component of the modelled light [80, p. 16]. In the past, ray tracing has been successfully used to model sample induced aberrations for scanning microscopes [82]. Light-sheet microscopy, with its decoupled illumination and detection beam paths, poses an additional complexity layer for modelling. If only the approximate refraction of a beam propagating through otherwise homogeneous refractive index distributions needs to be estimated, an implementation of Snell's law can be sufficient. Examples for light-sheet refractions on cylindrical or round surfaces can be found in [66], [74] (described in the SI). If however, the light's diffractive properties want to be taken into account, ray tracing will not suffice.

A commonly used approach to incorporate the diffractive behaviour of light, is found in the so-called *beam propagation methods* (BPMs) [83] and has been brought into the field of light-sheet microscopy by the group of Alexander Rohrbach, *e.g.* [84]. In these methods a virtual 3D refractive index distribution is generated, in which light is propagated one increment at a time. This is computationally rather demanding and also limited to the (near) paraxial regime, where only (near) parallel beams are simulated, *e.g.* an ideal Bessel beam. A recent improvement in this computational limitation, also directly applied in the simulation of light-sheet microscopy, has been addressed by a software package called BIOBEAM [85]. While still limited to lower angles, it can simulate beams and PSFs up to $NA \approx 0.5$ in parallel. To fulfil this task, the software relies on powerful graphics computational units (GPUs). The performance improvement due to the parallelization, allows for simulations of smaller digital structures in the time range of seconds. The authors have shown, that the software can be used to model beam propagation

through refractive index distributions mimicking embryos.

To be able to interpret the later shown experimental results, I chose to use BIOBEAM to first simulate the effects of a cylinder of a different refractive index than its surrounding medium. However, this is not done to quantitatively extract single PSFs from the 3D model, but rather find areas where strong image quality degradation is to be expected and be able to relate back to its causes. Equally, it is possible to identify in which regions the image quality, represented by the simulated PSFs, remains acceptable. The simulations will showcase how severely a refractive index mismatch can affect the PSF inside the otherwise homogeneous sample.

A technical note on the computational limitations of these simulations: The simulations were all performed on a NVIDIA Titan X GPU with 12 Gb of RAM[4]. To be able to use the parallel computational power of the GPU, the simulated volumes cannot exceed the GPU's memory size. For acceptable precision, the simulations should be performed at least in float32. The voxel size should ideally be isotropic and at sub-micron resolution, *e.g.* 1 voxel $\hat{=}$ 0.25 μm, or ideally even smaller. This results in limitations of the total simulation volume. Simulating a voxel of 1 μm^3 physical size at the resolution of 0.25 μm, results in 64 voxels of 32 bits each, or 256 bytes total. Considering a volume of a *Drosophila* embryo of $\sim 200 \times 500 \times 200\,\mu$m^3 at the given resolution, would require $\sim$ 5 Gb of memory.

Simulations of the Illumination

Biological samples frequently resemble spherical or cylindrical geometries. A *Drosophila* embryo for example can roughly be represented by a cylinder of 200 μm width, and 500 μm height. I used fly embryo's diameter to generate a geometry which I assigned a RI of $n_s = 1.38$ to. The electrical field and from it the intensity distribution of an approximate Gaussian beam was calculated for a full z-scan of the sample at 2 μm step-size. Snell's law predicts that the highest levels of refraction are to be found at the highest angles of the incidence beam to the sample's surface normal. For a round or spherical object this coincides with the beginning and the end of the stack, assuming the cylinder is oriented with its long axis along y. An example of three Gaussian-like beams propagating through a cylindrical geometry is found in Fig. 3.2.

The simulation shows that at the beginning and the end of the stack ($z = \pm 80\,\mu$m), the illumination beams and therefore the light-sheets are clearly refracted away from the original

[4]Random Access Memory - the temporary memory of the GPU. Due to its direct connection to the GPU, the achievable bandwidths are significantly higher than for the shared RAM of the computer which is used by the CPU.

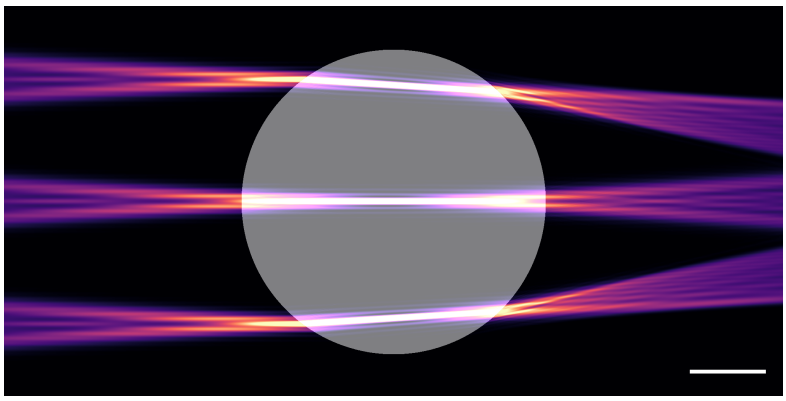

Figure 3.2: Simulated Gaussian beams are refracted at cylinder. Three Gaussian beams were simulated, propagating along the x-axis (from left to right). The cylinder (grey) has a RI difference to the surrounding medium of 0.05. Its diameter is $D_{\mathrm{cyl}} = 200\,\mu$m. The beams with NA = 0.08 are launched at the center depth ($z = 0$), and at $z = \pm 80\,\mu$m respectively. Upon refraction at the cylinder's surface, the beam direction of propagation changes towards the middle. At the center of the cylinder ($x = 0$) their intensity profile is $\sim 4\,\mu$m shifted from their original axis of propagation. At the point of exit from the cylinder, this shift is close to $8\mu m$. Further, for all three beams, the beams' foci shift towards their launching direction marginally. For all three beams, the average intensity is displayed. The simulation volume was set to [x,y,z] = [2048, 256, 1024] voxel at 0.25 μm/px resolution. Scale bar: 50 μm.

propagation axis. A displacement of $\sim 4\,\mu$m at the center of the geometry ($x = 0$), to $\sim 8\,\mu$m at the beams' exits ($x \approx 80\,\mu$m). As a result the detection plane and illumination plane are no longer coinciding and the light-sheet microscope is not performing ideally. For a real sample this would mean, that fluorophores away from the detection objective's focal plane are excited and detected. A possible solution could be the matching of the immersion medium's RI to the sample's RI or pre-tilting the incoming light-sheet for each z-position of the sample as done in [66].

Simulations of the Detection PSF

As shown above, the effects of RI mismatch between mounting medium and sample, lead mostly to a change of propagation direction on the illumination side. While light-sheets typically have a low effective NA, the detection is performed with much higher NA. To understand how the detection PSF is affected by the RI mismatch, we simulated the PSFs as in the section above for a cylindrical geometry with a diameter 200 μm, roughly corresponding to the size of *Drosophila melanogaster* embryo. We chose to use a NA of 0.5 as it corresponds to our available hardware and is still within the limits of BIOBEAM's simulation capabilities.

The effects of the RI mismatch grow with depth and towards the edges of the cylindrical

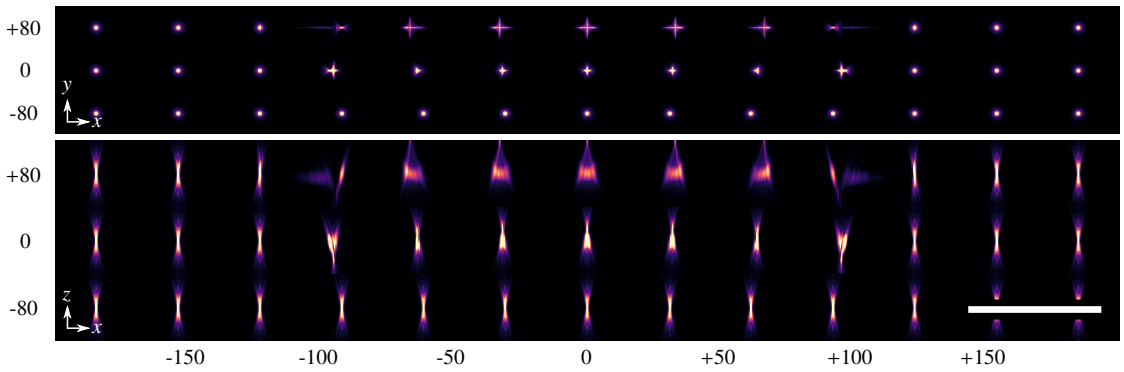

Figure 3.3: Simulated detection PSFs inside a cylindrical geometry. The simulation of the PSFs was performed on the same cylinder as in Fig. 3.2. For a better view the cylinder is omitted. The top image shows an array of maximum intenstiy projections in the *xy*-plane of simulated PSFs at different depths. On the left, the depth inside the cylinder is marked in μm with 0 representing the center of the volume. The deformation of the PSFs towards greater depth and towards the egdges of the refracting volume are striking. At a depth of 180 μm (+80-mark), the PSFs show a cross-like pattern and become smeared out on the edges at $x \approx -90\,\mu$m. Note the displacement of the PSFs in x. This distortion lets the imaged volume appear larger than it is in reality. The bottom image shows the maximum intensity projections of the same PSFs in the *xz*-plane (same view as in Fig. 3.2). Again the PSFs' shapes become deteriorated at greater depths and towards the edges of the cylinder. Also note the curvature and displacement of the PSFs with increasing depth. The simulation volume was set to [x,y,z] = [1600, 256, 1024] at 0.25 μm/px resolution. Scale bar: 50 μm.

volume. Fig. 3.3 illustrates the shape, positional, and intensity changes of the detection PSF in an array of PSFs at different positions. Especially at greater depths, *e.g.* 180 μm as shown in the mentioned figure, the PSFs grow in size, loose their symmetry, and move out of their original position. This already significantly affects the resolution capabilities of the imaging system and is only worsened if we consider the direction of the refracted beam in Fig. 3.2: While the beam is refracted inwards at the mentioned imaging depths, the PSFs are shifted further towards a positive z, decreasing their overlap. We therefore expect to see improvements in samples where the medium's RI approaches the sample's average RI.

The following sections will introduce the experimental approach to refractive index matching and compare imaging results in media of different refractive indices. The simulations let us expect to see the strongest effects on the edges of the sample's geometry, as well as at larger depths.

3.3 Microscope Setup and Experimental Procedure

Recently, Boothe *et al.* showed that the RI can be tuned linearly via a chemical called iodixanol, commercially available in the form of OptiPrep [25]. It can be administered to the mounting medium without harming the live sample[5] [25]. OptiPrep consists of 60 % liquid iodixanol and 40 % water, and has an RI of $n_{\mathrm{OP}} = 1.429$. By mixing it with an aqueous solutions the RI can be tuned linearly and one can determine the required concentration of OptiPrep c_{OP} via the wanted RI n_{wanted} with

$$c_{\mathrm{OP}} = \frac{n_{\mathrm{wanted}} - 1.333}{0.00096} \,. \tag{3.1}$$

The authors showed that resolution, signal, and image quality could partially be restored upon the addition of OptiPrep. However, their use of objective lenses without a correction collar for RI changes, made for a mounting medium of higher RI than water, does not allow to conclude how large the effect on the sample to medium interface is.

Instead, we chose to use a detection lens that would allow us to adapt to the medium inside the sample chamber via a correction collar. Further, we used the flexible nature of our homebuilt MuVi-SPIM [55][73][86] to exchange the sample unit located above the precision stages with a unit suited for refractive index matching. The rest of the microscope remained unchanged.

As this study focuses on the optical effects of RI matching on living organisms, only one detection objective (10x, 0.5 NA, 5.5 mm WD, Nikon MRD71120), was installed (*cf.* Fig. 3.4). The illumination was performed via two air objective lenses (4x, 0.1 NA, 18.5 mm WD, Olympus N1215700). A thin (0.13 – 0.16 mm thickness) coverglass was used as an optical window into the chamber for the illumination.

Upon RI change inside the sample chamber, the illumination beams undergo a focus shift which can be corrected via the lens mounts. For this purpose, threaded rings can be turned to move the objectives with μm-precision along the illumination axis. The detection objective on the other hand is attached to the sample chamber via a thread, directly after the front lens element. Refocussing is performed via the correction collar only. The chamber holds $\sim$ 6.5 ml of fluid and allows the user to access the sample as well as exchange the medium from the top.

[5] Not every sample tolerates any given concentration of iodixanol.

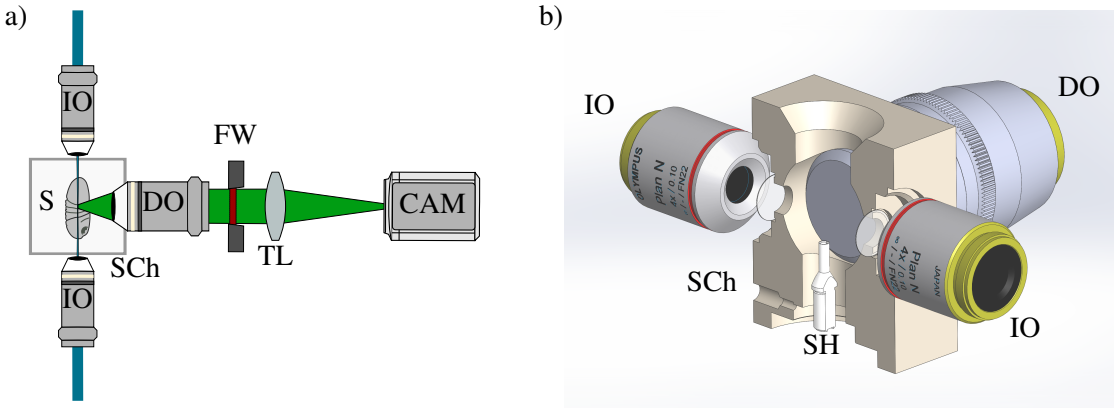

Figure 3.4: Microscope configuration for refractive index matching. The core of the optical setup is the homebuilt MuVi-SPIM platform as described in [55] and [73]. The sole relevant change is the sample unit, also called *Octagon*, which holds the sample chamber (SCh), the two illumination objectives (IOs), as well as the single detection objective (DO). A filter wheel (FW), the tube lens (TL), and camera (CAM) complete the dual-illumination, single detection light-sheet microscope. The core layout is shown in a). The detection objective used, is a multi-immersion lens and therefore mounted directly into the sample chamber as illustrated in b). It is flanked by two air objectives which are used for light-sheet generation. The illumination light passes a thin glass plate before it reaches the sample (S), which is held in place by the sample holder (SH). The two IOs can be moved along their optical axes with the help of two threaded adjustment rings (not shown). This is important to correct for axial focus displacement upon refractive index change. On the contrary, the DO is fixed in position and only the correction color is used to compensate for refractive index change.

3.3.1 Sample Preparation and Mounting

Many commonly used mounting methods for light-sheet microscopy, especially in the geometry used in our light-sheet microscope, rely on embedding the sample in gel or a viscous medium constrained by a thin plastic tubing. In these cases, the interface between sample and mounting medium is not accessible after mounting. This means the refractive index of the medium at the interface cannot be changed without removing and remounting the sample. As we aimed to compare the effects of matching the refractive index at the interface of the sample to the medium, it was crucial to find ways of mounting the sample such, that it was held in space and yet the medium around it could be changed easily.

Here, I summarize in brief the strategies I used to ensure close to constant sample position under medium (ex)change. For further details, please refer to the individual sections of the here presented model organisms. In all cases we made use of our sample holder which is designed to hold capillaries of a diameter of $\sim 1.75\,\mathrm{mm}$. Note that the here presented mounting methods are not all compatible with long-term *in vivo* recordings, but were necessary to test for refractive

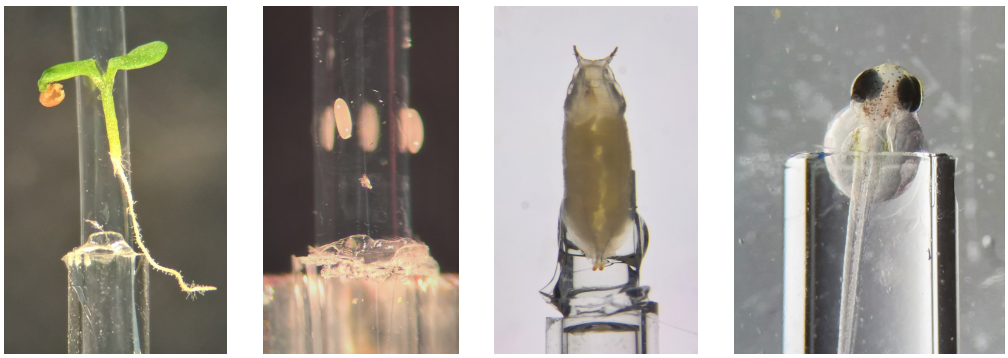

i) ii) iii) iv)

Figure 3.5: Sample mounting in RI matching experiments. This figure illustrates the mounted samples for refractive index matching experiments. The *Arabidopsis thaliana* seedling i) as well as the *Drosophila melanogaster* embryo ii) were attached to an FEP tubing coated with heptane glue. The *Drosophila melanogaster* pupa iii) was glued to an FEP tube which was priorly cut in half along its long axis. The *Oryzias latipes* larva iv) is shown after careful removing of agarose surrounding its head and upper body region. Note the varying scales between images. The glass capillary with a diameter of ~ 1.75 mm, found at the bottom of each image, can serve as a reference.

index matching effects. Once a helpful refractive index range is determined, a suitable mounting method can be adjusted, *e.g.* with the help of gel preparation of a suitable refractive index.

3.3.2 Experimental Procedure

The goal of the RI matching experiments is to study the possible effect of RI adjustment around the specimen of choice, and in case of image quality improvement, identify the ideal RI for the specific sample. Therefore, the experiments were performed as a set of recordings under different refractive index conditions. Data inspection by eye as well as with a the BGN-DCT metric (*cf.* 7.2) identified RIs which offered the overall highest image contrast. The data presented here, mostly shows a direct comparison between the regular condition and the RI of highest contrast.

I began each experiment with a careful alignment of the microscope, ensuring optimal image quality under regular imaging conditions at $n = 1.33$. First, the refractive index correction collar of the detection objective was readjusted to the zero position ($n = 1.33$). The light-sheet focus from both illumination sides was brought as close to the center of the FOV as possible. We then proceeded with sample mounting. Once the sample has been mounted successfully (see above for details), we checked the focus of the detection objective at the surface of the sample by minimally moving its adjustment collar and refocused the light-sheets if necessary. Usually this is not required, but rather serves as a control for proper initial focus. I then proceeded to

record the sample under regular imaging conditions with one excitation light-sheet at a time, using the second light-sheet as a backup and to check reproducibility. Subsequently, light-sheet profiles were recorded for later analysis and to ensure that focussing and positioning has been performed correctly. For the latter procedure the sample was moved out of the illumination and detection paths via the available precision stages.

Next, I exchanged a subvolume with OptiPrep such that the resulting mixture had the desired refractive index. Careful stirring with a plastic pipette ensured a homogeneous spread of iodixanol inside the chamber. Before the next recording, I changed the correction collar to the theoretical position, refocussing onto the now axially displaced light-sheets. The illumination beams remain parallel to the detection plane, but their focal position is shifted along the axis of illumination upon refractive index change. They are subsequently moved back to the center. Minor refocussing can again be performed at the surface of the sample and mostly serves as a control. Once a stack of the sample has been recorded under the new refractive index, we again imaged the light-sheet profile. We then repeated this process until the image quality clearly degraded compared to the first recording or until the sample reached its tolerable amount of iodixanol. Please note that iodixanol tends to form clearly visible schlieren (streaks) at concentrations of approx. 40 % and more. These moving refractive index distributions inside the medium can degrade image quality if they are in the detection path and can lead to light-sheet refractions. After a waiting period of $\sim$ 10 min the schlieren have usually settled and a more homogeneous gradient is present. With sample movement however, new inhomogeneities can arise. Therefore, I recommend to treat results above a refractive index of $n = 1.38$ with caution: A degrading image quality in this refractive index realm is not necessarily due to a mismatch, but can possibly be attributed to the mediums inhomogeneous refractive index distribution.

3.4 Refractive Index Matching on Phantom Samples

In Ch. 3.2, I demonstrated that it is possible to simulate the beam propagations and PSFs in comparatively simple and ideal geometries, such as cylinders. However, due to computational limitations, only small volumes can be simulated at sufficient precision. Further, the fact that BIOBEAM performs best for NAs ≤ 0.5, can be a limiting factor for studies. Therefore I set out to address these limitations with a well controllable refractive index matching experiment on phantom samples. Hydrogels can be shaped into different geometries, for example by filling a cavity while they are liquid. Upon solidification, the shape is maintained and can serve for mounting support or as a phantom sample with controllable propoerties, such as the refractive index. To expand upon larger cylindrical geometries, I chose to examine the PSF behaviour in cylinders of ≈ 1 mm in diameter and of different refractive indices, e.g. $n = 1.33$ & $n = 1.37$. Additionally, I designed the experiment in a way, that PSF evaluation could also be performed upon refractive index matching with the here presented setup. To estimate the PSF, fluorescent beads of $0.5\,\mu$m were mixed into the gel, such that the PSF behaviour over the full FOV could be observed. For this I prepared three gel cylinders, containing fluorescent beads under the following conditions:

- i) Gel and mounting medium share the same refractive index: $n_\mathrm{s} = n_\mathrm{m} \approx 1.33$
- ii) Gel has a higher refractive index: $n_\mathrm{s} \approx 1.37$ & $n_\mathrm{m} = 1.33$
- iii) Refractive index of the mounting medium gets matched to the refractive index of the gel: $n_\mathrm{s} = n_\mathrm{m} \approx 1.37$

The recording of the 3D volume of each cylinder, consists of 2000 recorded planes per experiment, *i.e.* images per volume. Such a recorded volume is commonly referred to as an *'stack'*. The sampling took place at $0.4\,\mu$m z-spacing, effectively spanning a z-range of $800\,\mu$m. Those stacks were *'concatenated'*, *i.e.* added to one another in sequential z-order, for one large volume. Afterwards, they were *'resliced'*, meaning a change of the 3D orientation took place digitally, to show the xz-orientation of the imaged volume. The results are summarized Fig. 3.6 for the three cases as maximum intensity projections in the xz-plane.

For the used 0.5 NA objective and a wavelength of $\lambda_0 = 700$ nm, the ideal extent of the PSF

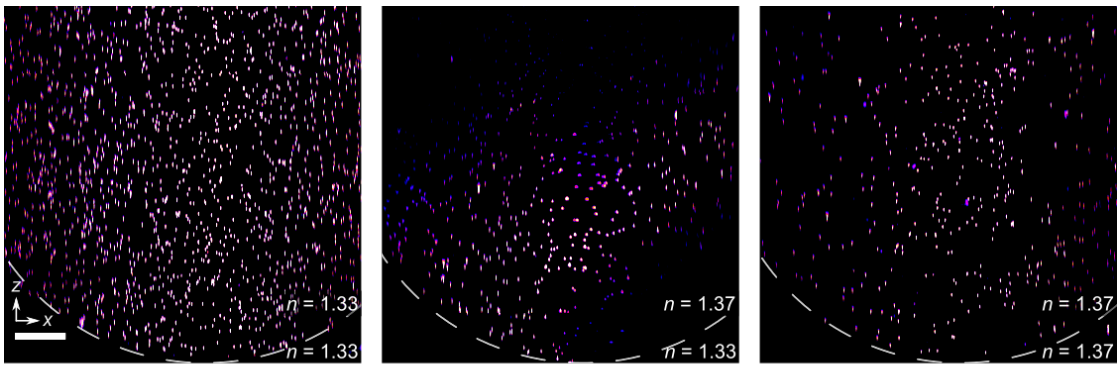

Figure 3.6: RI Matching on Phantom Samples. The panel shows three stitched maximum intensity projections in the *xz*-plane of recorded 260 nm beads with the refractive index matching setup as described in Ch. 3.3. The beads are imaged at a magnification of $M = 15$. The projections in the *xz*-plane show the computationally resliced stacks of the fluorescent beads inside a cylindrical gel of $\approx 1000\,\mu$m diameter. In this experiment the light-sheet illumination is performed from the left side of the stack only, while the detection was performed from the bottom side of the images. Note the difference between i) and ii), the regular imaging at $n_\mathrm{m} = n_\mathrm{s} \approx 1.33$ and the mismatched case with $n_\mathrm{m} = 1.33$ & $n_\mathrm{s} = 1.37$. As in the simulated case, the PSF is strongly affected at greater depths and in areas where the illumination beam is refracted away from the detection plane. Particularly in the bottom right corner and the top left corner in ii), only a low amount of signal is detected. Note also the PSF shape and intensity changes. While a relatively homogeneous *xz*-profile can be found in i), only the bottom right quadrant in ii) has PSFs of similar size and intensity. After adjusting the refractive index of the medium to $n_\mathrm{m} = 1.37$, the PSF shape and intensity is in large parts restored and signal at greater depths can be detected again. The intensity scaling is the same for all three images. The detection settings were also kept constant across the experiments. The excitation wavelength was 685 nm. Scale bar: $100\,\mu$m

is (approximated by a Gaussian profile as shown in Fig. 2.3):

$$\delta_{xy} \approx \sigma_{xy} = 0.854\,\mu\mathrm{m} \tag{3.2}$$

$$\mathrm{FWHM}_{xy} = \sqrt{2\ln 2}\cdot\delta_{xy} = 1.01\,\mu\mathrm{m} \tag{3.3}$$

$$\delta_z \approx \sigma_z = 7.448\,\mu\mathrm{m} \tag{3.4}$$

$$\tag{3.5}$$

To quantify the PSF extent in *xy* requires oversampling of the PSF by at least a factor of 2 according to the Shannon-Nyquist criterion [87]. At the used 15x magnification, a pixel resolution of $0.433\,\mu$m/px is achieved. This is right at the limit of fulfilling the Schannon-Nyquist criterion. Therefore the following PSF dimensions could be extracted with confidence. From the maximum intensity projections of 10 beads in the central region within the first $100\,\mu$m, I measured a FWHM in *x* of $\approx 1.3\,\mu$m. The *z*-extent was below the predicted theoretical limit based on solely

the detection PSF. The light-sheet of approx. $5\,\mu$m FWHM, reduced the PSF intensity in z to $\mathrm{FWHM}_z \approx 4.5\,\mu$m. This matches the prediction of the effective PSF with Eq. 2.30 well. These PSF dimensions shall serve as a reference for the dimensions observed in 3.6.

As expected, the PSFs in case i) are homogeneous in their size and especially near the focus of the light-sheet, are maintaining their profile for greater depths in z. In the case of a refractive index mismatch, the PSFs are only maintained towards the first quadrant on the side of light-sheet illumination. As the light-sheet is refracted away from the detection plane, and the detection plane is also deformed, the combined effects lead to the pattern shown for case ii). Not only the shape of the PSF is strongly affected for different locations in the gel, but also the signal intensity is greatly reduced for greater depths. At closer inspection, some beads around the central region at $z \gtrsim 500\,\mu$m exhibit a resolvable double peaked profile (not explicitly shown). This can potentially lead to the detection of doubled signals in real samples, *e.g.* double membranes, and therefore complicate data analysis or mislead the biological interpretation. Once the mounting medium is adjusted with the right concentration of Optiprep / iodixanol and the illumination and detection arms are adjusted accordingly, the PSF profiles resemble the first, aqueous case again.

These recordings on the one hand are a first proof of principle of the refractive index matching with our microscope design as well as experimental procedure, and on the other hand highlight the extent of aberrations at greater depth in real samples. Typically, the recorded signals in biological tissue are not distributed as sparsely as the here presented beads, and examining the spatially varying PSFs is not possible. This experiment on phantom samples can help to interpret why in real biological samples certain volumes can only be recorded with poor image quality and low resolution. Generally, the combination of simulations for smaller volumes, which cannot easily be realized experimentally, and experimental investigation of larger volumes, which in turn are hard to simulate with current technological limitations, are an effective approach to estimate present aberrations in real samples.

Sample Preparation

In total, three specimens out of gel of two different refractive indices are required. To capture the spatially varying PSFs across the FOV, I chose to use 260 nm beads which were mixed into the liquid gelrite of 1.1 % concentration. Critical for the sample preparation is to account for the physical separation of gel containing iodixanol from the aqueous mounting medium, as otherwise diffusion and a partial adjustment of the refractive index could take place. To prevent

this, first a thin FEP tube ($1.05 \times 1.15\,\mu$m) is inserted into the glass capillaries which are typically used in MuVi-SPIM imaging. The tubing has a refractive index of $n_{\mathrm{FEP}} \approx 1.33$ and due to its thinness is assumed to not affect the imaging noticeably. The tubing extrudes beyond the water level inside the sample chamber and therefore prohibits the diffusion of iodixanol and water between the gel and the water in the sample chamber. To maintain the same dimensions for the gels of cases i) & iii), the tubing was cut near the surface of the glass capillary, and the gel extruded beyond this height.

3.5 Refractive Index Matching on *Arabidopsis thaliana*

A common representative model organism in the field of plant science, is the vascular plant *Arabidopsis thaliana*, especially due to its relation to common vegetables, as cauliflower or cabbages [88]. Further, it has established itself as a model for genetic studies almost 8 decades ago [89]. Remarkably, the plant consists of only single-layered tissues in the root, making it an interesting candidate for cell fate studies and *in vivo* imaging [90][88]. During the embryo's and seedling's development, cells from a stem cell niche almost at the very tip of the root divide and give rise to different cell types.

While the root cap and meristem are well studied and their core processes understood, only recent advances in light-sheet microscopy enabled the long-term recordings of high resolution 3D datasets of the *Arabidopsis* development over extended periods of time [52]. Importantly, the upright orientation, the near physiological mounting conditions, and the low light-exposure of light-sheet microscopy, enabled the authors to record high resolution *in vivo*datasets. Despite the rather small diameter of approx. 100 μm of the meristem, the *in toto* imaging of the root remains optically challenging. One of the reasons is the refractive index difference between the aqueous media and the root itself, but also absorption and scattering contribute to the challenging conditions. Nonetheless, the root presents a comparatively transparent sample, especially when compared to the *Drosophila melanogaster* embryo. As seen in the simulations (*cf.* Ch. 3.2), the difference in refractive indices between tissue and mounting medium, leads to aberrations, especially in greater depths. Therefore, I expect similar effects to be present in the meristem, where vacuoles have not developed yet. These appear higher up in the root, in the *so-called* elongation zone where water is taken up by the cells [91]. Together with Dr. Marion Louveaux, who managed the sample preparation and evaluated possible toxicity effects of *Arabidopsis* seedlings upon exposure to OptiPrep, I recorded 3D image data for multiple refractive indices of the mounting medium. We found that we could restore contrast and resolution in deeper tissue layers by adjusting the refractive index to $n \approx 1.37$. The improvements become particularly evident in the resliced stacks where an improvement in z-resolution and contrast can be observed. Fig. 3.7 summarizes the findings.

I further applied a set of image quality assessments, based on background normalized spectral analysis of the images (*cf.* App. 7.2 for more details), to validate the already visible differences. Fig. 3.8 presents the local metric scores for the same slices presented above. Particularly at the very tip of the root cap, as well as at depths beyond 20 μm, the data from the refractive index

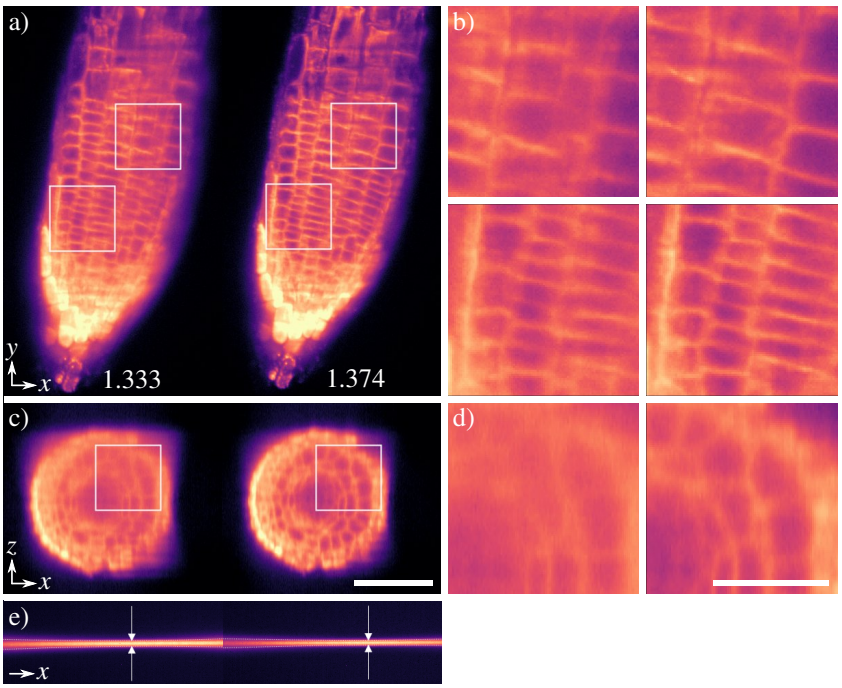

Figure 3.7: Refractive Index Matching of *Arabidopsis thaliana* root. I recorded the root cap and the meristem of an *Arabidopsis* seedling, expressing mCherry in the cell walls, with surrounding media of two different refractive indices ($n_{\text{med,1}} = 1.333$, $n_{\text{med2,}} = 1.374$). Adapting the refractive index of the immersion medium closer to that of the *Arabidopsis* root, leads to visible image contrast enhancements. An example slice at $\sim 30\,\mu$m depth of the recorded 3D stack is displayed in a). Note the improved contrast on the cell walls. A direct comparison of two regions (marked with white squares) is presented in b). A view through the resliced stack, shown in c), further displays the contrast enhancements in the xz-plane, highlighting the PSF improvements in z-direction. A close-up comparison of the upper right quadrant is shown in d). The light-sheets used for the recording, including a fitted profile (white dotted lines) and arrows indicating the location of the smallest waist w_0, are presented in e). The light-sheet illumination occurred from the left hand side with a laser of 594 nm wavelength. Due to a wide spectrum in the intensity distribution and for better visualization of the differences, the logarithmic intensity of the original images is presented here. Scale bar in c) for a), c) & e): $50\,\mu$m, scale bar in d) for b) & d): $25\,\mu$m. Data produced jointly with Dr. Marion Louveaux.

adjusted imaging, scores constantly higher than the regular imaging condition. Interestingly, the intensity for $n = 1.374$ is on average lower than for $n = 1.333$. One possible reason is a small amount of bleaching from the course of the experiments: before the recording of the here presented dataset, four more datasets where recorded for lower refractive indices.

While RI-matching leads to image contrast improvements in the root tip, matured tissues from the elongation zone and further up the stem, do not show positive results This is due to the changing refractive index distribution in the plant, which begins to vary stronger between water ($n \approx 1.33$) and cell wall ($n > 1.4$) [92].

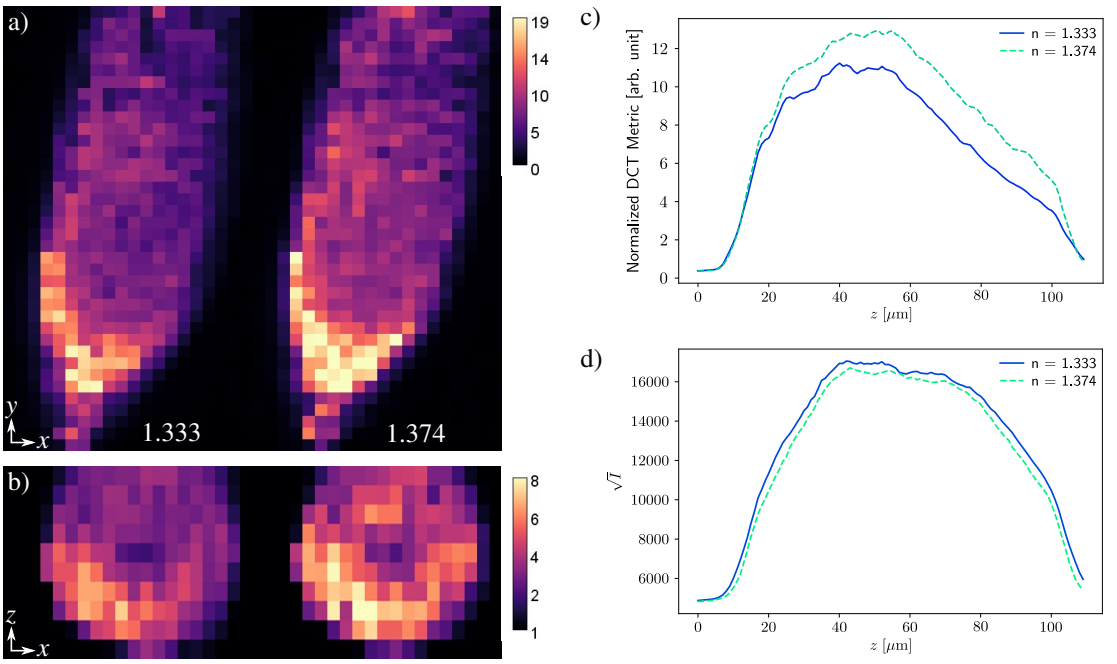

Figure 3.8: Image Quality Assessment of *Arabidopsis thaliana* Seedling for Two Different RIs The images in a) in b) display image metric quality scores on tiles based on the slices in Fig. 3.7. The metric scores confirm the visible differences in image contrast between imaging under $n = 1.333$ and $n = 1.374$. In the xy-plane (a)), the largest detectable difference lies at the bottom of the image or at the tip of the root. Higher scores can also be found around the central region. The differences are more pronounced in the xz-plane, where almost everywhere higher scores are achieved. Next to the tile-wise metric calculations, a whole-image metric was calculated for each recorded z-position of the entire stack. The results are shown in c). The quality of both recorded stacks is very similar for the first z-positions, but from $\sim 20\,\mu$m of depth onwards, the stack recorded under $n = 1.374$ shows a higher image metric score. That difference is maintained until the end of the stack, therefore over the 3D volume. Next to the BGN-DCT metric, the intensity throughout the stack has been calculated plane by plane. The square root of it over the z-extent is shown in d). Both 3D volumes show similar intensities overall, with the regular imaging condition at $n = 1.333$ offering a small percentage of additional signal. Support radius for noise filtering used: $r_n = 1.34\,\mu\text{m}^{-1}$. Tile sizes used (in px): $[x, y] = [15, 16]$, $[x, z] = [11, 16]$.

Sample Preparation

The plants where grown according to standard protocols on gel dishes by my collaborator. The seedling is a delicate and flexible sample. Therefore, finding a mounting approach that keeps the seedling fixed in space upon liquid exchange and also offers a direct surface contact to the medium, proofed to be challenging. We chose to glue the *Arabidopsis* seedlings to a $50\,\mu$m thick FEP tube, attached to a glass capillary. For this purpose we coated the FEP tubing with heptane glue prior to mounting. We then carefully transferred the seedling onto the FEP tube where it

attached to the sticky surface and was therefore held in place, even upon medium exchange. Note that this is not suitable for extended imaging as heptane has toxic effects on the plant. For the course of the RI matching experiment, this is however a feasible mounting option (< 1 h).

3.6 Refractive Index Matching on *Oryzias latipes*

Medaka (*Oryzias latipes*) similar to zebrafish (*Danio rerio*), has emerged as popular model organism in developmental biology due to its natural transparency, manageable size, and especially due to the available and ever expanding set of genetic tools. As a vertebrate with regenerative capabilities (cite), it further draws attention for medical and pharmaceutical related studies [93]. Together with the *Drosophila* embryo, Medaka appeared as a prime example of SPIM-imaging at the very beginning [14] of light-sheet microscopy. Nonetheless, zebrafish is often the organism of choice when showcasing the capabilities of new optical systems. Possible reasons are the already established transgenic lines, the smaller body size and a stiller early embryo development[6]. Recent developments however, make studies based on 4D image acquisition in Medaka more attractive [94]. The authors addressed possible body movements, pigmentation, and tested for optimal fluorescence among a set of commonly used fluorophores. We chose to built upon these improved conditions and further push imaging quality in deeper tissues using our refractive index matching approach.

In this endeavour, I collaborated with Dr. Colin Lischik and Leonie Adelmann, who managed the Medaka sample preparation, tested the *in vivo* capabilities of Medaka in a solution containing OptiPrep, and who assisted me in sample mounting.

We found that indeed, refractive index matching can improve image contrast and remove imaging artefacts. Fig. 3.9 summarizes the results and shows examples of the found improvements in an *in vivo* medaka larva.

As the Medaka larva has already various differentiated cell types, the distribution of regions of differing RIs is to be expected. This in turn means, that the image quality in different regions will be affected differently. One key observation is the suppression of fluorescence *'ghost signal'* when increasing the refractive index. This can be seen in Fig. 3.9 c). In the reslice of the stack, a clear line is observable for the regular imaging condition at the bottom of the image. I hypothesize that it stems from the refraction of the light-sheet at the beginning of the stack recording: While the sample is moved through the light-sheet, its tilting leads to the excitation of fluorophores outside the image plane of the detection objective (*cf.* Fig. 3.3 ii)). Detected signal from out of focus planes replaces the content of the actual recorded plane. This leads to misinterpretation of the sample's volume and makes high-resolution recordings of the surface

[6]Medaka embryos show rhythmic blastoderm movements during their early development. Any imaging modality has to be able to cope, *i.e.* record much faster than those movements.

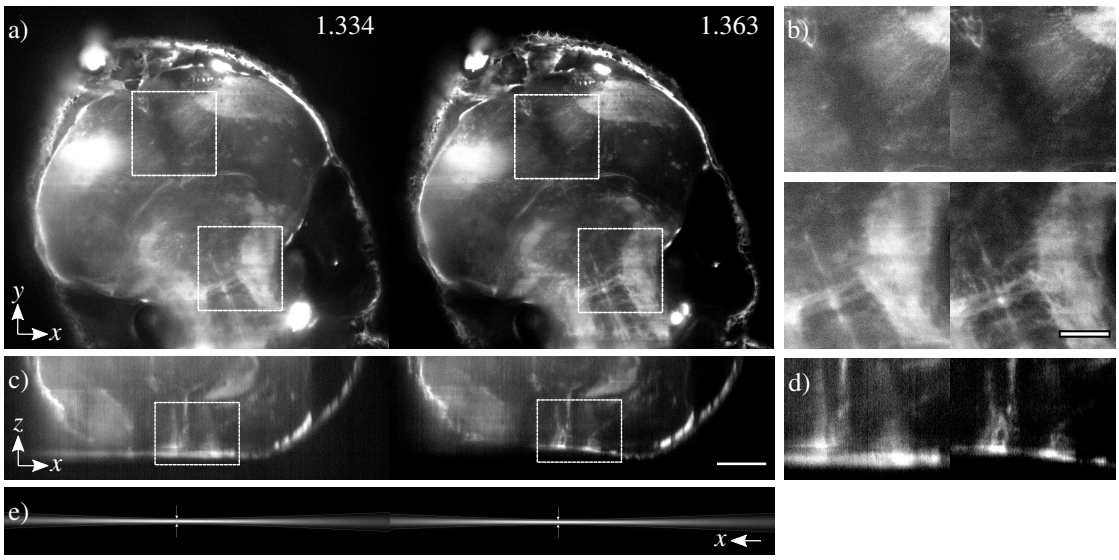

Figure 3.9: Refractive Index Matching of *Oryzias latipes* larva. A dorsal view of onto the head region of a Medaka larva expressing GFP in its membranes is shown here for two different refractive indices. Adapting the refractive index of the immersion medium closer to that of the Medaka larva, improves the overall contrast visibly. An example slice at $\sim 130\,\mu$ depth of a 3D recording under $n = 1.334$ and under $n = 1.363$ is displayed in a). A direct comparison of two regions (marked with white squares) is presented in b). A cross-sectional view of the stack, shown in c), further displays the contrast enhancements in the xz-plane, highlighting the PSF improvements in z-direction. A close-up comparison of lower central region is shown in d). The light-sheets of $\sim 200\,\mu$m length, used for the recording, are presented in e). Arrows indicate the location of the smallest waist w_0. The light-sheet illumination occurred from the right hand side with a laser of 488 nm. The z-step size was $1\,\mu$m. Due to a wide spectrum in the intensity distribution and for better visualization of the differences, I am presenting the logarithm of the original images. The colour map of the images is left in grey values as the differences are better visible than in the dual-colour alternatives. Scale bar in c) for a), c) & e): $100\,\mu$m. Scale bar in d) for b) & d): $50\,\mu$m. Data produced jointly with Leonie Adelmann.

impossible. Contrary to that, adjustments of the RI expose a visible curvature at the bottom of the resliced image shown in c) and d). Without adapting the refractive index it is otherwise undetectable. Instead a line extends well beyond the actual geometry of the Medaka larva.

Analysing the image quality with the help of the BGN-DCT metric showed the sensitivity of it to different noise levels. The metric correctly identifies areas of high contrast and bright content, but also assigns values between 0 and ~ 0.5 to areas of high noise and low contrast. This can in parts be addressed by reducing the support radius in the spectral domain but will affect also the highest detectable frequency, or in terms of resolution, filter out the well resolved portions of the image. Therefore, I conclude that the here used metric needs to be carefully applied to datasets of high noise levels, such as the Medaka larva, particularly if the fluorescence is based on mRNA injections at early stages. Additionally, bleaching occurred during the time frame of

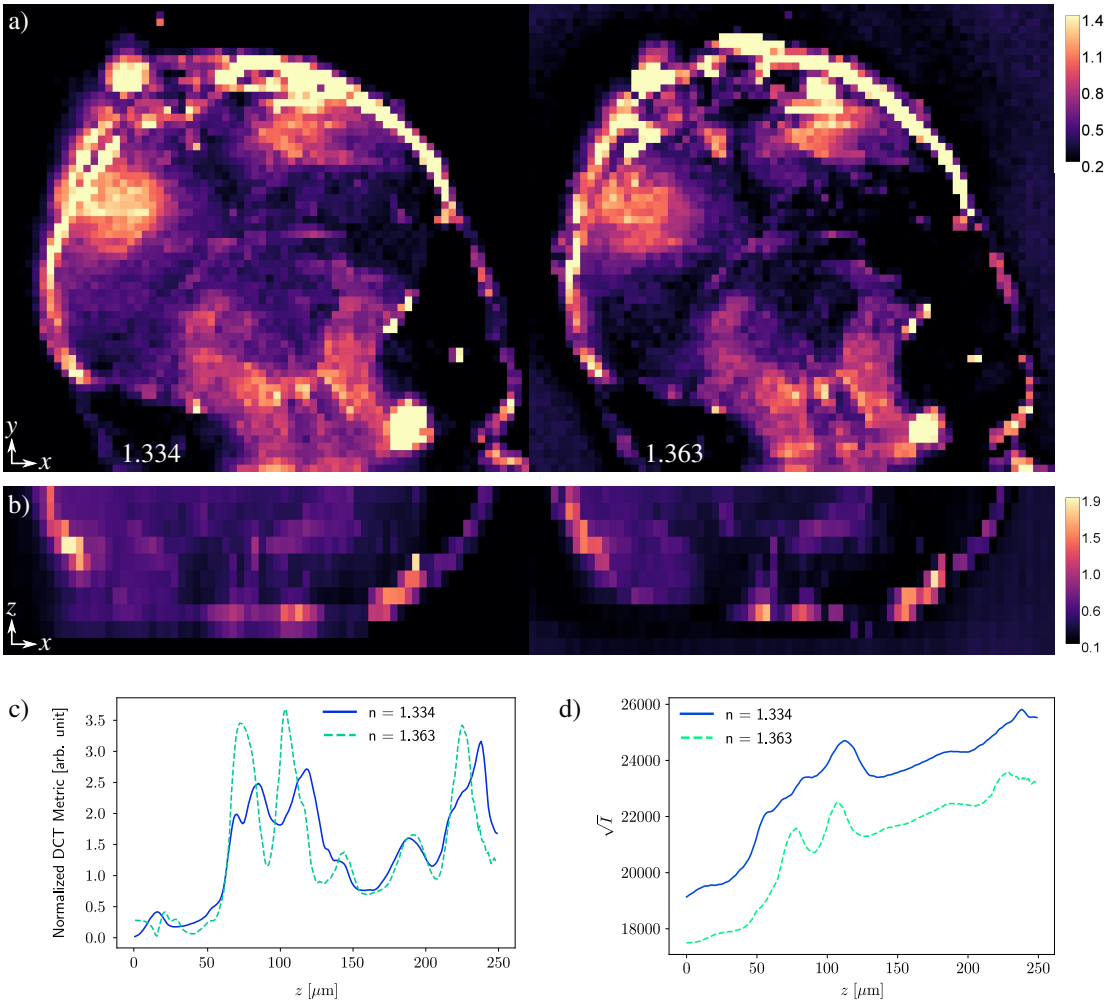

Figure 3.10: Image quality assessment of *Oryzias latipes* larva for two different RIs. The images in a) in b) display image metric quality scores on tiles based on the slices in Fig. 3.9 for two different refractive indices (n = 1.334 and n = 1.363). The metric scores highlight the regions with higher spectral content. The present image noise for both refractive indices, influences the final score. In the xy-plane (a)), smaller regional differences can be found between the two conditions. The metric values in the xz-plane are interesting, as the artefact signal on the bottom left corner counts towards the metric. Next to the tile-wise metric calculations, a whole-image metric was calculated for each recorded z-position of the entire stack. The results are shown in c). The quality of both recorded stacks is very similar for the first z-positions, but from $\sim 60\,\mu$m of depth onwards, the stack recorded under n = 1.363 shows a higher or similar image metric score. Several large strongly fluorescing cells (*e.g.cf.* Fig. 3.9 a), top left & bottom right) contribute strongly to the metric score, and move over the course of the experiment. Therefore, differences between the two metric curves can be the result. Next to the BGN-DCT metric, the intensity throughout the stack has been calculated plane by plane. The square root of it over the z-extent is shown in d). Both 3D volumes show a similar behaviour overall, with the regular imaging condition at n = 1.333 having a higher signal throughout the stack, presumably due to bleaching. Support radius for noise filtering used: $r_n = 1.34\,\mu\text{m}^{-1}$. Tile sizes used (in px): $[x, y] = [25, 25]$, $[x, z] = [20, 25]$.

the experiment, which is confirmed by the intensity profile in Fig. 3.10 d). This stems from the different recorded conditions in this experiment (multiple stacks, with multiple RIs) and can have an additional negative impact on the metric score.

In summary, the image contrast could in parts be improved upon RI adjustment to the Medaka larva, despite its differentiated cell types and its comparatively large size. Additional experiments, ideally in the red-shifted fluorescence spectrum where noise and autofluorescence is reduced, can help identify to which extent RI matching can truely benefit the recording of such large specimens. Apart from the image quality assessment, the clear reduction of imaging artefacts, arising from light-sheet refraction at the beginning of the stack, *i.e* the surface of the larva, was successfully demonstrated.

Sample Preparation

The Medaka embryos were collected according to standard protocols by my collaborators. For fluorescent protein expression and immobilization via α-Bungarotoxin, the embryos were injected with mRNA at the single cell stage as in [94]. The larva were imaged at 5 dpf. We used liquid 2 % low melt agarose to initially pull the larva into a glass capillary. Once the agarose solidified, we extruded the gel gently out of the capillary until the head of the larva and a small portion of its upper body was accessible. The extruded Medaka inside the gel cylinder was transferred into a petri dish with E3 medium. There we used forceps to gently remove the agarose around the larva's head. We then transferred the larva into the sample chamber of the microscope. This mounting method ensured a direct sample to medium interface at the head region while keeping the larva overall at the same position.

3.7 Refractive Index Matching on *Mus musculus*

The most prominent mammalian model organism[7], *Mus musculus* plays an important role in developmental biology and with the emergence of light-sheet microscopy can now be recorded with high spatio-temporal resolution in its first developmental stages [60][95][67]. As the embryo develops, its size increases from $\sim 100\,\mu$m to $\sim 1000\,\mu$m within the first week. Gastrulation, a key event in the development of any organism, begins with the implantation of the embryo into the uterine tissue. While the peri-implantation phase is still poorly accessible for culture and imaging, post-implantation embryos can be cultured and recorded for multiple days [96][67]. However, due to its size and multi-layered tissue, imaging remains challenging. Especially deeper tissue layers during early organogenesis cannot be resolved at a single cell level. However, matching the refractive index of the mounting medium to the tissue of the embryo should, similarly to the samples presented above, increase the contrast and resolution. We therefore performed refractive index matching experiments on post-implantation embryos to study possible image quality improvements on our custom microscope.

For these experiments I received help from Dr. Henning Falk and Takehito Tomita with the mouse samples. In particular, the mounting and evaluation of negative effects of OptiPrep on the mouse embryos' development were performed by my collaborators.

Of important note for the experimental procedure regarding the imaging, is the fact that the here used light-sheet microscope does not offer the possibility for controlled gas exchange, nor a precise enough temperature unit. Therefore, the here performed experiments were decoupled from any survival testing with OptiPrep. In a first round of experiments, we recorded mouse embryos at E7.5 in direct contact with a medium mixture of PBS and OptiPrep. In this set of experiments we found strong improvements in image quality across the entire sample volume. However, possibly due to toxic or osmotic effects, the cavity of the embryo showed shrinking and therefore a quantitative comparison will not be made here. I included example images of the dataset in the Appendix (*cf.* App. 7.3).

As we tested the viability of mouse embryos with different concentrations of OptiPrep, it became evident that even percentages as low as 10 % have detrimental effects on the embryo development. In conclusion, our approach of establishing a direct sample to medium interface required an alternative. In this case, the culturing medium of embryos in the post-implantation phase itself, is a medium of higher refractive index than water. It is based on a variable percent-

[7] cell cultures excluded

age of rat serum and DMEM and can reach a refractive index of up to $n_{\text{med}} \approx 1.350$ [8]. For the normally used water-dipping objectives in light-sheet microscopy, the difference in refractive index will lead to significant aberrations, especially at higher numerical apertures. Filling the entire sample chamber with the medium mixture however, is not a practical approach, as it would require > 6 ml of serum, a costly resource collected from live rats with lethal consequences, per experiment. Instead, we aimed at minimizing the amount of serum required by using a plastic tubing made out of PTFE of similar refractive index, and instead match the medium between the objective and the tubing to the culture medium. Together with the tubing, we were able to compare imaging conditions with a refractive index mismatch and match at the plastic to chamber-liquid interface, corresponding to regular imaging conditions with water dipping objectives, and refractive index adjusted objectives. Again, we found improvements in the image quality in the case of refractive index adjustment, especially in the axial dimension. The results are summarized for an example embryo at E7.5 in Fig. 3.11.

Overall, matching the refractive index to the regular mounting medium of *Mus musculus* post-implantation embryos leads to improved image quality. The differences however, are not as striking as in the *Arabidopsis* seedling's meristem. This is in parts due to the not optimal refractive index, which is still relatively low, compared to the tissue. Further, the PTFE tubing, as well as the native mounting medium can, under even small refractive index mismatches, both still lead to aberrations and light-sheet refractions. Despite these facts, our mounting method paired with the refractive index matching approach is a viable option for mouse embryo imaging and can be a rat serum saving alternative.

[8] Small variabilities ($\Delta n_{\text{med}} = \pm 0.03$) were found, depending on the filtration method of the rat serum.

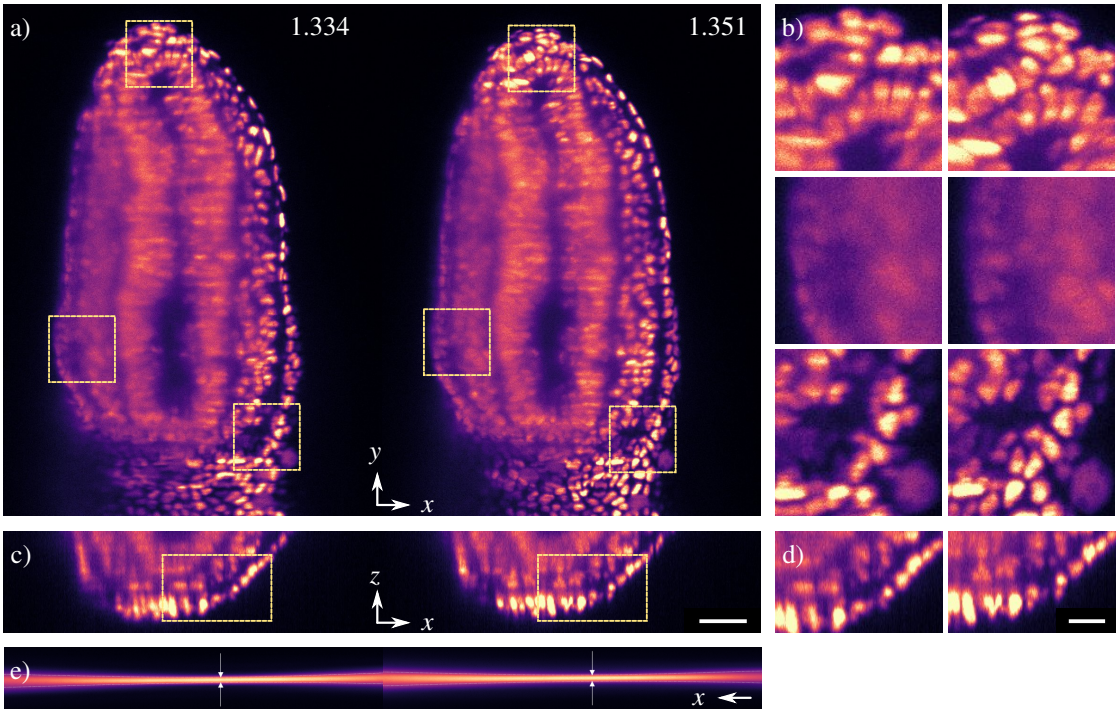

Figure 3.11: Refractive Index Matching of *Mus musculus* Post-Implantation Embryo. We recorded an E7.5 mouse embryo expressing iRFP713 in the nuclear membrane. It was mounted as described in the main text. An example slice at $\sim$ 150 μm depth of a 3D recording under $n = 1.334$ and under $n = 1.351$, between the objective lens and the PTFE tubing, is shown in a). Adapting the refractive index of the immersion medium to that of the culture medium $n_{\text{culture}} \approx 1.35$ results in image quality improvements across different parts of the embryo. Close-up images of three regions (marked with yellow squares in a)) are displayed in b). A cross-sectional view (xz-plane) of the stack can be found in c). Resolution improvements in the lower right quarter of the image can be observed in the form of more confined nuclear membrane signal. A zoom-in comparison of the lower right region from the xz-plane is shown in d). The light-sheets of $\sim$ 200 μm length, used for the recording, are presented in e). Arrows indicate the location of the smallest waist w_0. The light-sheet illumination occurred from the right hand side with a laser of 685 nm wavelength. Imaging took place at 15 x magnification. The z-step size was 1.5 μm. Scale bar in c) for a), c) & e): 100 μm. Scale bar in d) for b) & d): 50 μm. Data produced jointly with Takehito Tomita.

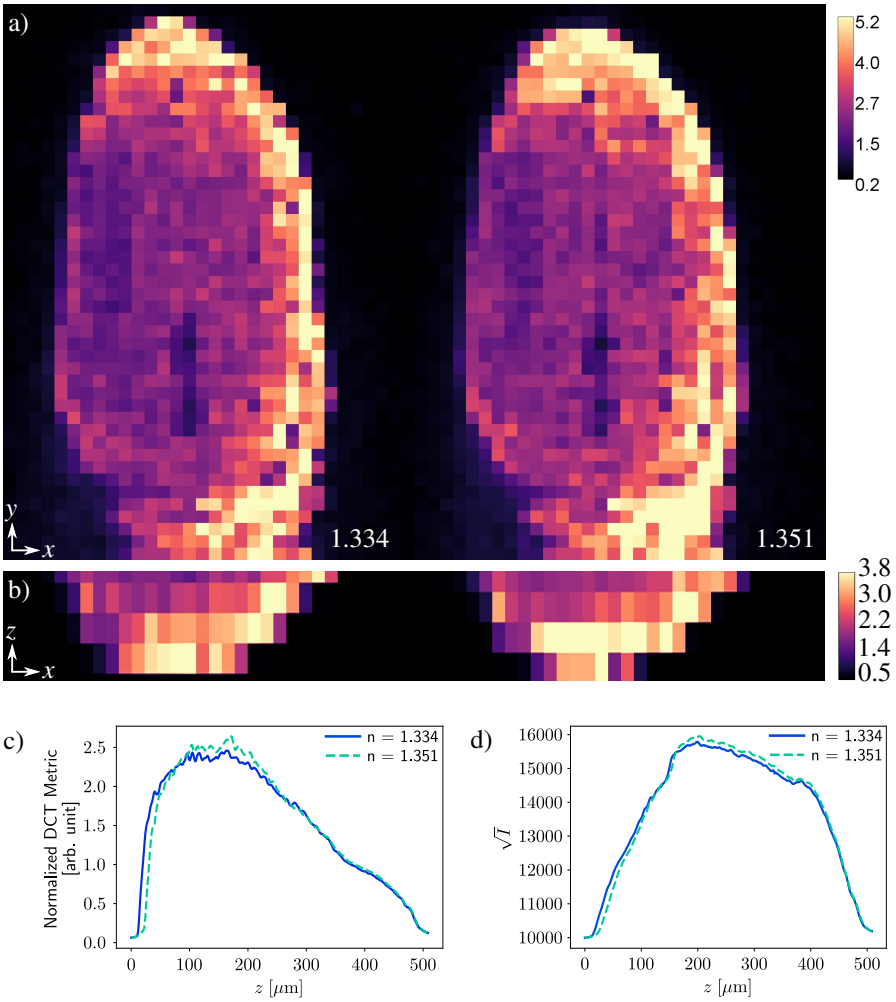

Figure 3.12: Image quality assessment of *Mus musculus* embryo for two different RIs. The images in a) in b) display image metric quality scores on tiles based on the slices in Fig. 3.11 for the two refractive indices $n = 1.334$ and $n = 1.363$. In the xy-plane (a)), smaller regional differences can be found between the two conditions, particularly at the top and bottom righ edges of the embryo shape. The metric values in the xz-plane are highest for the outer most cells for $n = 1.351$, but overall the metric score distribution is very similar. Next to the tile-wise metric calculations, a whole-image metric was calculated for each recorded z-position of the entire stack. The results are shown in c). The quality of both recorded stacks is very similar. Between $z \approx 100\,\mu$m and $z \approx 250\,\mu$m the stack recorded under $n = 1.351$ shows a higher image metric score. The noise in the images increases with greater z and therefore the metric approaches a similar value. Next to the BGN-DCT metric, the intensity throughout the stack has been calculated plane by plane. The square root of it over the z-extent is shown in d). Both 3D volumes show a similar behaviour overall, and between $z \approx 180\,\mu$m and $z \approx 400\,\mu$m a small difference is detectable, with the 3D volume recorded under $n = 1.351$ scoring higher. Support radius for noise filtering used: $r_n = 1.15\,\mu\text{m}^{-1}$. Tile sizes used (in px): $[x, y] = [24, 25]$, $[x, z] = [17, 25]$.

Sample Preparation

The mouse embryos were extracted along standard protocols by my collaborator. The mounting was performed similarly to the mounting method for Medaka. First, the embryo was pulled up into a glass capillary with the help of liquid 2 % agarose. Upon solidification, the embryo was extruded together with the gel and freed from the surrounding agarose with the use of forceps, until only the already formed ectoplacental cone remained embedded in the agarose. This way the rest of the embryo is accessible to excitation light and possible obstructions resulting from the gel are excluded. Subsequently, the embryo can be retracted back into the glass capillary, together with mounting medium, and the PTFE tubing can be added to the outside of the glass capillary. Once attached, it is filled with the mounting medium and the embryo is pushed back out of the glass cavity into the space of the plastic tubing. At this point the specimen can be inserted into the mount inside the sample chamber. The tubing should be long enough to reach above the liquid's level inside the sample chamber as otherwise medium exchange is possible. A thin layer of silicon grease can be used at the lower end of the tubing to ensure insulation.

3.8 Refractive Index Matching on *Drosophila melanogaster*

The famous and widely studied model organism *Drosophila melanogaster* has been successfully imaged on various microscope types over the past decades, including electron microscopy [97] and fluorescence microscopy [98]. Still, this animal poses many unanswered questions, in parts stemming from the fact, that is an optically challenging sample due to its autofluorescent yolk, the large amount of lipid droplets in its early stages, and the rapid development [99]. Beyond its biological relevance in the field, the fruit fly embryo is also historically connected to light-sheet microscopy, as it is one of the first organisms to have been recorded by light-sheet fluorescence microscopy [14].

3.8.1 *Drosophila melanogaster* Embryos

The fast, non-invasive recordings which became possible with light-sheet microscopy allowed for detailed studies of early *Drosophila* gastrulation events, such as the ventral furrow formation [100][101]. With the appearance of the furrow, cells are invaginated and form the mesoderm from which later the fly's organs are formed. As the furrow formation is a tissue-wide process, the study of cells from different regions of the embryo can give insight on the forces and interactions which drive the internalisation of the tissue. Despite the advances in microscopy, it remains challenging to resolve the invaginating cells during ventral furrow formation and follow their dynamics after internalisation. As this event happens on the order of seconds [55], rapid 3D imaging is essential, yet the available photon-budget is limited. Acquisitions on the scale of $\sim 30\,\mathrm{s}$ at high signal-to-noise levels and sufficient z-sampling quickly leads to bleaching, therefore phototoxicity and signal loss (unpublished data from [101]). The subsequently beginning organogenisis can therefore also not be studied at the same spatio-temporal scale as the surface of the embryo. True *in toto* recording with single cell resolution has only been achieved at the surface layers at best, but is crucial for a single cell level understanding of the development of the *Drosophila embryo*. We therefore investigated, whether RI adjustments of the mounting media could have a positive effect on the image contrast and resolution in deeper tissue layers in the *Drosophila* embryo. Example cross-sections under different imaging conditions are presented in Fig. 3.13.

Under the three different refractive indices of 1.335, 1.355, and 1.372, no significant image quality change could be detected, neither in the *xy*-, nore in the *xz*-plane. The only visible

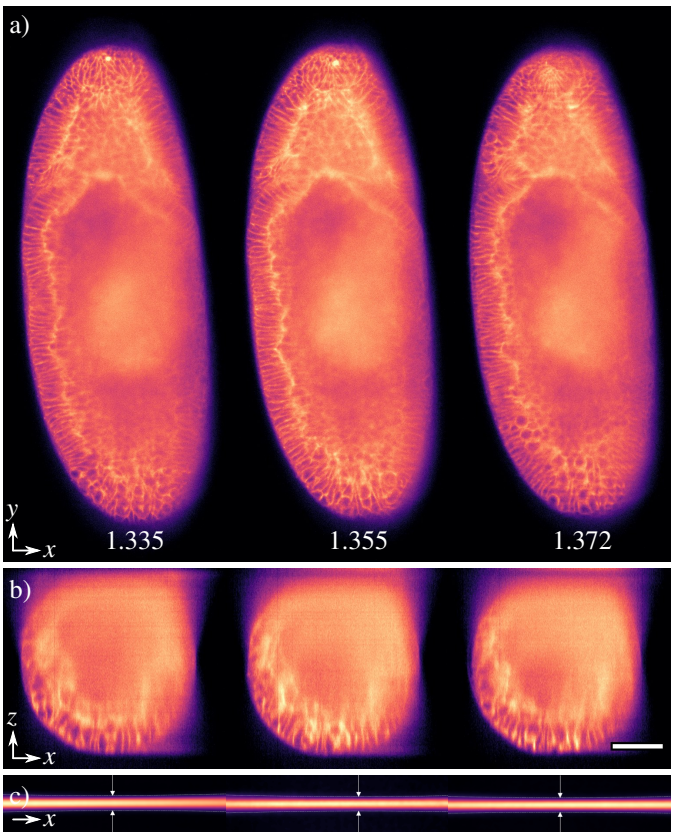

Figure 3.13: Refractive Index Matching of *Drosophila melanogaster* embryo. The images in a) show a cross-sectional view, approx. 80 μm in depth, of a *Drosophila melanogaster* embryo, expressing a Gap43-mCardinal marker which labels the organism's cell membranes. Increasing the refractive index of the immersion medium has little to no visible effect on the image quality. The three conditions shown here, with $n = 1.335$, $n = 1.355$, and $n = 1.372$ are also shown in a resliced view in the xz-plane of the 3D volume in b). Also here, no significant changes are observable. The light-sheets of $\sim 300\,\mu$m length, used for the recording, are presented in e). Arrows indicate the location of the smallest waist w_0. The light-sheet illumination occurred from the left hand side with a laser of 594 nm wavelength. The z-step size was 1.0 μm. Scale bar: 50 μm.

difference is the accumulation of fluorophores in the head region of the embryo in the first two imaging conditions.

With the pipeline for BGN-DCT image quality assessment, I performed an analysis across the 3D-volumes in a plane- and tile-wise manner, and confirmed the unaffected image quality. The findings and a tile-wise assessment are summarized in Fig. 3.14. Note that the algorithm also picks up the fluorophore accumulation in the image quality metric, visible in c).

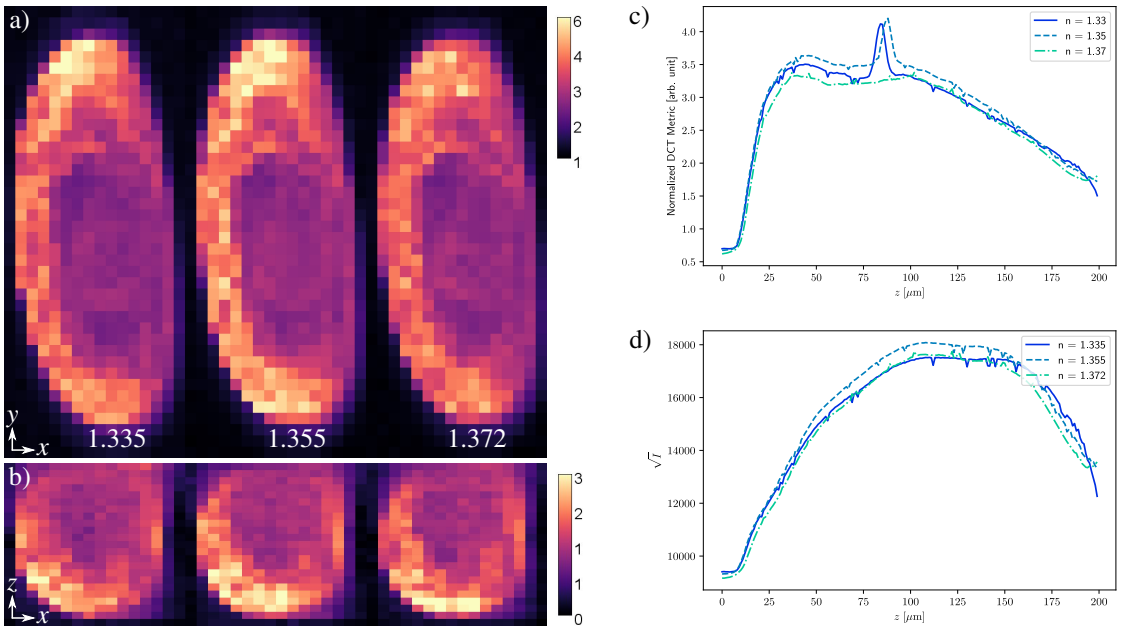

Figure 3.14: Image Quality Assessment of *Drosophila melanogaster* Embryo under Different RIs. The images in a) in b) display image metric quality scores on tiles based on the images in Fig. 3.13. No outstanding differences are detectable, apart from the top area of the images in a), where a increase in intensity, frequency, and ergo a higher metric can be found for a small amount of tiles for RIs 1.335 and 1.355. Next to the tile-wise metric calculations, a whole-image metric was calculated for each recorded z-position of the entire stack. The results are shown in c). Again, no striking difference is detectable, apart from the two peaks at $\sim 80\,\mu$m for the RIs 1.335 and 1.355, stemming from the fluorescence accumulation seen in the top part of the embryo (*cf.* Fig. 3.13). Next to the BGN-DCT metric, the intensity throughout the stack has been calculated plane by plane. The square root of it over the z-extent is shown in d). Support radius for noise filtering used: $r_n = 1.34\,\mu\text{m}^{-1}$. Tile sizes used (in px): $[x, y] = [32, 32]$, $[x, z] = [32, 20]$.

Sample Preparation

The *Drosophila melanogaster* embryos were collected on agar plates and dechorionated with a 50 % bleach solution for $\sim$ 1 min and washed immediately after. Next, they were picked up with a brush and attached to a FEP tube coated with heptane glue. This tube in turn was inserted into a glass capillary (*cf.* Fig. 3.5), which was then mounted in the microscope's sample holder. The fast development of the embryo poses a challenge on the RI matching method, as every stepwise change of RI in the sample chamber requires a minimum of 5 to 10 min. To be able to compare similar structures or ideally the same cells under different conditions, I cooled the entire sample unit and media to $< 15\,^\circ$C. At this temperature the embryo's development is significantly slowed down and side by side comparisons as shown in Fig. 3.13 become possible.

Further, I wanted to minimise the effects of scattering and autofluorescence as much as possible, as these effects limit the imaging depth and affect image contrast severely in the *Drosophila* embryo. For this, I chose a fly line which expresses the fluorophore mCardinal [102], tagged to Gap43, effectively labelling the animals membranes[9]. The fluorophore's excitation peak lies at 604 nm while its excitation peak is shifted to 659 nm. I used a 594 nm excitation wavelength and 594LP filters for detection.

3.8.2 *Drosophila melanogaster* Pupa

After its larval stage, *Drosophila melanogaster* begins metamorphosis, a process stretching over several days, during which a transformation from larva/pupa to the adult fly (imagino) takes place. Despite our curiosity beyond the science community, high resolution recordings of the fly's metamorphosis are lagging in comparison to its embryonic stage. This is partially due to the complexity of the system, the time scales at hand, but certainly also because of its size and poor accessibility to light-based imaging techniques. Additionally, the pupal case or cuticle posts an extra tissue layer around the organism that cannot be removed in the early pupal stages but hinders imaging as it becomes less and less transparent over time. Yet, it is of great interest to unravel the processes during metamorphosis as they are still not well understood, especially not on an individual cell level. The wing-disc, a popular model for organogenesis studies, is mostly imaged *ex vivo*, under special culture conditions [103]. *In vivo* it is however in contact with the pupal epidermis and attached to the pupal body. High resolution *in vivo* recordings of the wing disc's development would be a helpful addition to the field, *e.g.* verify the processes observed in culture.

Pupae further undergo a remarkable process, the head eversion. During embryogenesis the head of the embryo is internalized during a process called head involution. The head then remains internalized until metamorphosis when it is pushed out again from the body. This process takes place remarkably fast, within few minutes, compared to the $\sim$ 4 day metamorphosis. The study of both, the wing disc development and the head eversion, would greatly benefit from high spatial and temporal resolution of *in vivo* imaging. A recent study used tomography to capture the head eversion at high temporal resolution ([104]), however no cellular resolution is achieved. Other studies have used confocal microscopy to study an array of events during metamorphosis [105] and optical projection tomography [106] to record the full pupa, however both studies

[9] Courtesy of the Leptin group, EMBL. The line was also used in [101]

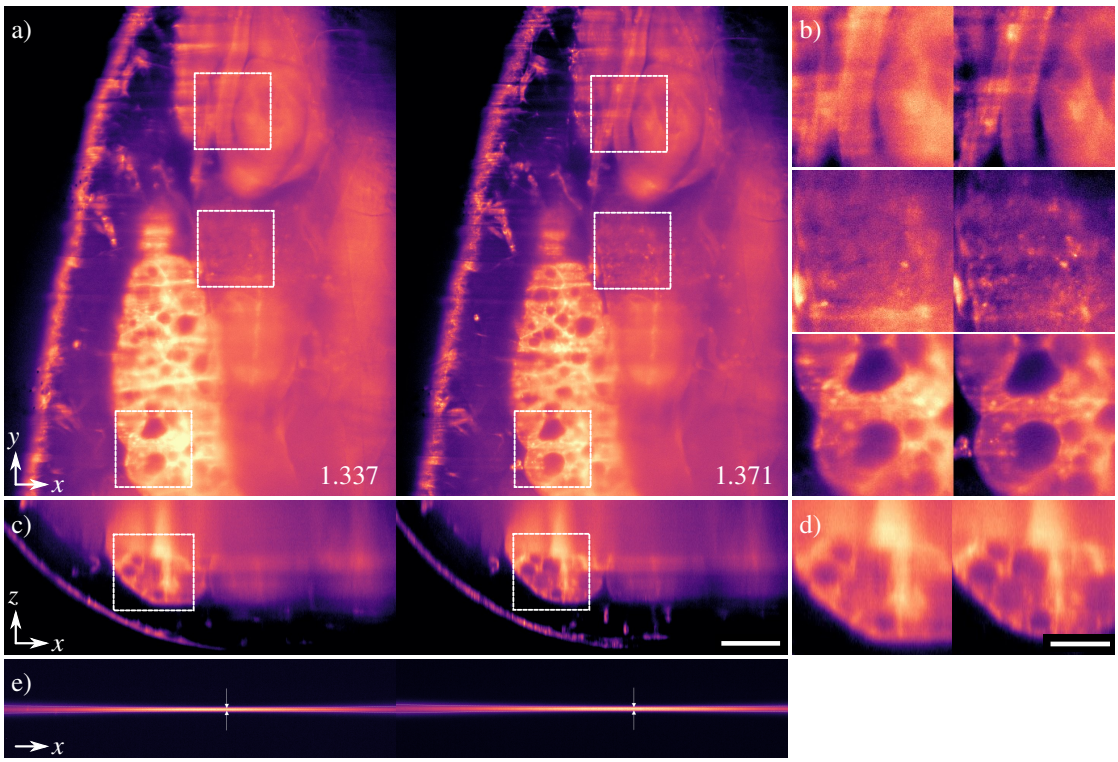

Figure 3.15: Refractive Index Matching of *Drosophila melanogaster* white pupa. The images show parts of the upper body of a white *Drosophila melanogaster* pupa expressing a Gap43-mCherry marker, labelling the organism's cell membranes. Adapting the refractive index of the immersion medium to that of the white pupa results in image quality improvements at different regions in the pupa. An example slice at ~ 90 μm depth of the 3D recording under n = 1.337 and under n = 1.371, is shown in a). Close-up images of three regions (marked with white squares in a)) are displayed in b). A cross-sectional view (xz-plane) of the stack can be found in c). Resolution improvements in the central left marked area can be observed. A zoom-in comparison of this region is shown in d). The light-sheet of ~ 200 μm length, used for the recording, are presented in e). Arrows indicate the location of the smallest waist w_0. The light-sheet illumination occurred from the left hand side with a laser of 594 nm wavelength. The z-step size was 2.0 μm. Scale bar in c) for a), c) & e): 100 μm. Scale bar in d) for b) & d): 50 μm

recorded at mostly 'organ-resolution'.

Here, I tested whether refractive index matching in light-sheet microscopy could help to bridge the gap between high temporal and spatial resolution of such a large sample, and possibly enable insights into the pupas complex mechanisms at single cell scale. Fig. 3.15 shows example slices of a white pupa under two refractive indices.

Indeed, image contrast could be recovered across various parts of the membrane labelled pupa. Membranes and organs appeared visibly clearer. At greater imaging depths of > 100 μm however, image quality in general was affected by an increase in noise and membranes could

not be resolved any longer. Multi-view recordings with dual sided illumination, paired with the electronic confocal slit detection of the cameras, improved the quality further (data not shown). The possibility of *in toto* recordings at the cellular scale are still a number of steps away, but with the here presented approach *in vivo* recordings of the *Drosophila* pupa, are brought one step closer in light-sheet microscopy.

Sample Preparation

During metamorphosis, the cuticle of the fruit fly pupa hardens and slowly becomes optically less accessible. I therefore chose to primarily look at the onset of metamorphosis, when the cuticle is still soft, attached to the white pupa, and optically rather transparent. For this, I carefully extracted 3rd instar larvae showing decreased motility, or directly young pupae from the culture tubes with a wet brush into a petri dish. Once the larvae have transitioned into the white pupa stage, I washed the pupa with a brush in a dish containing PBS. For mounting, a $1.05x1.15$ mm FEP tube was pushed inside a glass capillary, such that approximately $2-3$ mm of the tubing was accessible outside the glass. Then the tube was cut in half along its long axis. After drying the pupa with precision paper, it was placed onto the cut FEP tube and fixed with plant glue, which hardens at contact with water. An alternative fixation solution is two-components silicone glue. Note that during later pupal stages, it is possible to remove the upper part of the pupal case and proceed with the here described mounting method analogously. Different from the other presented samples, pupae require oxygen exchange with the surrounding air during metamorphosis and therefore long-term recordings or survival tests in aqueous solution are deemed to fail. For this reason, I did not perform detailed survival tests including different OptiPrep concentrations, but I nonetheless observed parts of the metamorphosis over the period of multiple hours. Crucial events as head eversion, disc development, as well as the appearance of the gas bubble described by Bainbridge et al. [107] were observed repeatedly.

Concluding Remarks on RI matching on *Drosophila melanogaster*

The heterogeneous refractive index distribution and scattering properties of the *Drosophila* embryo obscured possible image quality improvements in the here presented experiments. To broadly categorize the embryo according to the earlier presented scheme in Fig. 3.1, it falls into category iv), where aberrations inside the sample's volume are so high, that a reduction on the sample to medium interface, has no visible effect. That does not exclude a possible reduc-

tion of aberrations via RI matching however. A possible analysis to gain more insight into the aberrative properties of *Drosophila embryos* might entail direct wavefront measurements after RI adjustment or recording of injected fluorescent beads.

Contrary to its embryonic stage, RI matching on the *Drosophila* pupa, leads to visible improvements in image contrast for the first $\sim 100\,\mu$m of depth, after which the image quality drops rapidly, likely due to a combination of absorption, scattering, autofluorescence signal, and growing aberrations.

3.9 Materials and Methods used for Refractive Index Matching

The most important aspects regarding sample mounting and the experimental procedures of the individual sample types are described in the end of the respective section of this chapter. Overlapping procedures and strategies shall be summarized here.

Refractive Index Change and Measurement

Most experiments comprised a series of recordings to generate data under multiple refractive indices. I first imaged the sample individually with both light-sheets, under different angles, generating at least two 3D volumes for the given RI. Then, a pre-calculated amount of liquid was slowly extracted from the sample chamber and aliquoted for later RI measurement. Subsequently, and once again with caution, OptiPrep was added to the sample chamber, effectively replacing the extracted amount. Careful stirring was performed to avoid local RI gradients. These steps were repeated until a dataset with the desired maximum RI has been generated. From those experiments, I selected the dataset with the clearest image quality improvements, if present. I confirmed my selection by the stack-wise image quality assessment with the BGN-DCT metric (*cf.* 7.2).

The extracted aliquots during the experimental series were all measure with a refractometer. For this as much as $\sim 5 - 10\,\mu$l were enough.

RI Matching Evaluation

All recorded data was screened, pre-processed (cropping, stitching, reslicing, etc.) and visualized in FIJI [108]. The downstream analysis with the BGN-DCT metric was performed with self-written code in PYTHON (Python Software Foundation). There I used functions and packages from numpy [109] and SciPy [110].

A typical data processing workflow from one of the refractive index matching experiments follows these steps:

1. Screen recorded data, create maximum intenstiy projections for overview.
2. Select ROI of sample and crop the 3D dataset. Propagate the crop to datasets from recordings under other RIs. Here a minor adjustment in 3D might be required as the sample can move by few μm upon RI change. Save the ROIs for later selection of the light-sheet area used for illumination and for possible revisiting of data.

3. Save slices of interest, including a representative background image, create resliced datasets for inspection.
4. Switch to Image Quality Assessment in PYTHON, provide relevant imaging metadata, *e.g.* wavelength, voxel size, magnification, NA.
5. Load preprocessed data, generate spectral mask (to filter out noise beyond the resolution limit), generate spectra, multiply spectra with the spectral mask, and perform the rest of the calculation as outlined in Ch. 7.2.
6. Save the resulting datasets, create graphs, preview images, and save the used properties.
7. Switch back to FIJI to visualize tiled image quality stacks, apply the same lookup tables and provide intensity calibration bars.

The processing was performed on a workstation running Windows 10 Pro, equipped with:

- 2 processors: Intel(R) Xeon(R) CPU E5-2620 v4 @ 2.10 GHz
- Memory (RAM): 192 GB
- GPU: GeForce GTX TITAN X (NVIDIA Corporation)

Refraction Simulations

The aberration simulations in Ch. 3.2 were performed on a workstation running Linux, equipped with a GeForce GTX TITAN X GPU (NVIDIA Corporation). I used the package biobeam [85] which is based in PYTHON. I created different 3D refractive index geometries/distributions and various operations, as reslicing, projecting, and other volume-related tasks in PYTHON as well. Stacks of the simulated beam and PSF intensities was saved in separate datasets. Final visualization occurred in FIJI.

Materials

- Low-melt agarose (Starlab GmbH, gelling temperature: 24 – 28° C)
- Gelrite / Gelzan CM (Sigma-Aldrich # G1910)
- Fluorescent beads of 0.26 μm size (SPHERO^{TM} Fluorescent Sky Blue, Spherotech Inc.)
- Plant glue (PlantFix liquid (Dupla)
- Two component silicone glue (picodent twinsil)
- Methylene blue (Sigma-Aldrich Chemie GmbH, CAS Number: 122965-43-9)
- Refractometer (Model TAbbeB, TEC++ DR. VOLKER SCHMIDT GMBH)
- FEP tubing of 1.05 mm inner diameter and 50 μm wall thickness, (Karl Schupp AG)
- PTFE (Adtech Polymer Engineering Ltd):
  1.76mm ID x 0.2mm Wall +/-0.05mm, Adtech part number: STW14
- Glass capillaries (BLAUBRAND, intraMark glass cuvettes # 708744):
- OptiPrep / iodixanol (Stemcell Technologies, Catalog # 07820)
- PBS
- Lasers: 488 nm & 594 nm (Omicron-Laserage Laserprodukte GmbH), 685 nm (Obis, Coherent, Inc)
- Fluorescent filters: 488 nm LP EdgeBasic, 594 nm LP EdgeBasic, 692 LP (all Semrock, IDEX Health & Science, LLC and ET700 LP (Chroma)
- Camera: ORCA-Flash4.0 V2, Hamamatsu

3.10 Concluding Remarks

In this chapter, I have introduced the concept of optical aberrations induced by refractive index mismatch in biological specimens and shown how they can impair imaging at different depths and scales. Further, I have shown an experimental approach, tailored to *in vivo* light-sheet microscopy, on how to reduce aberrations in 4 different model organisms. The results are further backed up by a image quality measures based on spectral analysis. I therefore conclude, that *in vivo* refractive index matching is a useful approach to reduce aberrations, restore resolution, and minimize imaging artefacts for *in vivo* recordings across scales.

The approach shown here is not mutually exclusive with other image contrast enhancing techniques, such as the commonly used electronic confocal slit detection in light-sheet microscopy [73]. In fact, correcting the excitation beam's position across the FOV will have positive effects on the confocal line readout. Restoring the PSF shapes across the recorded 3D volume will also improve deconvolution approaches, as they are typically based on theoretical PSF models, or PSFs extracted from ideal imaging conditions. And most importantly, I expect refractive index matching to support adaptive optics approaches in the future. Reducing the aberrations arising from the sample geometry via RI matching, also reduces the low order aberrations typically corrected with deformable mirrors in adaptive optics. Therefore, the aberration correction with the adaptive optical element does not require to cover as high of a dynamic range any longer, and instead can be used for the correction of higher order aberrations with better precision.

Ideally, other compounds for RI matching will emerge in the future, which are also biocompatible and will allow for RI changes in the culture medium of mammalian samples, such as the mouse embryo. Further, a larger selection of objectives with multi-immersion capabilities, also covering the higher NA range, would be beneficial for fluorescent microscopy. As a last point, I would like to mention the link to the simulation approaches introduced in this chapter: With the growing computational power of modern GPUs, more precise simulations will become possible, as well as simulations on larger volumes. A 3D segmentations with subsequent aberration estimation for an average RI of the sample, will be a good starting point for addressing possible artefacts or resolution limitations. Even an initial guess for the wavefront correction in adaptive optics could results form such an approach. All together, I expect the interplay of simulations, RI matching and adaptive optics, to push light-sheet microscopy to greater depths, in the spatial, but also in the quantitative context.

4 Dual-View Light-Sheet Microscope for Mammalian Samples

When light-sheet microscopy opened the vault for embryological studies in 2004 [14], it also brought science closer to understanding our own developmental origins. One decade after successfully demonstrating that high spatio-temporal 3D-recordings of developing *Drosophila melanogaster* embryos and *Medaka* larvae were possible [14], the first light-sheet microscope devoted to study pre-implantation mammalian embryos, more precisely *Mus musculus* embryos was realized at the EMBL [60]. The microscope is capable of recording high resolution data up until day 3 of the embryonic development, corresponding to the 64 cell stage of the embryo. With single cell tracking and statistical analysis, the authors were able to show that cell fate determination occurs for the first time around the 16 cell stage. In the following years, a number of studies have been successfully completed, focussing on intra-embryonic events, *e.g.* on chromosome segregation during the first cell divisions [95]. The microscope's open-top configuration, the multi-sample imaging capabilities, as well as the incubation enabled studies on other mammalian samples such as mammary acini [69] and bovine embryos [111]. In recent years, similar microscope configurations were adapted to study *Drosophila* embryos in a microfluidics environment [70], pathological samples [112]. Additionally, the configuration was adapted and commercialized by Luxendo GmbH in 2016 [113].

The shared open-top configuration of the mentioned systems offers the advantage of easy sample access and mounting, as well as quantitative high-throughput imaging along the perpendicular axis of the objective configuration plane. As any SPIM configuration with a single illumination and single detection lens, this type of microscope setup suffers from unwanted light-tissue interactions. Resulting shadowing effects and inhomogeneous illumination profiles can make quantitative analysis difficult. Further, the effective imaging depth in the sample can be limited. Especially scattering and aberrations can lead to low signal to background ratios in few tenths of micrometers depth, ergo inhibiting *in toto* recordings. A possible inexpensive

improvement is the addition of a second illumination objective as originally demonstrated by Huisken and Stainier [53]. An open-top setup offering dual-illumination was realized to study intestinal organoids [114], and has been commercialized by Luxendo, Bruker Corp [54] and Viventis Microscopy Sàrl [115]. As organoids of few 100 μm in size are an optically challenging sample, the addition of a second illumination direction visibly improves the overall sampling and imaging quality [114].

In the standard upright SPIM configuration [14][16][55] the samples are usually mounted with the help of a cylindrical support, *e.g.* a glass capillary and/or fluorinated ethylene propylene (FEP) tubing as well as hydrogel. Sample rotation is then realized along the long axis of this cylindrical geometry with a rotation stage. Views from multiple angles can then be combined to a more isotropic three-dimensional dataset. A possible further improvement in resolution and contrast can be gained via multi-view deconvolution [116][117][118]. For *in toto* recordings across spatio-temporal scales, *e.g.* cell divisions and tissue folding during *Drosophila melanogaster* development, multi-view light-sheet microscopy based on dual detection and dual illumination objectives has become the go-to technique in recent years [55][56][57][67]. The simultaneous detection from two opposing sides enables the dual-sided 3D recording of the volume of interest at no extra expense of the photon budget. If scattering can be suppressed, the detected planes can be added mathematically instead of going through a more complex image fusion process [73][118]. The resulting 3D volume typically exhibits a higher overall signal to noise level, a more homogeneous resolution, and in optically challenging samples as *Drosophila melanogaster* and organoids of larger size, is the preferred mode of imaging. This is particularly due to the simultaneous detection where biological events on the ~second time scale could otherwise not be synchronized between views, and where light-sensitive samples demand a careful usage of the available photon budget.

In summary, the currently available open-top light-sheet microscopes offer flexibility and easy sample access through their geometry, making them ideal high-throughput platforms for quantitative mammalian studies in 3D. However, these systems struggle to accommodate for image quality degradation at greater depths. At the same time, resolving intra-cellular processes is of great interest for our understanding of the early mouse embryo's development. Events as cell division, chromosome segregation or intra-cellular protein localization require quantitative studies at the highest possible spatio-temporal resolution *in vivo* imaging can offer.

I addressed this limitation by implementing a second high NA detection objective lens in a new open-top geometry. There, the two detection objectives are opposed to one another in

the horizontal plane, while the illumination is performed from below. This system effectively doubles the amount of detected light and enables multi-view fusion to compensate for image quality loss at larger depths. At the same time, the high-throughput character is upheld by a redesign of the sample mount. To bridge the gaps between different mammalian samples, I introduce a flexible illumination scheme, based on extended or *pushed* light-sheets which can be controlled in length adaptively. Further, I show a readjustable detection arm which can be modified to either offer simultaneous dual colour detection or sequential channel detection at larger FOVs. In the following sections I will describe the optical and mechanical design of the inverted pushed light-sheet selective plane illumination microscope, short: **InPuLS-SPIM**. A rendering of the full system can be seen in Fig. 4.2. It serves as a primary overview of the system and its layout before the following sections will detail the different units.

It should be noted that this microscope was initially conceptualized by Jan Ellenberg, Lars Hufnagel, and Yu Lin (Ellenberg group), and subsequently redesigned from ground up, built, characterized, and brought to operation by me. The precision stages, filter wheels, software, and the necessary hardware control unit based on an FPGA (field programmable gate array) were purchased from Luxendo, Bruker Corp. and tailored in collaboration to our needs. Here, I

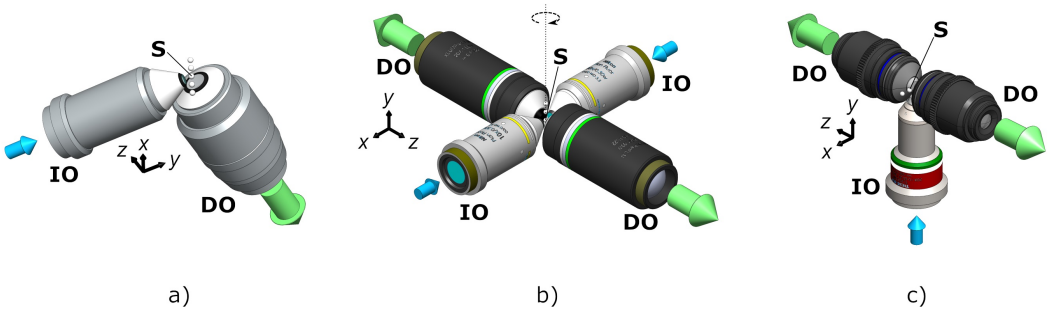

Figure 4.1: InVi-, MuVi, and InPuLS-SPIM configurations. The open-top configuration of the InVi-SPIM in a), offers flexible sample (S) access and high-throughput imaging along the *x*-axis. In its original design and in other follow-up configurations (see main text), only one illumination objective (IO) and one detection objective (DO) are used for imaging. The MuVi-SPIM configuration, shown in b), on the other hand offers dual illumination, dual detection, and sample rotation around the *y*-axis. A more isotropic sampling and higher quality recordings are therefore possible. Contrary to the InVi-SPIM, multi-sample mounting is limited and has be be performed along the *y*-axis, effectively stacking the specimens on top of each other. The novel InPuLS-SPIM introduces a second detection objective to the inverted configuration of the InVi-SPIM as shown in c) and uses a high NA illumination objective for extended light-sheets (see main text). High-throughput imaging is again possible along the *x*-axis with access from the top. Further, the recordings benefit from the simultaneous dual-view detection with high NA objectives. The illumination directions are indicated with blue arrows, while the detection directions are marked by green arrows. Small spheres are used to visualize the direction of the multi-sample mounting axes.

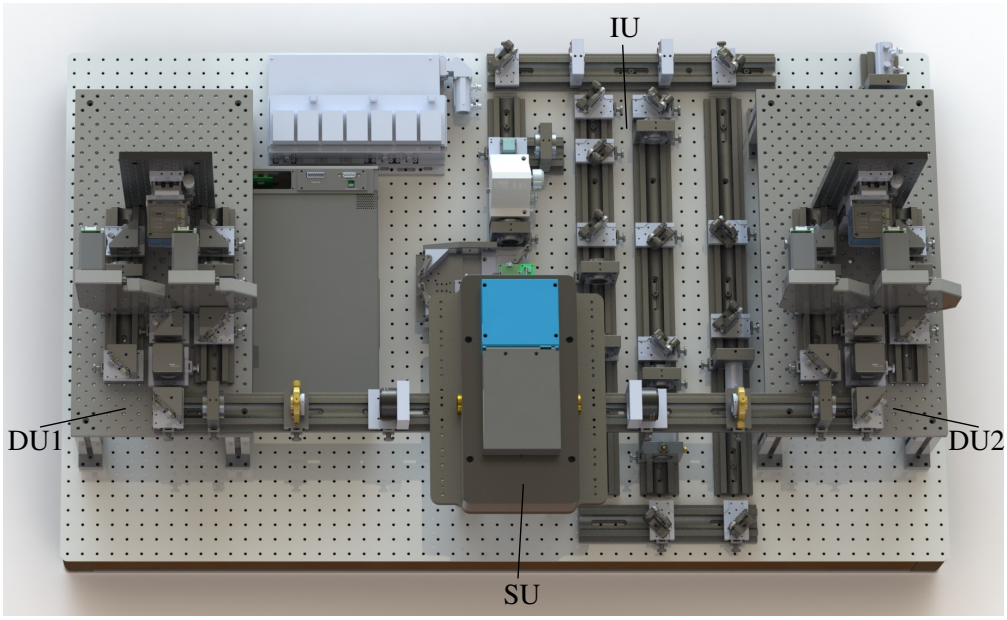

Figure 4.2: 3D rendering of the InPuLS-SPIM. The system consists of four main units which will be discussed in more detail in the following sections. In the center the sample unit (SU) is found, elevated on aluminium legs that allow the mounting of an objective, and illumination from below. It is flanked by two likewise elevated detection units (DU1 & DU2) which are symmetric to one another and entail the same components. The fourth unit is the illumination unit (IU), occupying approximately half of the optical table, in parts underneath the detection and sample unit. The electronic control box (Luxendo, Bruker Corp) and the laser combiner (Omicron-Laserage Laserprodukte GmbH) are located on the left side of the optical table, partially underneath the left detection unit.

received valuable support from Dr. Bálint Balázs. The software design or control will therefore not be part of this chapter. However, a similar software design and hardware control strategy is described in [118]. This microscope and its custom sample mount have been filed as a European patent under the number *EP 21191351.2*.

4.1 Sample Unit

The core of the microscope, the sample unit, is designed around the sample chamber with two detection objectives (NA = 1.1) and one illumination objective (NA = 0.6). As the illumination is performed from below, the illumination objective positioning and the required mirror demand an elevation of the sample unit. For better access and flexibility, I chose the optical plane of detection be be at a height of 250 mm.

The size and geometry of the three objectives further defines the dimensions and movement ranges of the sample holder. As a high-throughput during image acquisition is desired, a large travel range in the x-dimension, similar to the InVi-SPIM [60], is required. Therefore, the combination of precision rails and piezo motors found in the TruLive system[1] [54] served as a basis for the sample unit. The TrueLive's design encompasses one motor for the long axis translation in x, two motors for y-axis, as well as two motors for z-axis movement. The two yz-translation units are located in front and behind the sample chamber, spanning across two long flanking precision rails. They are connected via two stainless steal rods and the sample mount holder with each other. The design allows for movements of the sample mount of

$$[\Delta x, \Delta y, \Delta z] = [50.0\,\text{mm}, 10.0\,\text{mm}, 0.6\,\text{mm}]$$

The full sample unit without the cover and without the incubation add-on is shown in Fig. 4.3.

[1] Also referred to as the TruLive3D Imager

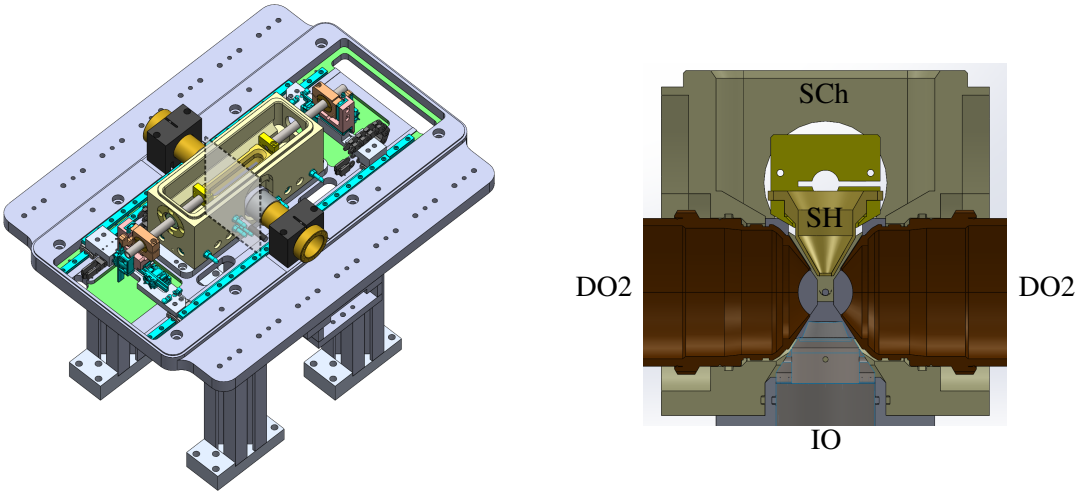

Figure 4.3: InPuLS-SPIM - sample unit. The elevated sample unit is designed and built around the sample chamber and the objective arrangement. It is presented in full in a). The rails for x-translation flank the sample chamber, while the other precision rails and motors can be found on two units in front and behind the sample chamber. The grey trapezium indicates the location of the cross-section, which is presented in b). Here, the two detection objectives (DO1 & DO2) and the illumination objective (IO) are shown in their arrangement in relation to the sample holder (SH) as well as the sample chamber (SCh).

Sample Mount

In the past, thin plastic foils made out of FEP with a refractive index close to water proved efficient for mouse embryo [60] and acinii imaging [69] at the EMBL. I therefore chose to use a similar system, adapted to the new geometry of the InPuLS-SPIM. A sample holder made out of polyether ether ketone (PEEK), together with a shaped FEP foil make up the sample mount. The geometrical constraints due to the objective lens assembly requires a change of the otherwise comparatively flat V-shaped sample mount. For good optical access, the protrusion of the FEP foil was extended, following a U-shape, such that the sample is located 4 mm below the sample holder (*cf.* Fig. 4.4). To shape the foil accordingly, I designed two moulds that can be used in combination. While one presents the outer boundary of the U-shape, the other mould pushes the FEP foil through the opening into the sample holder. A shallow longitudinal cavity in the outer mould, paired with fine extensions on the inner mould, can be used to generate pockets in the FEP foil. This can be of help for samples such as pre-implantation mouse embryos.

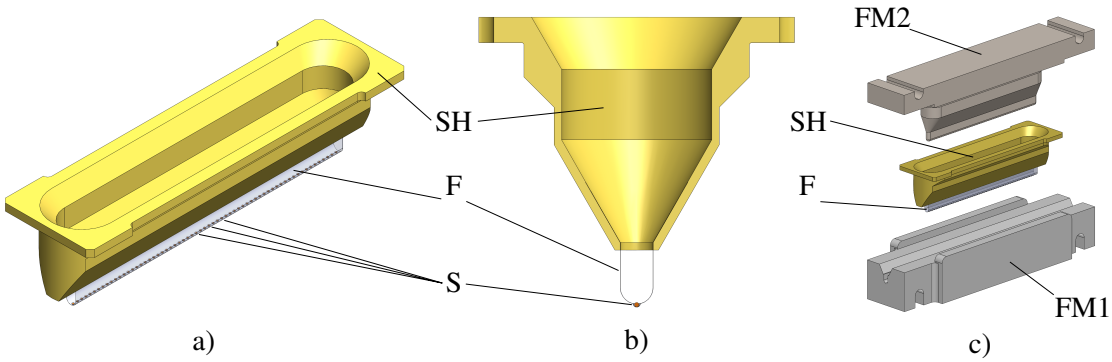

Figure 4.4: Sample mount of the InPuLS-SPIM and its assembly. The sample mount, shown in a), is comprised of the sample holder (SH) and the FEP foil (F), connected by bio-compatible glue. The specimens (S) are located at the bottom of the U-shaped foil, ≈ 4 mm from the PEEK sample holder, in indentations in the foil. A cross-section of the sample mount is shown in b). For the assembly process, two foil moulds (FM1 & FM2) are used. An exploded view is shown in c).

Alternatively, a capillary with a round tip, or similar objects, can be used to manually indent the foil after sample mount assembly.

4.2 Detection Unit

As the primary goal with this system is to record light-sensitive mammalian samples in the range of 20 μm to 200 μm, with a focus on preimplantation mouse embryos of < 100 μm size, it is important to be as light-efficient as possible on the detection side. We chose to use two 60x, 1.1 NA detection objectives from Olympus (LUMFLN60XW) as they offer a maximum field of view of ~ 300 μm at a working distance of 1.5 mm[2]. In the existing InVi-SPIM setup [60] simultaneous dual colour detection was implemented via a double dichroic mirror configuration with which two different channels could be recorded with the same camera sensor. However, FOVs on the camera were displaced diagonally from each other. In this instance, the diagonal displacement on the sensor prevented the implementation of the electronic confocal slit detection (eCSD) [73] as the light-sheet position needs to be synchronized to the camera readout. Under diagonal channel displacement, this effectively means the presence of two light-sheets for the camera, preventing the readout synchronisation. Camera readout with the eCSD, ensures that only light from the current position of the light-sheet is collected. Only pixels that match the light-beam's position while it is being scanned, are read out by the sensor. This means that light which reaches other parts of the sensor is likely scattered light and does not contribute positively to the overall image quality. As eCSD is a contrast enhancing feature from which specifically multi-view microscopy benefits, my aim was to enable simultaneous dual colour detection on one camera sensor while using the eCSD and maximizing the overall usable detection area. This can be achieved by splitting the two colours with a single dichroic mirror, and later recombining the two colours on the chip via a prism mirror (*cf.* Fig. 4.5). Please note that in this scenario, it is advantageous to recombine the two detection paths as close to the sensor as possible, such that colour crossovers on the chip can be avoided. This configuration further allows to treat the two colours completely separately before recombination, *e.g.* different magnifications or focus corrections can be applied. Small offsets of the FOVs can also be corrected by changing the mirror positions and angles.

[2]The detection objectives have a field number of 26.5 mm, divided by the magnification, resulting in ~ 442 μm. If one then takes the square shape of the detector into account and divides further by $\sqrt{2}$, it becomes evident that a square sensor can at best record an area of ~ $300 \times 300\,\mu m^2$.

The simultaneous dual colour detection path per detection side encompasses the following optical components:

- 60x, 1.1 NA detection objective with 1.5 mm working distance and a effective focal length of 3 mm (Olympus, LUMFLN60XW)
- Tube lens, $f = 180$ mm (Thorlabs, TTL180-A)
- Dichroic mirror, separation edge at 560 nm (Semrock, FF560-FDi02-t3-25x36)
- Three custom relay lenses $f \approx 150$ mm, each made out of 2×300 mm lenses (Edmund Optics, #49-378)
- Set of fluorescence filters in a filter wheel (filter wheel provided by Luxendo, Bruker Corp: 488 LP Edge Basic Longpass (AHF, F76-490), 525/45 BrightLine HC (AHF, F37-521), 550/49 BrightLine HC (AHF, F37-551), 561 LP Edge Basic Longpass Filter (AHF, F76-561), 594 LP Edge Basic Longpass (AHF, F76-594), 700 LP ET Longpass-Filter (AHF, F47-070)
- Multiple elliptical mirrors (Thorlabs, BBE1-E02)
- Dove prism (Thorlabs, PS995M)
- Knife edge prism (Thorlabs, MRAK25-P01)
- Back illuminated sCMOS camera with 95 % peak quantum efficiency, with 2048×2048 pixels, and a pixel size of $6.5 \times 6.5\,\mu m^2$ (PCO, pco.panda 4.2 bi)

A layout sketch of the right detection arm can be found in Fig. 4.5 while a more detailed 3D rendering is shown in Fig. 4.6.

At $M = 60$, the effective FOV on the camera sensor is $2048 \times 6.5\,\mu m/60 \cong 222\,\mu m$, leaving $\sim 100\,\mu m$ for each colour, including a small region of overlap. The detection unit can be transformed to standard light-sheet (widefield) detection path, offering a larger field of view and higher quantum efficiency as any unnecessary optical components are omitted. To achieve this configuration a filter wheel and the camera need to be moved onto the precision rail (*cf.* Fig. 4.5 & Fig. 4.6). Simultaneous colour detection is then replaced by sequential colour detection through filter change between stack recordings. This configuration is also particularly useful for troubleshooting and alignment of the system as less possible sources of error are present. Both

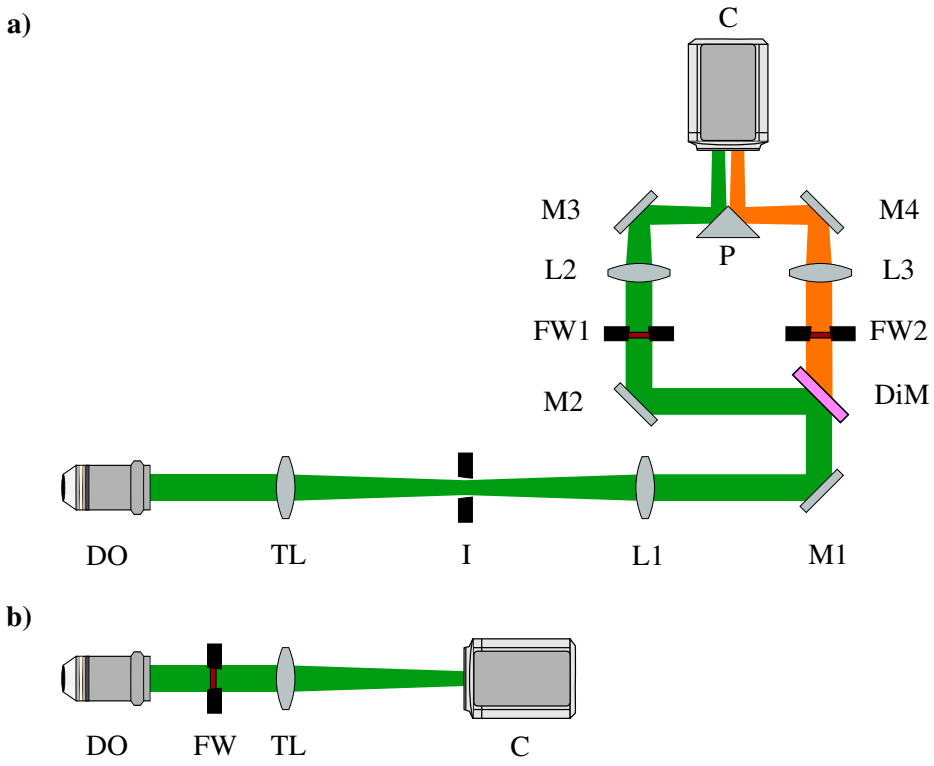

Figure 4.5: InPuLS-SPIM - Sketch of the detection path. The two possible detection modes are shown. In a) the dual colour detection scheme is presented. Here, the combined light from the detection objective (DO) is relayed through the tube lens (TL) and lens L1 towards the colour-splitting unit. An Iris (I) in the intermediate image plane can be used to define the size of the FOV. After being reflected at mirror M1, the light is separated the the dichroic mirror (DiM). Light of a wavelength below $\sim$ 560 nm is reflected towards mirror M2 where it passes through a fluorescence filter in filter wheel FW1. Light of longer wavelengths, *e.g.* $>$ 560 nm, passes through the dichroic mirror and a fluorescent filter in filter wheel FW2. Please note that two extra mirrors have been omitted for simplicity. Following the fluorescence separation and filtering, the two separate detection light beams are focussed via lenses L2 and L1 respectively. Another pair of mirrors M3 & M4 together with the knife edge prism P eventually guide the light onto the camera C and its sensor. Two separate images on the sensor are the result. The detection path is mirrored for the left detection unit. In b) a standard light-sheet (widefield) detection path is shown. Colours can be recorded sequentially in this arrangement. One can obtain this configuration by moving a filter wheel and the camera to the indicated positions. This allows to image a larger FOV and collect more photons.

cameras are positioned on fixed precision rails and the detection objectives are mounted in a way that only allows for marginal movement along the optical axis. This is advantageous for initial alignment and long-term stability, but can lead to two offset FOVs among the two detection arms. To address this possibility, I designed two camera mounts which are compatible with the Owis precision rail system. While one mount is designed to compensate for a vertical offset, the other compensates for possible horizontal displacements. Both axes offer a translation range of ±5 mm, which corresponds to ~ 80 μm or ~ 40 % of the FOV at magnification of 60 (*cf.* Fig. 4.7). Different magnifications are also easily achieved via exchange of the tube lens, *e.g.* with a tube lens of 300 mm focal length f_{TL}:

$$M = \frac{f_{\mathrm{TL}}}{f_{\mathrm{DO}}} = \frac{300}{3} = 100$$

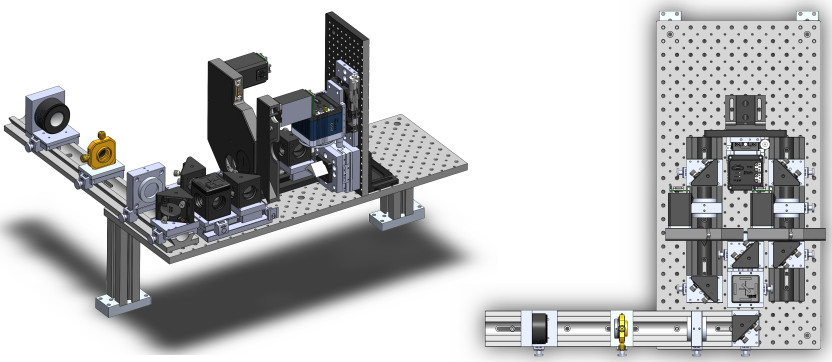

a) b)

Figure 4.6: InPuLS-SPIM - 3D model of the dual colour detection unit. A 3D rendering of the right detection arm starting with the tube lens is shown here. The arm is elevated above the optical table by four aluminium legs and allows for access below the breadboard. Apart from two extra mirrors after the dichroic beamsplitter, the layout corresponds to the sketch in Fig. 4.5. In a) a cross section through the breadboard is displayed to showcase the vertical mounting of the camera and knife edge prism. This orientation is necessary to rotate the image such that the light-sheet moves from the top of the camera sensor to its bottom. To flip one of the images by 180°, a dove prism (not shown) can be attached to the mirror mounts. Otherwise the simultaneous dual-channel eCSD readout of the sensor is not possible. The knife edge prism is mounted on a precision stage and can be adjusted in height and distance to the camera. A top view of the full detection arm is presented in b). The left detection arm is mirrored and consists of the same components.

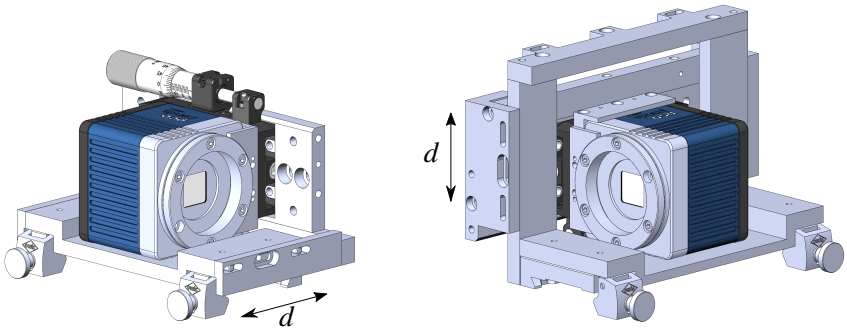

a) b)

Figure 4.7: InPuLS-SPIM - 3D model of the camera mounts. The two different camera mounts for single channel detection are displayed here. In both cases, the camera can be transferred with its original precision stage and mount (*cf.* Fig. 4.6 a)) to the here shown single channel mounts and vice versa. As the the mounts are built around Owis' rail system, the riders allow for movement along the rail for course focussing. The precision stage (Thorlabs, XRN25P/M) then enables fine focussing. The assembly in a) shows the camera mount on the left detection arm, where movement along the horizontal axis is possible. The construction in b) allows for movement in the vertical axis. Together these movements ensure a well overlapping FOV on both camera sensors. Stability and precision are maintained via the guidance through four stainless steel pins and two screws for fixation.

4.3 Illumination Unit

Recent studies in mammalian organisms [60][95] and in fish [74] have highlighted the importance of being able to image at subcellular resolution in a multi-cellular or organismal context. For such studies a high spatio-temporal resolution is of essence and the high NA detection optics additionally profits from thin light-sheet illumination, enhancing contrast and axial resolution. With this microscope we therefore aimed to not only improve the detection efficiency via a second detection lens, but also to design a system capable of bridging the scales from single to multi-cell imaging via adaptable light-sheet illumination. For this purpose regular Gaussian beam based illumination has its limitations, especially because of non-uniform intensity distribution along the axis of illumination, but also because of its changing width.

Soon after light-sheet microscopy found its regular application in biological imaging, a number of studies investigated potential effects on the image quality when non-Gaussian illumination profiles were used. Among the non-Gaussian illumination profiles, Bessel beams[3] were among the first successfully used profiles [84][18] as they offer a thin core over longer lengths than a regular Gaussian beam. This comes at the cost of exceeding intensity in the outer rings of this illumination profile, potentially leading to increased photodamage and background intensity in the image. In an effort to suppress the outer ring structure of the Bessel beam profile, Chen *et al.* introduced the lattice light-sheet [68] which in its essence can be seen as the addition of several Bessel beams along one axis, such that the side lobes are reduced due to destructive interference. Other illumination profiles encompass the so-called Airy beam [119], a profile which exhibits a curvature away from the axis of illumination. Alternatively, one can also tile regular Gaussian light-sheets and effectively generate extended illumination profiles [120][121]. In this latter illumination approach, recording and stitching of several image tiles around the focus of the light-sheet, results in a dataset of higher image quality. If tiling is not desired, *e.g.* when imaging speed is important, a rapid shifting or *'pushing'* of the illumination beam's focus can generate an extended illumination profile with similar characteristics to a Bessel beam [122].

This type of illumination can be realized with a tunable acoustic gradient (TAG) lens. TAG lenses belong to category of so called gradient index (GRIN) lenses and use a refractive index gradient distribution to refract light, rather than different substrate thicknesses. In the case of the

[3]Please note, that true Bessel beams are impossible to generate as they would require infinitely large apertures and optics. In microscopy one can only generate Bessel beams of finite length in which the properties are a mixture between Gaussian and Bessel beams. Therefore, they are often called finite Bessel beams or Bessel-Gaussian beams. For the sake of simplicity they will be referred to as Bessel beams throughout this work.

TAG lens, a liquid is used to generate radial refractive index gradients via acoustic drivers. The change in refractive index happens in the range of several kHz and is therefore a multitude faster than the typical camera exposure times in light-sheet microscopy, *e.g.* $< 100\,\text{ms}$. The rapid re- and defocussing capability of such a lens has found application in microscopy on the detection side [123][124], where an extended depth of field is advantageous, but also on the illumination side, *e.g.* in light-sheet microscopy [122][125][126] where an extended thin illumination profile has been implemented. In fact, the TAG lens can be driven in such a way that it will generate Bessel beams if desired [127][128]. Based on previously reported successful illumination approaches with the TAG lens for single cell imaging [122] as well larger organisms, *e.g.* zebrafish [126], we chose to implement a similar illumination scheme. To generate the thinnest core possible in the illumination profile, a high NA illumination objective is required. The choice of high NA illumination objectives with a long working distance is limited however, as the objective needs to fit in between the two detection objective lenses. For the here presented geometry, I chose to use a 20x, 0.6 NA illumination objective with 5.5 mm working distance (TL20X-MPL, Thorlabs). The arrangement of the three objectives can be seen in Fig. 4.1 c).

4.3.1 The Pushed Light-Sheet

As touched upon in chapter 2.2, the resolution in light-sheet microscopy can be improved along the detection axis z in comparison to regular widefield detection if a thin sheet is used in illumination (*cf.* 2.30). Here, I want to illuminate this concept in greater depth and illustrate that for certain ranges, a gain in resolution as well as a more homogeneously illuminated specimen can be achieved. For this purpose, I simulated possible extended light-sheets and effective point spread functions across scales to understand whether resolution improvements can be achieved (*cf.* Ch. 4.3.2). The profile of a 0.6 NA Gaussian beam, corresponding to a fully illuminated back aperture of the objective lens, is displayed in Fig. 4.8, next to a regular Gaussian beam of $100\,\mu\text{m}$ length. To estimate the dimensions of the Gaussian beam formed by a 0.6 NA objective lens and a laser with a wavelength of 488 nm, the $1/e^2$-width of the Airy disc was taken as a reference for the beam waist:

$$w_0 \approx 0.41 \frac{\lambda_0}{\text{NA}} = 333.5\,\text{nm} \tag{4.1}$$

$$\text{FWHM} = \sqrt{2 \ln 2}\, w_0 = 392.7\,\text{nm} \tag{4.2}$$

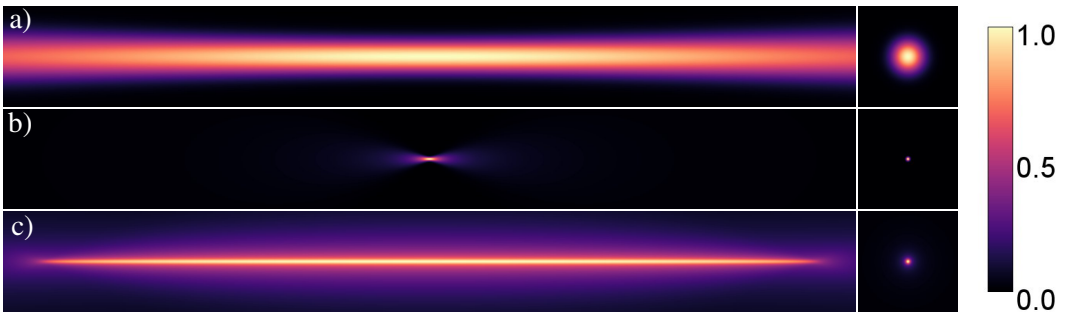

Figure 4.8: Regular vs. pushed light-sheet simulation. The sum along the z-axis of three simulated light-sheet profiles generated with different NAs and methods are presented here. For consistency with the coordinate system on the detection side, x is the axis of propagation, while z corresponds to the optical axis of the detection objective. The right column shows the beam cross sections in the center of the beams (yz-profile). In a) a regular light-sheet of 100 μm length is shown, while b) displays a short light-sheet generated at 0.6 NA illumination. In c) a simulated profile of a pushed beam with a 100 μm length, including its central cross section, is shown. For this simulation the short light-sheet shown in b) was translated from left to right until the desired length was reached. All intensities were normalized to 1.0 (*cf.* intensity scaling on the far right in [arb. unit]). The wavelength was set to 488 nm. The pixel size corresponds to 50 nm and the total simulation volume was $[x, y, z] = 4401 \times 257 \times 257$ voxel. The full FOV presented here corresponds to 110 μm $\times$ 12.8 μm, and 12.8 μm $\times$ 12.8 μm for the right column respectively.

By using Eq. 2.26 one can estimate the axial extent or length of the light-sheet:

$$z_{\mathrm{R}} = \frac{n\pi w_0^2}{\lambda_0} = 952.3\,\mathrm{nm} \tag{4.3}$$

As the TAG lens can shift the focus along the illumination axis with a variable extent around the zero position, it is possible to cover the length of the reference beam and compare the beam profiles. In the simulation of the pushed light-sheet, a repetitive pixel-wise displacement and summation of the high NA focussed beam was used to simulate the final intensity profile. As an example, a pushed light-sheet of the same length as the reference beam is displayed in Fig. 4.8.

One note to make here regarding the simulations of the pushed Gaussian beams, is the non-linear behaviour the TAG-lens shows in reality. While the simulations here uses a linear focus displacement, the de- and refocussing with a liquid lens result in extra time spent on the edges of the chosen focal range. This sinusoidal movement of the focus results in additional intensity at the beam ends, with a dip at the center of the beam (*cf.* Figs. 4.13 & 4.14). This has been reported before [122] and can in principle be addressed via rapid patterned laser modulation [126] or an ultra fast Pockels cell which can control the intensity directly [125]. In this work however,

the profiles are simulated with a linear translation and without additional laser modulation.

4.3.2 Effect of Pushed Light-Sheet on System PSF

While the two long light-sheets in Fig 4.8 are well suited to illuminate samples of $\sim 100\,\mu$m size, the bridge to samples of smaller scale is of particular interest, *e.g.* single cells or smaller regions inside a developing mammalian embryo. With decreasing light-sheet length also the beam diameter decreases in size. As mentioned in Chapter 2.2, the z-resolution of a light-sheet microscope can be increased once the light-sheet thickness reaches the axial extent of the detection PSF. One extreme case can be seen in Fig. 4.9 where the light-sheet had a width of $w_0 \approx 330\,$nm. Such thin light-sheets are also of short lengths, with a Rayleigh range of $z_R < 1\,\mu$m, and therefore of no particular use for live imaging. Nonetheless, the extent of the system's effective PSF is reduced by 50 % and can be regarded as a theoretical lower boundary for the here presented setup.

To understand how the pushed light-sheet profile affects the system's effective PSF in comparison to regular Gaussian light-sheet illumination, I simulated and compared the PSFs across the two different light-sheet profiles for the three different imaging scales referred to earlier: $20\,\mu$m, $50\,\mu$m, and $100\,\mu$m. Of particular interest is not only the PSF at the center of the light-sheet, but also at the ends of its length. The detection PSFs were modelled using a modified implementation of the Gibson-Lanni model [129] while the system's effective PSFs are the product of the detection PSF and the light-sheet profile (*cf.* Eq. 2.17). Note that the coordinate system used for the simulations corresponds to the camera coordinates of the microscope system, with z denoting the optical axis of the detection objective[4]. The results for a Gaussian and a pushed beam with $\lambda_0 = 594\,$nm and a length of $50\,\mu$m are summarized in Fig. 4.10.

The simulations predict, that for extended beams as presented here, an increase in resolution can be achieved across different scales (*cf.* App. **??** for the $100\,\mu$m and $20\,\mu$m regimes). Further, the more even intensity distribution along the illumination axis allows for homogeneous excitation and fluorescence detection in the sample of interest.

[4]The Rayleigh length will nonetheless be defined as z_R for consistency.

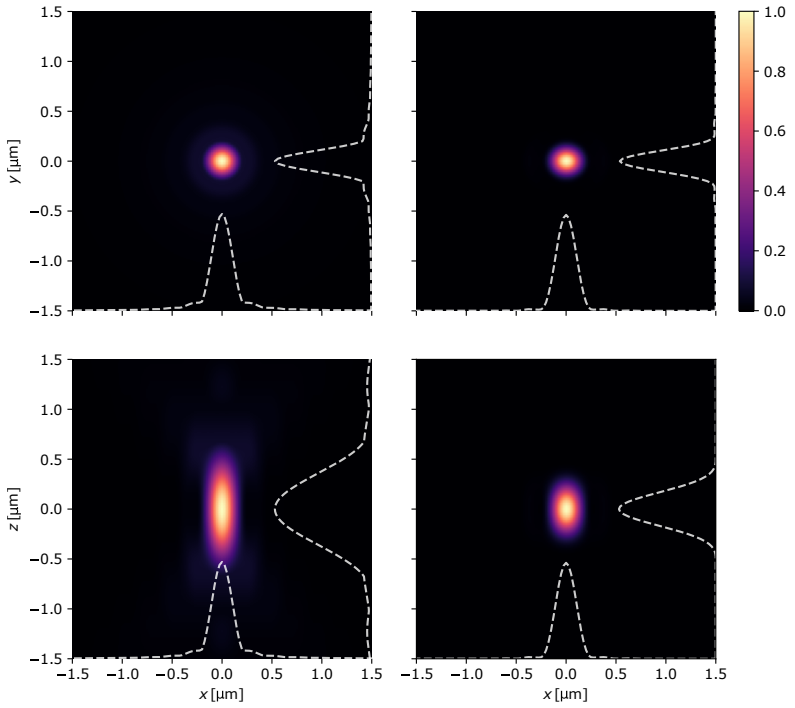

Figure 4.9: Regular 1.1 NA PSF vs. combined PSF with 0.6 NA LS illumination. The effect on the axial extent of the system's effective PSF under illumination with a thin light-sheet is shown here. The left row displays maximum intensity projections of a regular PSF simulated with the Gibson-Lanni model for an NA = 1.1 and $\lambda = 510\,\text{nm}$. The dimensions are $\text{FWHM}_{xy} \approx 0.25\,\mu\text{m}$ and $\text{FWHM}_z \approx 0.75\,\mu\text{m}$. The cross-sectional intensity profiles, all normalized to 1 arbitrary unit in amplitude are shown with dotted lines inside the graphs. The right column shows the system's effective PSF after multiplication with the illumination profile of a thin light-sheet as shown in Fig. 4.9 (b). While the *xy*-profile, apart from a minor suppression of the Airy pattern's side lobes, is mostly unaffected, the extent in z is clearly noticeable. The dimensions of the combined PSF are $\text{FWHM}_{xy} \approx 0.25\,\mu\text{m}$ and $\text{FWHM}_z \approx 0.37\,\mu\text{m}$, effectively reducing the extent in z by 50 %. All intensities were normalized to 1 arbitrary unit. The simulation volume was $[x, y, z] = 513 \times 513 \times 513$ voxel with a voxel size of $25\,\text{nm}^3$.

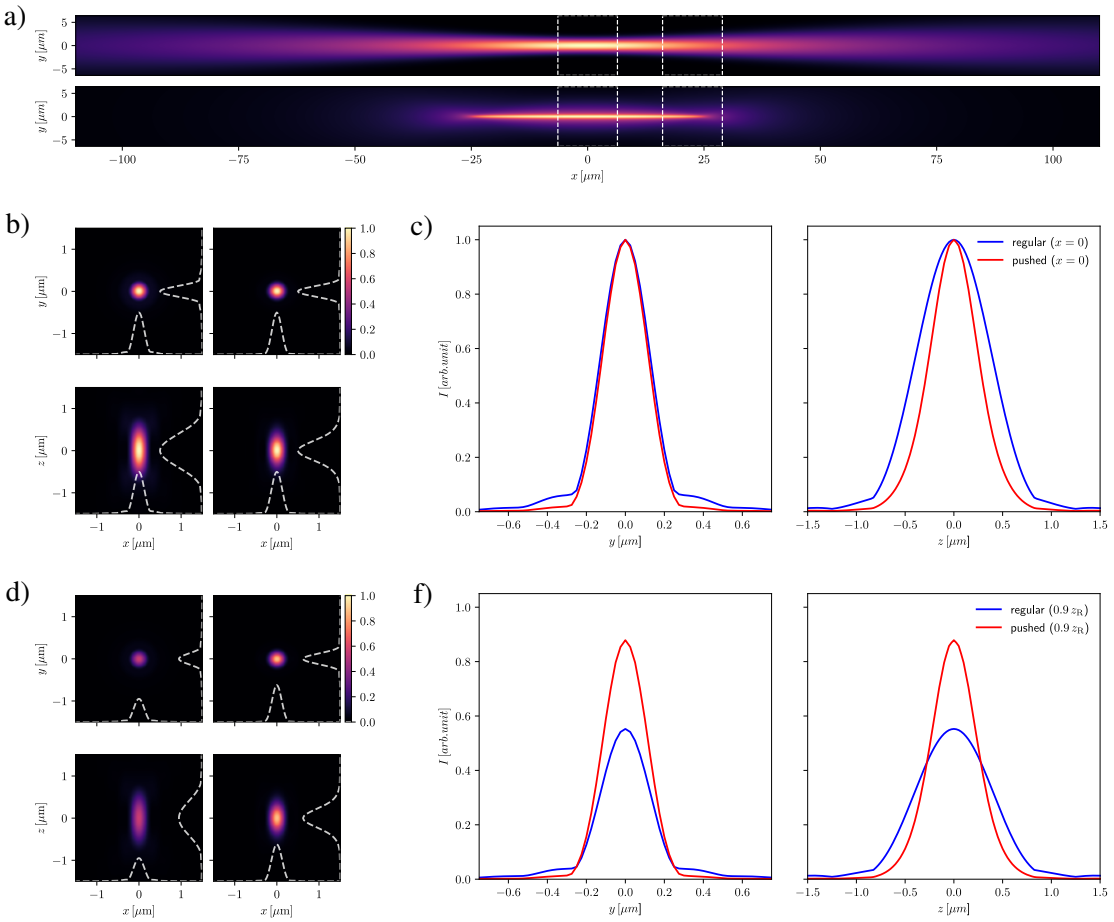

Figure 4.10: Regular Gaussian beam vs. pushed light-sheet - effects on system's PSF. Both simulated beams of $50\,\mu$m length are shown as sums along the z-axis in a). The dotted lines in the regular Gaussian beam (upper image) and the pushed beam (lower image) indicate the volume used for the downstream PSF simulations. The central region is located exactly at $x = 0$ while the second region is located around the Rayleigh length $x = 0.9z_R$. The system's effective PSF at the center of the respective region is calculated via a multiplication of the light-sheet and detection PSF volumes as done in Fig. 4.9. Maximum intensity projections of the effective PSF for the center of the illumination beam are shown in b). The z-extent of the detection PSF is reduced from $\mathrm{FWHM}_{\mathrm{RegLS}} = 0.9\,\mu$m to $\mathrm{FWHM}_{\mathrm{PuLS}} = 0.6\,\mu$m. The cross-sectional intensity profiles are plotted in c). Maximum intensity projections of the PSF at $x = 0.9z_R$ is displayed in d). The Gaussian beam's intensity drop-off results in a clear reduction of the PSF's intensity. The pushed beam's intensity reduced by $\sim 10\,\%$ and the axial extent of effective PSF reaches $\mathrm{FWHM}_{\mathrm{PuLS}} = 0.6\,\mu$m. All intensities were normalized to 1.0 arb unit at the center of the beam profiles. The PSF simulation volume was $[x, y, z] = 513 \times 513 \times 513$ voxel with a voxel size of $25\,\mathrm{nm}^3$.

4.3.3 TAG Lens Optics and Illumination Unit Design

With the theoretical advantages and limitations of light-sheet illumination based on the use of liquid lenses discussed above alongside simulated results, I will focus on the optical and mechanical design of the illumination unit in this section.

The first component of any light-sheet illumination unit, is the laser. We chose to use the LightHub from Omicron-Laserage Laserprodukte GmbH with the following diode lasers (peak wavelength ±5 nm & power after fibre output):

- 488 nm, 41.8 mW
- 561 nm, 41.0 mW
- 594 nm, 44.0 mW
- 685 nm, 33.0 mW

A single mode optical fibre in combination with a collimator produced a Gaussian beam of ~ 3 mm thickness. The aforementioned 20x illumination objective (TL20X-MPL) offers a NA = 0.6 and is designed for the use of tube lenses with a focal length of $f_{\mathrm{TL}} = 200$ mm. Ergo, the effective focal length of the illumination objective is

$$f_{\mathrm{IO}} = \frac{f_{\mathrm{TL}}}{M} = \frac{200\,\mathrm{mm}}{20} = 10\,\mathrm{mm}\,. \tag{4.4}$$

The aperture size $\varnothing_{\mathrm{IO}}$ of the illumination objective can further be estimated via

$$\varnothing_{\mathrm{IO}} = 2\mathrm{NA}f_{\mathrm{IO}} = 12\,\mathrm{mm}\,. \tag{4.5}$$

For an optimal focus spot, it is desirable to completely fill or better overfill the back aperture of the illumination objective lens. In our case this means that the initial beam originating from the optical fiber needs to be magnified at least 4x before it reaches the illumination objective lens. At the same time, the TAG lens (TAG LENS 2.5 BETA) has a physical aperture of its own, which is listed at 16 mm. The effective apertures vary with driving signal and amplitude and peak at 11 mm for comparatively low optical powers[5]. At larger optical powers the effective aperture falls to 4 mm or even 2.3 mm at higher frequencies. It is therefore useful to be able to controllably fill the aperture of the TAG lens, depending on the required optical power. I

[5]The optical power is the inverse of the focal length: $P = 1/f$. Its unit is m^{-1} or one dioptre and is the choice of unit in the specification sheet of the TAG lens.

found that this can be achieved well with an iris right before the TAG lens. However, one can estimate the needed optical power by considering the maximally needed focal shift in the sample space. For the large FOV under sequential multi-colour detection, the maximum needed extent amounts to $\sim 200\,\mu$m. The possible scan range Δ_x inside the sample chamber can be estimated via [130][122][126][6]

$$\Delta_x = 2\left|\frac{n \cdot f_{\mathrm{IO}}^2}{f_{\mathrm{TAG}} \cdot M_{\mathrm{TAG}\to\mathrm{IO}}^2}\right| . \tag{4.6}$$

Here, n denotes the refractive index of the immersion medium, f_{IO} the focal length of the illumination objective (*cf.* Eq. 4.4), f_{TAG} the focal length of the working TAG lens and $M_{\mathrm{TAG}\to\mathrm{IO}}$ summarizes the combined magnification from the TAG lens to the back aperture of the illumination objective. Please note, that f_{TAG} can be positive and negative as the lens de- and refocusses the beam. Further, it can be seen that a large intermediate magnification from the TAG lens to the illumination objective, reduces the scan range inside the sample chamber. At the same time our aim is to fill or overfill the back aperture of the illumination objective to generate the smallest possible spot size. To estimate the needed optical power or focal length of the TAG lens for a $\sim 200\,\mu$m FOV, we solve Eq. 4.6 for f_{TAG}

$$|f_{\mathrm{TAG}}| = 2\frac{n \cdot f_{\mathrm{IO}}^2}{\Delta_x \cdot M_{\mathrm{TAG}\to\mathrm{IO}}^2} . \tag{4.7}$$

Now considering the needed magnification from the TAG lens to the back aperture of the illumination objective, we can calculate the maximally required focal length of the TAG lens at 11 mm aperture. In this instance the intermediate magnification becomes

$$M_{\mathrm{TAG}\to\mathrm{IO},\,max} \geq \frac{12\,\mathrm{mm}}{11\,\mathrm{mm}} \approx 1 .$$

Contrary to the low optical power regime, higher optical powers, *e.g.* $P = 20\,\mathrm{m}^{-1}$, can be achieved at higher frequencies, resulting in smaller effective apertures of the TAG lens. For the smallest mentioned effective aperture in the specification sheet of 2.3 mm, we find

$$M_{\mathrm{TAG}\to\mathrm{IO},\,min} \geq \frac{12\,\mathrm{mm}}{2.3\,\mathrm{mm}} \approx 5$$

[6] The relationship is described in the supplementary information of the cited work.

while at intermediate driving frequencies of 190 kHz and an effective aperture of 4 mm we get

$$M_{\mathrm{TAG}\rightarrow\mathrm{IO},\,med} \geq \frac{12\,\mathrm{mm}}{4\,\mathrm{mm}} \approx 3\,.$$

With these results it is now possible to estimate the required focal lengths of the TAG lens for these three aperture regimes, including the corresponding optical powers:

$$\left|f_{\mathrm{TAG},\,max}\right| \approx 1300\,\mathrm{mm} \qquad \Rightarrow P_{max} \approx 0.75\,\mathrm{m}^{-1} \tag{4.8}$$

$$\left|f_{\mathrm{TAG},\,med}\right| \approx 150\,\mathrm{mm} \qquad \Rightarrow P_{med} \approx 6.67\,\mathrm{m}^{-1} \tag{4.9}$$

$$\left|f_{\mathrm{TAG},\,min}\right| \approx 50\,\mathrm{mm} \qquad \Rightarrow P_{min} \approx 20.00\,\mathrm{m}^{-1} \tag{4.10}$$

These focal lengths are all based on approximately filling the back aperture of the illumination objective. If one chooses to overfill the back aperture, *e.g.* by a factor of $\sqrt{2}$, the focal lengths due to the inverse quadratic relationship to the magnification would shorten by a factor of 2. In turn, the optical powers would double. It becomes then evident, that the driving signal frequency in the lower range ($\sim$ 70 kHz, larger effective apertures) is on the very edge of producing usable extended beams. A promising frequency range on the other hand is found at $\sim$ 190 kHz (4 mm aperture).

One more constraint on the design of the illumination unit is the galvanometric scan mirror (GSM) and its size. For optimal scanning along the y-axis at the specimen location, the GSM needs to be conjugated to the back focal plane of the illumination objective. In turn, the TAG lens should also be conjugated to the same plane. It can therefore be relayed to the position of the GSM. For additional alignment and to have translational degrees of freedom at the focus, an extra relay lens pair and a mirror in between the GSM and the TAG lens can be used. In sum, this means there are three conjugate planes to the BFP distributed across the illumination unit. We chose to use a scan mirror from Scanlab (dynAXIS 3 T) with a 8.5 mm aperture. This allows a beam magnification of $\sim$ 1.5 between the TAG lens and the GSM without significant beam clipping[7] From the GSM to the back aperture of the objective, an additional factor of at least 2 is necessary. To ensure the usage of the full NA, we magnify by a factor of 3.

In addition to the TAG lens illumination, an extra arm for regular scanned Gaussian light-sheet illumination is included. Depending on the chosen demagnification of the initial beam, different

[7]The beam diameter is specified through the $1/e^2$-diameter and accounts for 86 % of the power. To transmit $\sim$ 99 % of the beam's power, one should calculate with an additional factor of $\sim$ 1.5.

beam lengths and widths can be realized. The two arms need to be recombined before the GSM via a beamsplitter or a removable, *e.g.* magnetically mounted, mirror. The estimation of the needed parameters for the Gaussian beam are straightforward. As an example, we solve for the necessary parameters of a reference Gaussian beam with a length of $2z_R = 100\,\mu$m. Using Eq. 2.26, the required beam width inside the sample chamber is

$$w_{0,\,\mathrm{reg}} = \sqrt{\frac{\lambda_0 z_R}{n\pi}}\,. \tag{4.11}$$

With the vacuum wavelength $\lambda_0 = 488\,$nm, a desired Rayleigh length of $z_R = 50\,\mu$m and the refractive index of the immersion medium $n = 1.33$, we get $w_{0,\,\mathrm{reg}} \approx 2.4\,\mu$m (FWHM $\approx 3.28\,\mu$m). The angle of divergence follows (*cf.* Eq. 2.27)

$$\alpha_{\mathrm{reg}} = \frac{\lambda_0}{n\pi w_{0,\mathrm{reg}}} \approx 2.77°\,. \tag{4.12}$$

From here, the effective numerical aperture of the beam can be calculated using

$$\mathrm{NA}_{\mathrm{reg}} = n \sin\alpha_{\mathrm{reg}} \approx 0.064\,. \tag{4.13}$$

Using geometric relationship between the focal length of the illumination objective f_{ill}, the input beam diameter b_{reg}, and the divergence angle α_{reg}, we find for the input beam diameter

$$b_{\mathrm{reg}} = 2n \sin\alpha_{\mathrm{reg}} \cdot f_{\mathrm{ill}} = 2\mathrm{NA} \cdot f \approx 1.29\,\mathrm{mm}\,. \tag{4.14}$$

As we have a 3x magnification after GSM, the beam size of the reference beam before the GSM should be $\sim 0.43\,$mm in diameter. Later, a beam of $\sim 50\,\mu$m length will be shown. It is realized by a $\sim 0.6\,\mu$m beam diameter before the GSM and by a demagnification of 4.

With the above presented constraints and parameters, the optical layout of the illumination unit can be arranged as shown in the sketch in Fig. 4.11.

For the construction on the optical table, OWIS precision rail system was used. With it, the optical height is fixed at 65 mm and lens positioning can be achieved with $\sim 0.1\,$mm precision. For long-term stability, constrained movement along optical axes, as well as fast exchange of components, such systems are beneficial as the number of degrees of freedom is greatly reduced. The 3D rendering from the SolidWorks model of the illumination unit is displayed in Fig. 4.12.

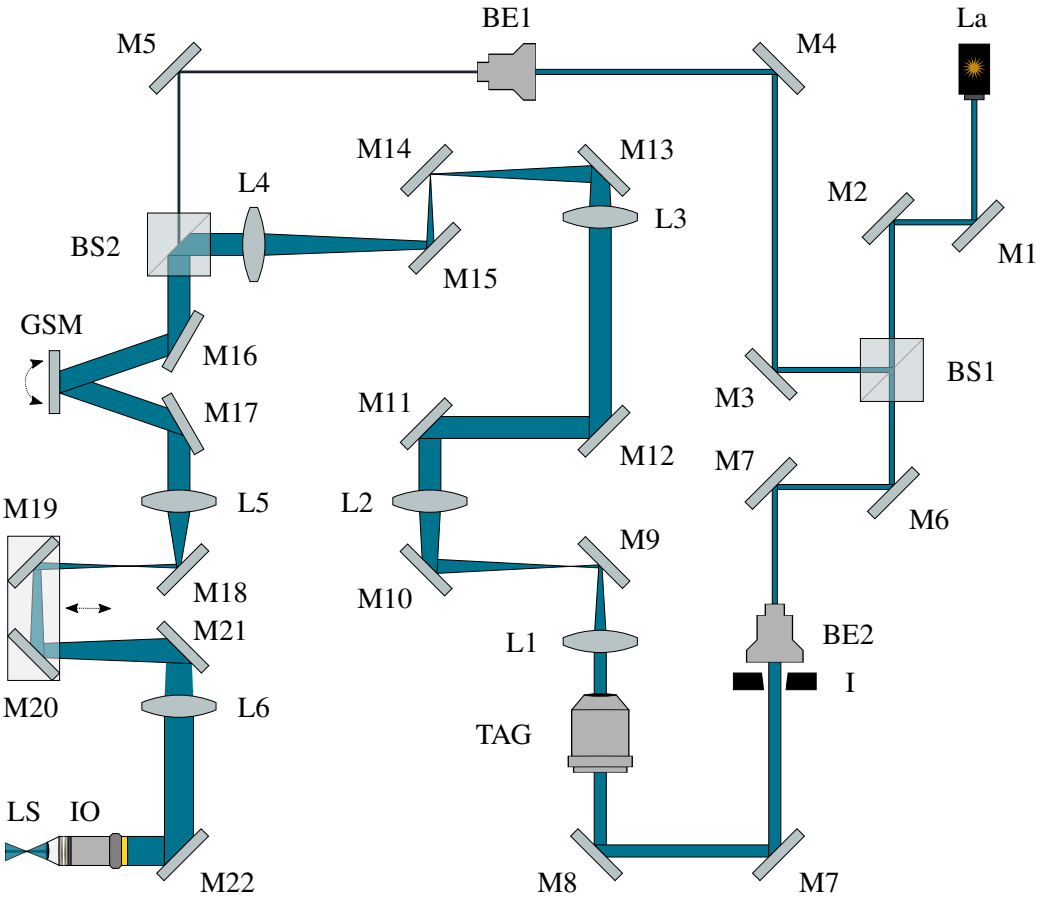

Figure 4.11: InPuLS-SPIM: Beam path of the illumination unit. The sketch shows the two beam paths for regular light-sheet illumination and pushed light-sheet illumination. The emitted light from the laser (La) is guided to a beam splitter (BS1), where the two different paths begin. The upper path is defined by mirrors M3 to M5 and a demagnifying beam expander (BE1). The lower path consists mainly of a 3x beam expander (BE2), an Iris to clip the beam if desired, the TAG lens (TAG), and a relay optics. Lens L1 and L2 conjugate the TAG lens onto mirror M12 and expand it by factor 1.5. L3 and L4 in turn conjugate M12 onto the galvanometric mirror (GSM) at a 1:1 ratio. The GSM is also conjugated to the BFP of the illumination objective (IO) via L5 and L6. These lenses expand the beam by another factor of 3 to overfill the BFP of the illumination objective. After the the objective, a regular light-sheet (LS) from the upper beam path is generated, or a focal spot from the TAG lens path. Mirror M22 reflects the beam up, away from the optical table as the illumination in the sample chamber is inverted and comes from below. Most mirrors are helpful for alignment and are not discussed individually. Apart from M12, which can be used for translation in the image plane, M14 is at a useful position as it allows for tip/tilt movements of the beam in the image plane. Further, M18 to M21 are used to fold the beam once. M19 and M20 are located on a precision rail and can further be used for beam displacement along the illumination axis.

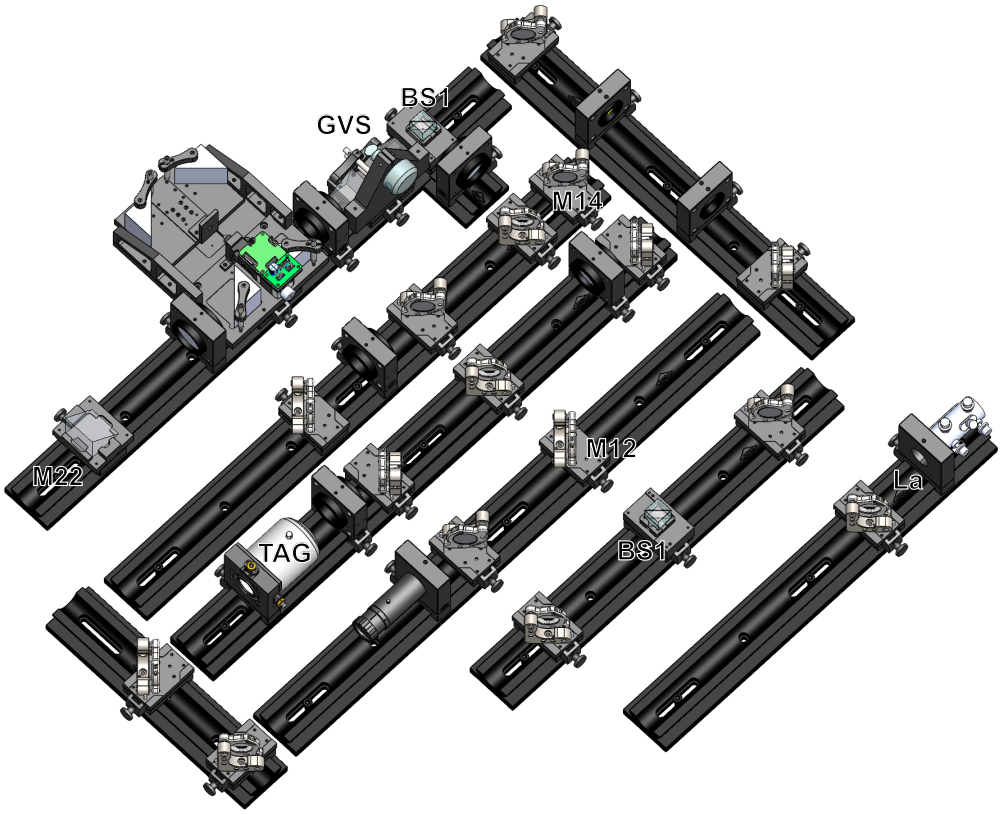

Figure 4.12: InPuLS-SPIM: 3D rendering of the illumination unit. A 3D model of the illumination unit is presented here. Relevant optical components corresponding to the sketch in Fig. 4.11 have been indicated for better overview.

4.4 Optical Alignment and Operation

In the following paragraphs, I will introduce the alignment procedure of the system, which degrees of freedom are essential, as well as the different modes of imaging. Please refer to Fig. 4.11 for better understanding.

Alignment of Illumination Unit

For best light-sheet de- and refocussing, the TAG lens should be conjugated to the back focal plane of the illumination objective. The same is true for the GVS. Further, an additional conjugated plane can be used for light-sheet translation in the image plane. Therefore, the first steps in the assembly and the alignment, is to place the relay optics and necessary mirrors at the theoretical positions. Then, beginning from the light-source, the collimated output from a single mode fibre, the first two mirrors (M1 & M2) are used to ensure the laser beam follows the rail system at a 65 mm height. This is done with the help of two irises. By tilting two displaced mirrors along two axes each, in total four degrees of freedom can be addressed: Vertical displacement & tilt, and horizontal displacement & tilt. The now aligned beam gets separated in two at the beamsplitter cube BS1.
The regular or reference light-sheet path begins with mirror M3. Together with mirror M4 the beam can be aligned to pass through beam expander BE1 (*e.g.* $M_{\mathrm{BE1}} = 1/4$) on-axis. Mirror M5 is then used for light-sheet tilt in the image plane. Rotation of the GVS is used for light-sheet scanning and an additional flexure on the GVS mount enables displacement of the illumination plane.
The light-path used to generate the pushed light-sheet, begins with mirror M6 which together with mirror M7 is used to stir the beam on-axis through beam expander BE2 ($M_{\mathrm{BE2}} = 3$). An iris can be used to control the final beam diameter before the light reaches the TAG lens or right after. Another mirror pair (M7 & M8) is used to pass through the TAG lens on-axis. For fine adjustments, the TAG lens itself can also be moved vertically and horizontally with the help of a translation mount (Thorlabs ST1XY-S(/M)). Lens L1 ($f_{\mathrm{L1}} = 100\,\mathrm{mm}$) and lens L2 ($f_{\mathrm{L2}} = 150\,\mathrm{mm}$) are used to relay the TAG lens plane onto mirror M12. Mirrors M9, M10 & M11 are used for on-axis alignment. Lenses L3 & L4 ($f_{\mathrm{L3}} = f_{\mathrm{L4}} = 150\,\mathrm{mm}$) relay the Tag lens further onto the GSM. Mirrors M13, M14 & M15 are used for on-axis alignment before the two light-paths are recombined at beam splitter BS2. Note, that mirror M14 lies in the focus of lenses L3 & L4. Therefore, tilting of M14 introduced translation on the GVS and rotation in

the image plane. Together with the tilt of mirror M12, these two mirrors provide the necessary four degrees of freedom in the image plane. Apart from mirror pair M19 & M20, which can be translated on a precision stage parallel to the optical axis, all mirrors are fixed. The translation of this mirror pair can be used for minor axial displacements of the focus position. As we want to take full advantage of the full 0.6 NA of the illumination objective lens, it is crucial to have precise alignment and aberration free beam expansion across the system. To achieve this, I use shear plate interferometers (Thorlabs SI100 & SI254) to minimize possible aberrations in between the various relays. As most commercial lenses have an error tolerance of at least $1-2\,\%$, minor corrections on the lens positions need to be performed iteratively from lenses L6 and L5, back to L2 and L1, with possible mirror displacements. This is rather straight forward and due to the rail system and achieved in few minutes time. One final degree of freedom is given by the illumination objective itself as it is mounted in a custom tubing. It is held in place by a combination of a spring loaded disk and a threaded adjustment ring that can be used to move the objective along its optical axis.

Alignment of Detection Unit

Depending on the mode of operation, the detection unit can be adjusted to mimic a simple widefield detection unit, consisting only of a filterwheel, a tube lens and the camera. This has previously been referred to as the single channel detection mode (*cf.* Fig. 4.5 b)). Here, each detection arm has the option to move the tube lens for focussing, as well as the precision stage, the camera is mounted upon. The custom camera mounts shown in Fig. 4.7 further allow to either displace the cameras vertically or horizontally for better overlap of the two FOVs. The alignment needed in this configuration is minimal and straightforward.

In the case of simultaneous dual channel detection (*cf.* Fig. 4.5 a), the cameras are mounted on a vertical breadboard, pointing down to the main breadboard. Following the detection light path after the detection objective, the tube lens generates an intermediate image at the beginning of the detection arm. This image is then relayed via the lenses L1 and L2/L3, respectively. After lens L1 the detection beam is redirected via a mirror M1 towards the dichroic mirror DiM where it is spectrally separated. Adjusting mirror M1 therefore affects both arms. As it is located closely to L1, the image rotation is minimized. After passing the filter wheels, the detection beam becomes focussed by lenses L2 & L3. It is redirected by mirrors M3 & M4 towards the upward pointing knife edge prism P. As the two lenses are once again located closely to the adjustable mirrors

M3 & M4, rotation of the mirrors mostly translates the image on the sensor, and introduces little rotation. This is crucial as otherwise a rotated image plane will appear aberrated. Note, that L2 & L3 do not have to be in a 4f-configuration with L1, but can have longer or shorter distances from it. Theoretically, different magnifications between the two channels are possible. The knife edge prism should ideally be located as close as possible to the camera C, as the overlap of the two channels on the sensor is then minimized. Adjusting the height of the prism via the precision stage it is mounted on (Thorlabs DTS25/M), allows to bring the two channels into closer proximity of one another or to separate them further. Altogether, the adjustments and the alignment needed is kept at a minimum, as it improves long-term stability or the accidental introduction of imaging artefacts. For initial on-axis alignment, a miniature laser can be placed before the tube lens TL and co-aligned with the optical axis with the help of two irises.

Note that the orientation of the downwards pointing cameras in the simultaneous detection arrangement needs to be combined with a dove prism (Thorlabs PS995M, not shown) in one of the two colour paths for for simultaneous use of the confocal line scanning mode in both channels. Otherwise, the images will appear flipped by 180° on the camera sensor. Therefore, the excitation beams will appear to move in opposite directions and the confocal line scanning readout can only be performed for one of the channels.

4.5 Optical Performance and Example Applications

After construction of the microscope, the first aim was to validate that the TAG lens can be used to generate light-sheets of various lengths at the predicted driving frequencies of ~ 190 kHz and ~ 300 kHz. Further, their intensity profiles were investigated as a thin core region is at the essence of possible resolution improvements in the z-axis.

Next, fluorescent microspheres of 0.1 μm size, below the diffraction limit, are imaged to quantify the optical performance.

Finally, the correct mechanical precision and alignment can be validated by comparing the overlap of the two FOVs from both detection objectives. This goes hand in hand with example recordings of fluorescent mouse embryos where we expect the fusion of both stacks to lead to a dataset of higher image quality than the individual stacks.

4.5.1 TAG Lens Generated Extended Light-Sheets

After the assembly and alignment of the microscope, I proceeded to investigate the performance of the TAG lens and its limitations. From the simulations under ideal conditions (*cf.* Ch. 4.3.1), we expect to achieve illumination profiles with a thin core over the entire FOV. With growing length, the thickness and background intensity is expected to increase. For sufficient detection signal, I used a low concentration methylene blue solution in the sample chamber and excited it with the laser of 594 nm. Example profiles as detected at $M = 60$, are presented in Fig. 4.13. As a reference profile, a Gaussian beam of ~ 50 μm length is displayed, as well as the full NA focal spot.

Already visible by eye, is the inhomogeneous intensity distribution along the core of the beams. This is due to the sinusoidal driving of the TAG lens and has been reported by others [122][126]. The FWHM along the illumination-axis are lowest at the ends of the beam profiles which corresponds the to location of maximum intensities. At the center of the beam, the intensity shows a dip of ~ 10 % and an increase in width. This can be explained by the residing times of the focus, which are averaged out during the camera readout. As the focus resides longer at the ends of the pushed light-sheet, the average profile in these regions is more confined. In contrast, the focus is swept across the central region linearly. Additionally, while the focus is near the ends of the beam, the wide tails of the focus are contributing to the intensity profile in the central region. The result is a lower and broader intensity profile in the center, as seen in Fig.

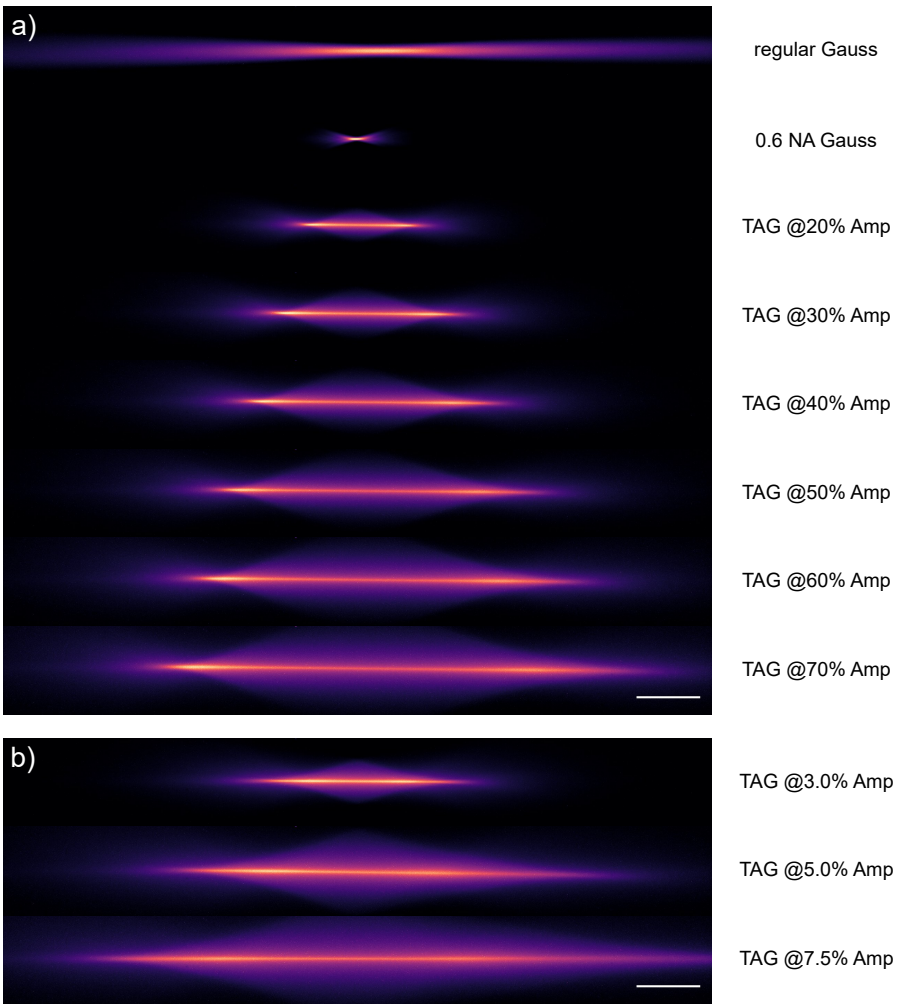

Figure 4.13: InPuLS-SPIM: Recorded light-sheet profiles. A number of possible light-sheets is presented here. In a), a regular light-sheet of approx. 50 μm length is shown above the focal spot resulting from the fully used 0.6 NA. The pushed light-sheets below were generated by driving the TAG lens at $\sim$ 190 kHz and the given amplitudes specified on the right-hand side. Driving the TAG lens at $\sim$ 300 kHz and lower amplitudes, results in the three example profiles shown in b). All images were normalized to an intensity of 1.0 arb unit. The displayed intensity range corresponds to 0.1 to 0.9 arb unit. Scale bars: 20 μm.

4.14 b), c) & d).

A direct comparison with the shown Gaussian beam is challenging and should be performed with caution. The previously shown simulations were based on ideal intensity profiles where model parameters could be extracted easily. Gaussian beams of different lengths and widths were shown, but under experimental conditions, or after alignment of the system, only a single length of a regular Gaussian beam is available. We chose to explore the regime of the 50 μm beam as it spans across the core of a mouse embryo, offering best resolution in the center, while still giving a good overview of the entire embryo. It is shown at the top of Fig. 4.13. Noise, aberrations, and the uneven intensity distribution, render the extraction of length and width of the TAG lens generated beams challenging. I therefore define the usable length of a pushed light-sheet not by its width, but by its intensity profile along its propagation axis. Different from the regular Gaussian beam, the intensity drop-off is rather steep and therefore we define the point in the illumination profile where the intensity drops below 70 % as the end of the beam (*cf.* Fig. 4.14 b)).

A beam of similar length is then also used in Ch. 4.5.3 to image a fixed mouse embryo. The here performed characterization serves as a reference for the TAG lens generated light-sheets in the following section.

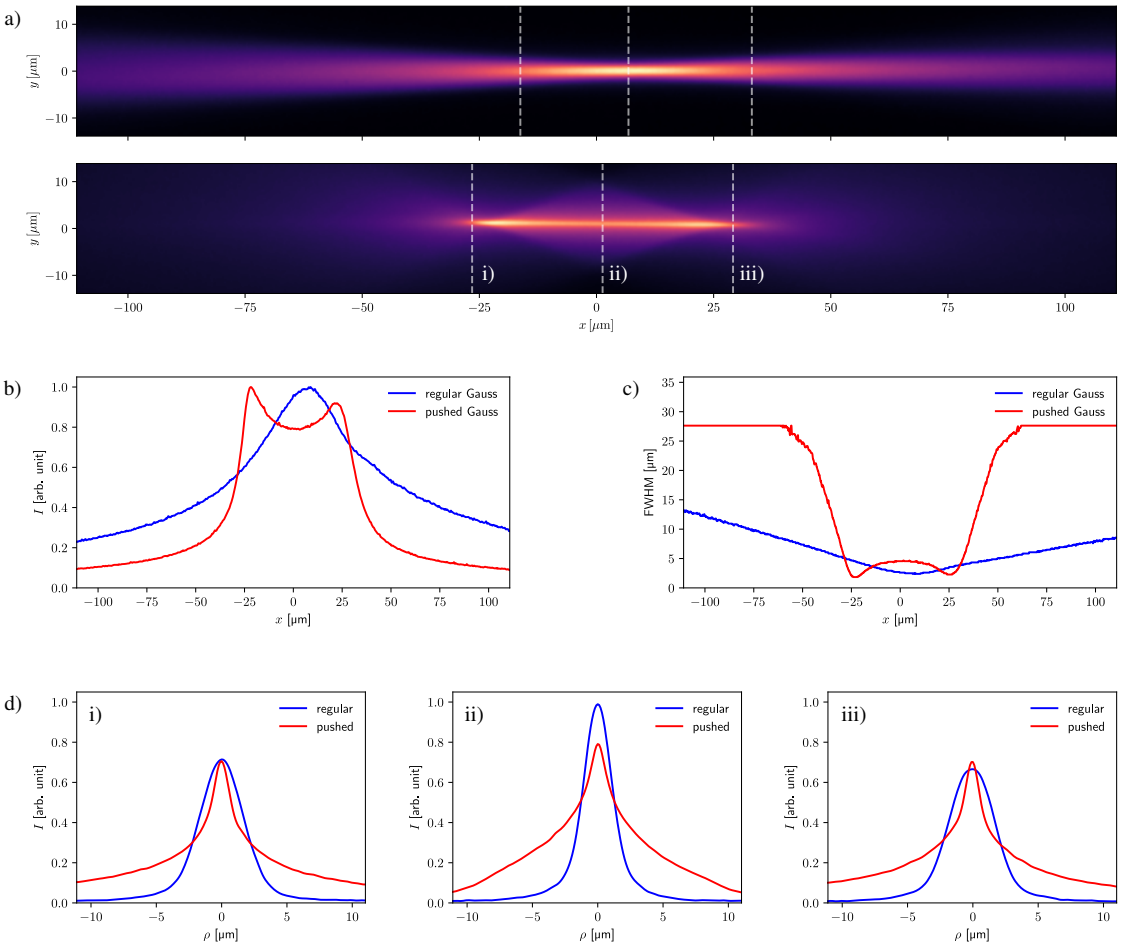

Figure 4.14: Recorded Gaussian vs. pushed beam. A Gaussian beam of length 49.4±1.5 μm is compared with a pushed beam of 55.7±1.5 μm length. Both beams are shown as average intensity profiles in a). Dashed lines indicate the beginning i), the center ii), and the end iii) of the light-sheets. The two differing intensity profiles of the beams are illustrated in b). Note the dip in intensity of the pushed beam and the two peaks at the beam's start and end regions. The FWHMs along the propagation axis are plotted in c). Similar to the intensity, the widths actually increase in the center and decrease at the start and end regions of the pushed beam. The Gaussian beam follows a typical Gaussian behaviour. The intensity cross-sections of the three marked regions in a) are plotted in d). At the starting point i) the two beams exhibit FWHMs of 3.9±0.2 μm (Gauss) and 3.1±0.2 μm (pushed). The end of the beams iii) displays similar widths with a FWHM of 4.0±0.2 μm for the Gaussian beam and 3.0±0.2 μm. The central region holds the Gaussian beam's smallest FWHM of 2.4±0.2 μm while the pushed beam has a FWHM of 4.6±0.2 μm. Both beams were normalized to 1.0 arb unit intensity. The length of the pushed beam was defined as the point were the detected intensity dropped below 70 %.

4.5.2 Optical Performance Based on Fluorescent Bead Imaging

After validating the performance of the extended light-sheet, I characterized the PSF of the system under both modes of detection. For this I transformed the left detection arm into the dual channel configuration shown and described in 4.2. The right detection arm remained in the single channel configuration. This way a validation of the relay optic and colour splitting in the dual channel detection arm is possible. I used 0.1 nm sized fluorescent beads (FluoSpheres), with an absorption peak at 580 nm and an emission peak at 605 nm, mixed in gel (Gelrite) of 0.8 % concentration. To avoid possible aberrations from the FEP foil of the sample mount, I used a glass capillary filled with the mixture of gel and beads, to pierce through the membrane and extruded the gel 1 mm down below the sample mount. To avoid unwanted movements, I stabilized the glass capillary in the sample mount's cavity with additional gel.

The spectral separation under the simultaneous dual-colour detection arrangement (left view), lead efficiently to a half sided detection of the light-sheet ($\lambda_0 = 594$ nm) and fluorescent beads on the sensor. The left sensor half, which is designated for signals in the spectrum below $\lambda = 561$ nm displayed no significant signal. The FOV of $\approx 100\,\mu$m was illuminated by the pushed light-sheet with the TAG lens driven at 190 kHz and an amplitude of 50 %. The results of the PSF extraction are shown in Fig. 4.15.

To estimate the average PSF over the FOV, I selected 16 beads for each camera with the FIJI plugin PSF Tool 3D (Mosaic tool box, based on work by [131]) from which via centroid fitting, an average 3D profile is generated. That profile is displayed on the right hand side next to the respective full FOVs in Fig. 4.15 a) & b). For optimum quality, I imaged fluorescent beads within the first 100 μm of the extruded gel cylinder for each view individually, *i.e.* the two presented bead volumes do not match. Otherwise aberrations caused by the gel would affect one of the views. The extracted PSF profiles were then used to fit Gaussian profiles within the built-in function of FIJI. The resulting fit-parameters include the Gaussian standard deviation which needs to be multiplied by $2\sqrt{2\ln(2)}$ to reach the here shown FWHM.

The PSF estimate for the left view (simultaneous dual channel detection arrangement, index

l) and for the right view (single channel detection arrangement, index *r*) results in:

$$\mathrm{FWHM}_{xy,\,l} = 361.2\,\mathrm{nm} \tag{4.15}$$

$$\mathrm{FWHM}_{z,\,l} = 1598.4\,\mathrm{nm} \tag{4.16}$$

$$\mathrm{FWHM}_{xy,\,r} = 417.3\,\mathrm{nm} \tag{4.17}$$

$$\mathrm{FWHM}_{z,\,r} = 1354.0\,\mathrm{nm} \tag{4.18}$$

In the lateral, as well as the axial extent, the PSFs extracted from the bead recordings, are larger than the predicted theoretical PSFs (*cf.* Fig. 4.10), where the Gibson-Lanni model predicted a lateral extent of $\mathrm{FWHM}_{xy,\,t} = 270\,\mathrm{nm}$ and an axial extent of $\mathrm{FWHM}_{z,\,t} = 900\,\mathrm{nm}$. Present aberrations are the likely cause of the larger measured PSFs. A possibility, not explored in this experiment, is the correction with the collar on the detection objectives. As it is designed to correct aberrations, *e.g.* introduced by 'brain sample index mismatch'[8], it can potentially be used to compensate for the here seen effects. I decided to keep it at constant position for the aqueous solution and hydrogel, as it can also introduce unwanted aberrations if adjusted to the wrong position for the respective imaging medium. In the future, a thorough evaluation at different positions can be helpful.

[8] from the manufacturer's website description

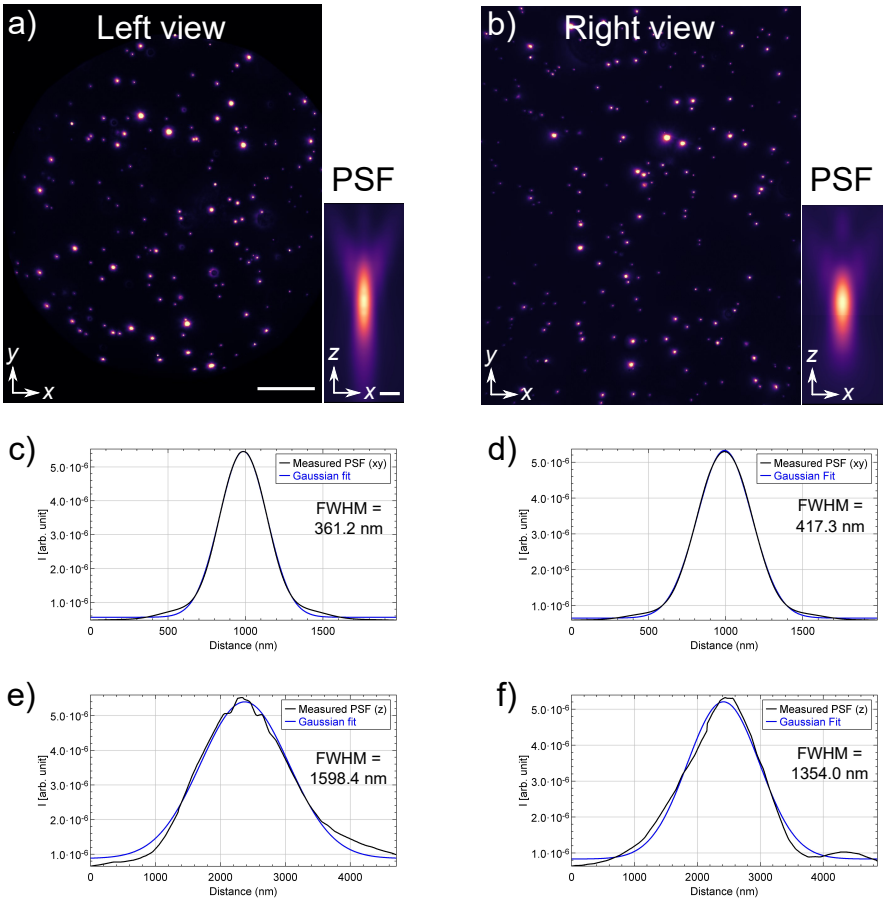

Figure 4.15: PSF measurement with fluorescent beads. PSF measurements under the dual channel detection (left view) and the single channel detection (right view) are presented here. Two maximum intensity projections of the cropped FOV's are presented in a) and b), with the corresponding extracted averaged PSFs from 16 beads on the right hand side. The lateral fit of the PSF with a Gaussian profile results in a $\mathrm{FWHM}_{xy,\,l} = 361.2\,\mathrm{nm}$ for the left view and $\mathrm{FWHM}_{xy,\,r} = 417.3\,\mathrm{nm}$ for the right view. The axial extent of the PSF is characterized via a Gaussian fit as well, and results in $\mathrm{FWHM}_{z,\,l} = 1598.4\,\mathrm{nm}$ for the left view, and $\mathrm{FWHM}_{z,\,r} = 1354.0\,\mathrm{nm}$ for the right view. The z-stepsize was $0.1\,\mu\mathrm{m}$. Scale bar for bead distribution overviews, found in a): $20\,\mu\mathrm{m}$ (applies also for b)), Scale bar of the extracted PSFs, found in a): $0.5\,\mu\mathrm{m}$ (applies also for b)).

4.5.3 Fixed Mouse Embryo Imaging

In addition to the characterization of the illumination profiles and optical performance on fluorescent bead samples, the assessment of the imaging capabilities of biological samples is a priority. I therefore chose to record fixed mouse embryos in the 16 cell stage, immunofluorescently stained with Alexa Fluor 488 against anti-Lamin B, which localizes predominantly at the nuclear lamina. Here, I received help from Dr. Isabell Schneider, who kindly provided me with the mouse embryos and helped with the sample mount preparation.

For best optical quality and highest quantum efficiency, I performed the recordings in the single channel configuration where the cameras and filter wheels are positioned directly after the respective detection objective (*cf.* Ch. 4.2). The mounting was performed with our custom sample mount, based on a thin U-shaped FEP foil as described earlier (*cf.* Ch. 4.1). The imaging results are summarized in Fig. 4.16. The nuclear envelope of the mouse embryo is clearly resolved and allows for nuclear identification by eye. Substructures inside the nuclei, most likely folds or protrusions of the nuclear envelope, can be observed in the central regions.

Of particular interest is the performance of the tandem detection from two sides. The 3D volume was obtained by moving the z-stages from the left objective towards the right objective with a step size of 0.5 μm. This means, that the right detection arm begins to record the surface of the mouse embryo closest to the right detection objective. As the light has to travel through the least amount of biological tissue here, the imaging contrast and resolution are highest at the beginning of the 3D volume, as detected by the right hand detection arm. The opposite holds true for the left detection arm, where the surface closest to the left detection objective is recorded towards the end of the 3D volume. Ergo, the image quality and contrast improve throughout the stack until the best quality and resolution are reached in the final segment of the embryo.

With these two simultaneously acquired 3D stacks at hand, a combined 3D volume, exhibiting better image quality and resolution throughout the entirety of the recorded volume can be achieved via multi-view fusion. This approach has been successfully implemented numerous times on other types of microscopes as well as samples [26][27][55][73], and is supported by our customized software provided by Luxendo, Bruker Corp.

The recorded 3D volumes clearly display the advantage of the dual detection approach as the two views compliment each other. Especially, at greater imaging depths, *e.g.* $> 50\,\mu$m, the contrast and intensity of the opposing view becomes higher, therefore ensuring a more homogeneous and quantitative sampling.

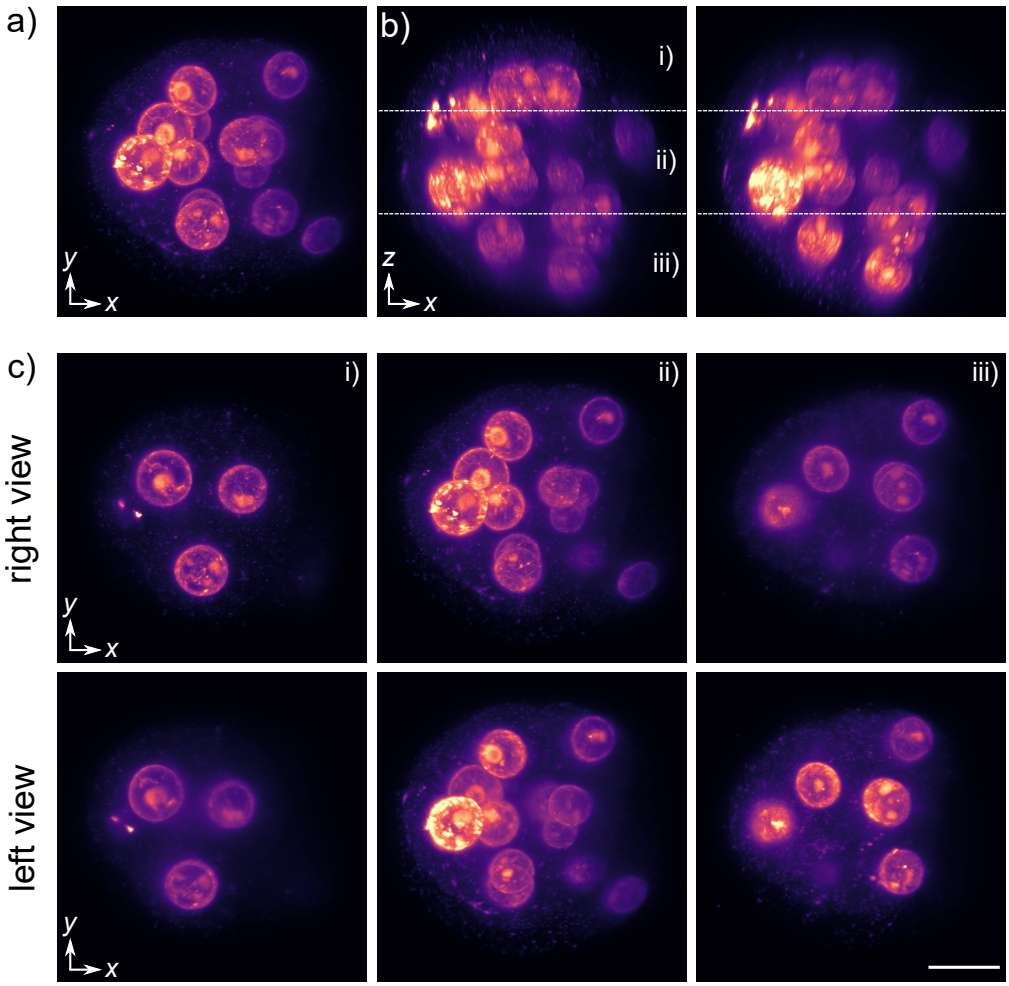

Figure 4.16: InPuLS-SPIM: Recorded stained mouse embryo. A fixed mouse embryo was recorded with a pushed light-sheet on the InPuLS-SPIM and the two resulting datasets are summarized here. A maximum intensity projection of the right view is shown in a). Two maximum intensity projections of the resliced dataset, providing a view on the *xz*-plane, is presented in b). Three regions of 30 μm thickness are marked and correspond to the beginning i), the centre ii) and the end of the recorded stack. As the imaging depth increases for the right detection side, the intensity and image quality decreases, while on the left detection side the opposite is the case. Maximum intensity projections of the three regions from the two different views showcase the quality difference in c). Magnification: 60. *z*-step size: 0.5 μm. Tag lens amplitude: 40 % at $\sim$ 190 kHz resonant frequency. Confocal line thickness: 50 px. Scale bar: 20 μm.

4.6 Materials and Methods

Microscope Design

The microscope was fully designed in the computer-aided design (CAD) software SolidWorks (Dassault Systèmes SolidWorks Corporation). For optical performance and requirement estimations, I also simulated the optical paths with OpticStudio (Zemax LLC, a ray tracing software for the design of optical systems.

Data Processing

All recorded data was pre-processed (cropping, stitching, reslicing, etc.) and visualized in FIJI [108]. Light-sheet and PSF simulations (based on Gibson-Lanni model implemented by [129]) were performed with self-written code in PYTHON (Python Software Foundation). There I used functions and packages from numpy [109] and SciPy [110].

The code was executed on a workstation running Windows 10 Pro, equipped with:

- 2 processors: Intel(R) Xeon(R) CPU E5-2620 v4 @ 2.10 GHz
- Memory (RAM): 192 GB
- GPU: GeForce GTX TITAN X (NVIDIA Corporation)

Materials

- Gelrite / Gelzan CM (Sigma-Aldrich # G1910)
- Fluorescent beads of 0.1 μm size (FluoSpheres Carboxylate-Modified Microspheres, red fluorescent (580/605), 2% solids, Thermo Fisher Scientific Inc., # F8801)
- Two component silicone glue (picodent twinsil)
- Methylene blue (Sigma-Aldrich Chemie GmbH, CAS Number: 122965-43-9)
- 25 μm thick fluorinated ethylene propylene foil (FEP) for sample mount assembly (Lohmann, RD-FEP100A-610)
- Glass capillaries for bead measurement (Drummond Scientific Company, # 9-000-1061):
- PBS
- Lasers: 488 nm & 594 nm (Omicron-Laserage Laserprodukte GmbH)
- Fluorescent filters: 488 nm LP EdgeBasic, 594 nm LP EdgeBasic (both Semrock, IDEX Health & Science, LLC

- Cameras: pco.panda 4.2 bi, PCO AG
- precision stages, filter wheels, electronic control board, microscope software (Luxendo, Bruker Corporation)

4.7 Concluding Remarks

In this chapter, I have introduced the concept of a novel high-throughput fluorescence light-sheet microscope based on a flexible dual-detection approach for multi-scale imaging and supported this work with simulation and experimental data. For optimal results across the different spatial scales, we chose to implement an alternative illumination approach designed around extended or so-called *pushed* light-sheets which can be generated with resonantly driven liquid lenses, such as the here presented TAG lens. I have shown that in the ideal theoretical model, resolution gains in the axial domain are possible with the use of pushed beams. The experimental conditions did not reach the theoretical predictions for several possible reasons, such as the non-linear excitation profile of the TAG lens, optical aberrations in the illumination path, and the indirect measurement of the illumination profile based on fluorescence excitation of methylene blue. Nonetheless, the TAG lens allows for quick and uncomplicated changes of the light-sheet length which can be of benefit when recording samples of different sizes or when focussing on a smaller region of interest. The regular Gaussian light-sheet is always available as a standard illumination option to fall back on, if desired, as both illumination schemes have their benefits.

Further, the optical layout and mechanical design of the three main units were presented here, and the different modes of operation were explained, *e.g.* sequential vs. simultaneous channel detection. The novel sample mount including its assembly has been introduced. A final picture of the assembled microscope can be found in Fig. 4.17.

Finally, the performance of the entire microscope has been evaluated on samples including fluorescent microspheres and on an immunofluorescently labelled mouse embryo. Here, the advantages of the dual-detection could be clearly demonstrated.

The next steps before the microscope will be able to record extended movies of developing mammalian embryos, is the addition of a incubation system. It is essential for the proper development and any mammalian sample.

Further, an update to the TAG lens illumination scheme is already planned and will allow laser modulation in synchrony to the focal position of the TAG lens. This approach has been demonstrated successfully by Power *et al.* [126] and will improve the axial confinement of the

illumination beam, and decrease the effective exposure time with out of focus light on the sample. A more thorough investigation of the effective profile would be beneficial as the indirect measurement with the help of a fluorescent medium shows its limitations at small beam widths. A possible approach has been demonstrated by Dean *et al.* [122] in which the authors used a collinear detection arm to sample the illumination arm stepwise in the propagation direction. Alternatively, a special mirror, attached to a custom sample holder could be positioned at the focus of the illumination and detection objective at 45°. The beam can then be sampled by movement of the detection objective or illumination objective. Either way, the movement has to be precise as the the beam extent ranges between 20 and 200 μm. With the incubation system operational in the near future, and possible illumination profile improvements, I expect this microscope to become a useful tool for the in-house mammalian research. Not only is it an additional system in the SPIM family at the EMBL, but it offers unique experimental flexibility on the illumination and detection sides and produces data of superior imaging quality in comparison to its single detection objective based relatives, such as the InVi-SPIM.

Figure 4.17: InPuLS-SPIM: Completed microscope setup. A wideangle picture of the full optical table ($150 \times 110\,\mathrm{cm}^2$) with the assembled microscope is displayed here. For illustration purposes, I configured the left detection unit for simultaneous dual-colour detection (*cf.* Ch. 4.2), while the right arm is seen in its sequential channel detection configuration.

5 Conclusion and Outlook

In this work, I have presented two independent approaches which nevertheless share one common theme: the strive for improved image contrast and resolution across the recorded 3D volumes of the sample of interest.

The aim of the first project was to investigate possible image quality improvements upon refractive index adjustments on live sample in light-sheet microscopy. For this study, I chose a representative set of widely used model organisms in developmental biology to examine possible changes in contrast upon refractive index change of the surrounding mounting medium. Additionally, I performed simulations on the illumination and detection light for small volumes, and expanded those predictions via experiments on phantom samples containing fluorescent beads. The results paint a clear picture: aberrations arising from the sample-to-medium interface play a crucial role towards the final recorded image quality. Increasing the mounting medium's refractive index to the refractive index range of the sample, restores image quality across the 3D volume. The magnitude of contrast improvement depends on the sample's optical properties. For example, inhomogeneous refractive index distribution, absorbing tissue parts, scattering structures, autofluorescent proteins, and the sample size itself are all factors to consider. Here, I presented samples of different properties, discussed suitable mounting strategies for short-term refractive index matching experiments and for potentially long-term *in vivo* recordings under adjusted mounting medium.

The second project's goal was to design a novel high-throughput light-sheet microscope for mammalian samples, which combines the most prominent advantages of two available in-house light-sheet systems: the MuVi-SPIM [55] and the InVi-SPIM [60]. Additionally, to bridge the spatial scales among mammalian samples as single cells, early mouse embryos, or organoids, the InPuLS-SPIM employs a tunable acoustic gradient index lens with which extended or so-called 'pushed' light-sheets of different lengths can be realized. Here, I describe the optical design, the microscope's capability of simultaneous-dual color detection, characterize the generated pushed beams, and discuss possible resolution improvements tied to the thin core of the

extended light-beams. Further, the optical performance is explored with a PSF estimation based on fluorescent beads of size below the diffraction limit. A fixed mouse embryo is recorded with the help of dual sided detection. The clear advantages of the second detection lens are visible and a dataset of overall higher contrast, and of more isotropic signal is the result. In summary, compared to existing high-throughput light-sheet based systems for live mammalian sample imaging, the InPuLS-SPIM offers twice the photon collection efficiency due to its dual-detection scheme, allows to image samples of various sizes from $\sim 20\,\mu$m to $\sim 200\,\mu$m while retaining the high-throughput capability of the first multi-sample light-sheet microscope dedicated to early mammalian sample imaging [60].

In future work, I look forward to seeing the experimental flexibility of the InPuLS-SPIM fully taken advantage of for mammalian and other complex organisms, *e.g.* by combining it with RI matching approaches and adaptive optics to achieve unprecedented resolution in *in toto* and deep-tissue imaging.

With two here presented contributions to the field of light-sheet fluorescence microscopy, and more broadly light based microscopy, I hope to have pushed the door open a few μm further to record life's processes in true *in toto* fashion: with single cell resolution down to the core of the organism and insight into intracellular events.

6 The Author's Publications and Contributions

Over the course of my time at the EMBL, I contributed to the following publications:

Francesca Caroti, Everardo González Avalos, Viola Noeske, Paula González Avalos, Dimitri Kromm, Maike Wosch, Lucas Schütz, Lars Hufnagel, Steffen Lemke, "Decoupling from yolk sac is required for extraembryonic tissue spreading in the scuttle fly Megaselia abdita", *eLife*, vol. 7, p. e34616, Oct 2018. https://doi.org/10.7554/eLife.34616.001

Gustavo de Medeiros, Dimitri Kromm, Balint Balazs, Nils Norlin, Stefan Günther, Emiliano Izquierdo, Paolo Ronchi, Shinya Komoto, Uros Krzic, Yannick Schwab, Francesca Peri, Stefano de Renzis, Maria Leptin, Matteo Rauzi, Lars Hufnagel, "Cell and tissue manipulation with ultrashort infrared laser pulses in light-sheet microscopy." *Scientific reports*, vol. 10(1):1942, Feb 2020. doi:10.1038/s41598-019-54349-x

Additionally, a patent based on the here presented InPuLS-SPIM (*cf.* Ch. 4) has been filed with the European Patent Office under the file number EP 21191351.2, with the following authors: Dimitri Kromm, Jan Ellenberg, Lars Hufnagel.

7 Appendix

7.1 Elliptical Gaussian Beams

When using a cylindrical lens for light-sheet generation instead of a galvanometric scan mirror for a digitally scanned light-sheet, it is feasible to treat the light-sheet as an elliptical Gaussian beam:

$$U(x,y,z) = A_0 \cdot \sqrt{\frac{w_{x,0}}{w_x(z)}}\sqrt{\frac{w_{y,0}}{w_y(z)}} \cdot \exp\left(-\frac{x^2}{w_x^2(z)}\right) \cdot \exp\left(-\frac{y^2}{w_y^2(z)}\right) \cdot \exp\left(-i\phi(x,y,z)\right) \tag{7.1}$$

$$I(x,y,z) = |A_0|^2 \cdot \frac{w_{x,0}}{w_x(z)}\,\frac{w_{y,0}}{w_y(z)} \cdot \exp\left(-\frac{2x^2}{w_x^2(z)}\right) \cdot \exp\left(-\frac{2y^2}{w_y^2(z)}\right) \tag{7.2}$$

The difference to the previously introduced Gaussian beam (*cf.* Eq. 2.22) comes from the now uncoupled x- and y-waists. Both can be treated independently of each other, so that two separate Rayleigh ranges and beam waists can be defined:

$$z_{x,\mathrm{R}} = \frac{n\pi w_{x,0}^2}{\lambda_0} \tag{7.3}$$

$$z_{y,\mathrm{R}} = \frac{n\pi w_{y,0}^2}{\lambda_0} \tag{7.4}$$

with

$$w_x(z) = w_{x,0}\sqrt{1+\left(\frac{z}{z_{x,\mathrm{R}}}\right)^2} \tag{7.5}$$

$$w_y(z) = w_{y,0}\sqrt{1+\left(\frac{z}{z_{y,\mathrm{R}}}\right)^2} \tag{7.6}$$

Typically the height of the FOV (dimension of y-axis) then defines the waist $w_y(z)$ and with it the focal length of the cylindrical lens.

7.2 Image Quality Metric Analysis with BGN-DCT

Image quality or contrast[1] is a broadly used term, often times referring to the signal-to-noise ratios found within an image and the information stored in it. Typically such measures are used to find the best focus with an optical system. They are for example, found in regular consumer cameras and help the user with the 'autofocus'. A variety of metrics exist, ranging from intensity-based definitions to spectral ones, where the image is transformed into its frequency space first. With varying image properties, the performance of individual metrics typically changes as well. Therefore, the application usually defines the metric that is being used. A helpful summary and comparison of a great number of metrics, applied to light-sheet microscopy images, has been done by ([66], SI). The authors of the mentioned work found that for their light-sheet microscopy data, spectral metrics performed the best, with minor differences in precision and performance among them. Other publications falling back onto the spectral analysis for light-sheet data include Truong *et al.* [76] and Preusser *et al.* [77]. Beyond light-sheet microscopy, similar approaches have been established in the past and reviewed for different data [132]. An extended review in the field of image quality assessment is provided by Damon M. Chandler [133].

As discussed in Ch. 3, the goal is to find areas of the 3D volume that are of higher contrast and contain more information than other areas. Of importance in this task, is the direct comparison between images of one 3D dataset, *e.g.* slices at the beginning of the stack and at the end. Further, a comparison within one image is beneficial, as the image content and quality varies spatially in the image. I therefore chose to apply a spectral metric based on the discrete cosine transform to evaluate the acquired datasets. To make the metric comparable for different images, I included a normalization step, in which the metric can be normalized against an image of choice. Throughout this work, I always used the cameras background image, where no or insignificantly little light reaches the camera sensor[2]. Any fluorescent signal detected by the camera, will then give a metric value, higher than that of the background.

The algorithm to find the image quality metric of an image follows the following steps (IM: image, BG: background image, *DCT*: discrete cosine transform (operation), SP: DCT spectrum of image, SPBG: spectrum of background image, MA: spectral mask to remove high frequencies

[1] in this work used interchangeably

[2] If a large enough stack is recorded, where in the first slices the sample is not yet excited by the light-sheet, the first image(s) can serve as a reference background.

below the resolution limit - uses support radius $r_p = \delta_{xy}^{-1} = \frac{NA}{0.61*\lambda_0}$, similar as in [66], BGN-DCT-M: background normalized discrete cosine transform metric, the final number used to describe the found image content/frequencies.)

1. IM = IM - $\overline{\text{IM}}$
2. SP = DCT(IM)
3. BG = BG - $\overline{\text{BG}}$
4. SPBG = DCT(BG)
5. SP = SP $\cdot$ MA
6. SPBG = SPBG $\cdot$ MA
7. BGN-DCT-M = $\left|1 - \sum \sqrt{\frac{SP}{SPBG}}\right|$

With this metric measure at hand, I performed two types of analysis on the recorded 3D data:

- Full stack analysis: Here, I computed a metric for each recorded plane (image) and compared the metric curves throughout the stack with curves of stacks recorded under different refractive indices.
- Tiled image analysis: In this case, I divided a given image into tiles of few pixels in size, *e.g.* tiles of 16 by 16 pixels. The metric calculation was then normalized with a background value extracted from a representative background tile of the same size. As a result, tiles with frequencies in the range of the background, score low metric numbers, while tiles that carry a larger number of frequencies, score higher metric numbers. The final result is a tiled image with different metric scores assigned to the respective tiles. Areas of with more frequencies, *e.g.* more content at higher resolution, score higher values than areas of with less content or content of lower frequencies.

In all metric calculations a low pass filter based on the detection objectives theoretical resolution is applied first. Any frequency higher than the resolution limit is therefore treated as noise and does not contribute to the metric score. However, scattered light and autofluorescence can affect the metric as they can generate signal of higher and medium frequency, reducing the signal-to-noise level in an image but also overlapping with the frequencies of the desired signal. Reducing

the support radius and filtering out more high frequencies can counteract such trends. I have chosen not to do this arbitrarily throughout this work, as I wanted a consistent basis throughout the analysis of different data. In Ch. 3, it becomes evident, that the metric can identify regions of higher (quality) content throughout different datasets with changing signal types. It best predicts quality differences in the *Arabidopsis* root and the *Mus musculus* which match observations by eye and intensity profile measurements. It also

7.3 RI Matching of *Mus musculus* in direct contact with OptiPrep

As mentioned in the main text, we also assessed possible image quality improvements in post-implantation mouse embryos for a direct contact of OptiPrep solutions of different concentrations with the embryo. Such an example can be seen in Fig. 7.1. A clear improvement in contrast is visible, almost over the entire embryo. However, the positive imaging quality results should be interpreted with caution: Our imaging conditions were not providing the necessary incubation for long-term survival of mammalian specimens in our sample chamber. Further, we found that OptiPrep has lethal effects on the mouse embryo at concentrations as low as 15 %, and leads to severe misdevelopments at 10 %. Between recordings of different refractive indices, lies a time window of approx. 10 to 15 min. During this time frame a clear shrinking of the embryo's volume can be observed.

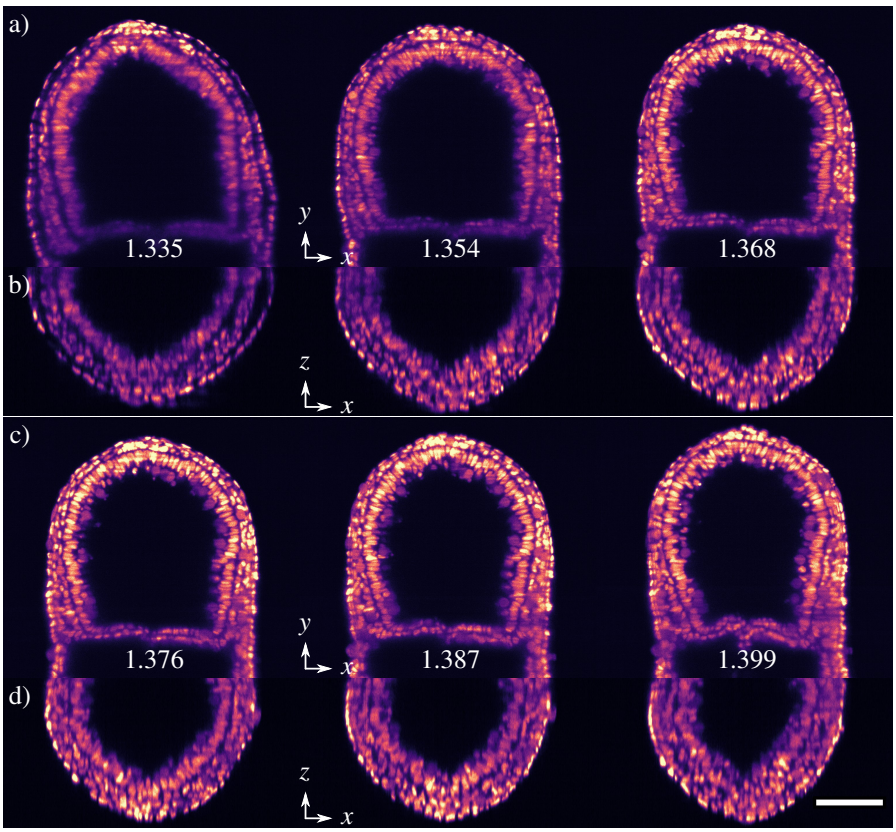

Figure 7.1: Refractive Index Matching of *Mus musculus* Post-Implantation Embryo. Adapting the refractive index of the immersion medium to that of the mouse embryo results in clearly visible image quality improvements across the embryo. We recorded an E7.5 mouse embryo expressing IRFP in the nucleus. It was mounted as described in the main text (*cf.* Ch. 3.7). Example slices near the center of the embryo (~ 200 μm depth of the 3D recordings under different refractive indices are shown in a) and c). The corresponding cross-sectional views (xz-plane) are displayed in b) and d). We used dual sided illumination with a laser of 685 nm wavelength. The light-sheets had a length of ~ 200 μm for these experiments. We additionally used the confocal line scanning mode of the cameras with a 40 px readout width. The z-step size was 2.0 μm. Scale bar: 100 μm. Data produced jointly with Dr. Henning Falk.

7.4 Toxicity Assessment on *Arabidopsis* Seedlings

While OptiProp has been reported to be non-toxic and compatible for different developing specimens [25], we decided to assess whether it has possible effects on the development of our samples. For the assessment of the *Arabidopsis* seedlings, Marion Louveaux kindly performed the experiments. We chose three conditions in which the plants were let to grow for approx. 3 days. We designed specific mounts which can fit a beaker and hold mounted seedlings in the medium, similar to the mounting conditions of our MuVi-SPIM setup. Otherwise standard

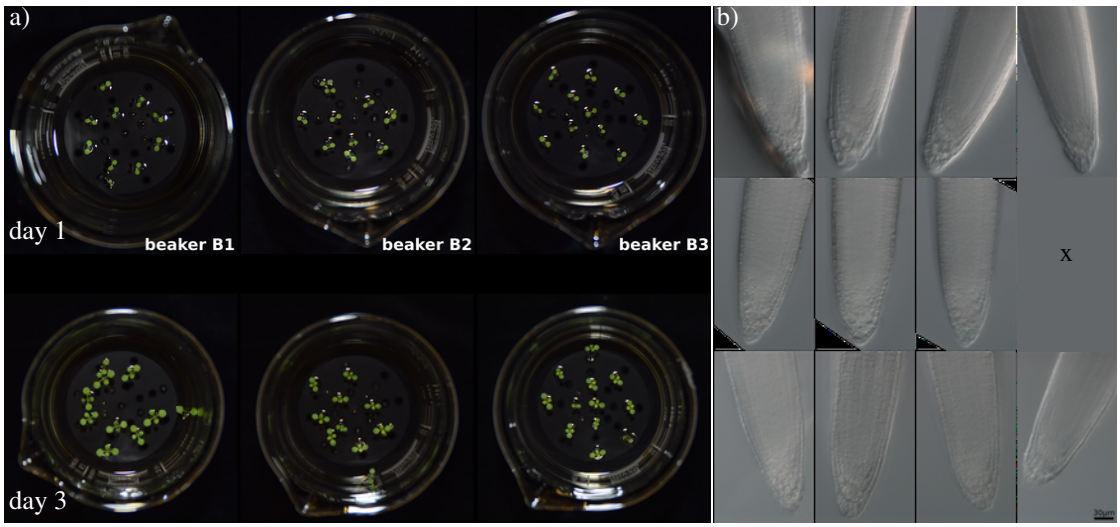

Figure 7.2: Toxicity assessment of *Arabidopsis thaliana* seedlings. *Arabidopsis thaliana* seedlings tolerated OptiPrep and developed only slightly slower than under control conditions. The two pictures in a) show the seedlings from the top before the beginning of the experiment (day 1) and after (day 3 for the three conditions (beaker 1: control, beaker 2: 25 % OptiPrep), beaker 3: 50 % OptiPrep)). The picutures in b) show the root tips under a differential interference contrast microscope. [Images kindly provided by Marion Louveaux.]

conditions for growing the plants were used.

- control, no OptiPrep: 0.086 g MS, 4 ml MES, 36 ml water
- 25 % OptiPrep: 0.086 g MS, 4 ml MES, 26 ml water, 10 ml OptiPrep
- 50 % OptiPrep: 0.086 g MS, 4 ml MES, 16 ml water, 20 ml OptiPrep

The seedlings showed near normal growth over the course of three days. Pictures of the root tips with a differential interference contrast microscope did not show any negative effects on the plant's development under OptiPrep addition to the media of up to 50 %. See Fig. 7.2 for images of the seedlings under the different growth conditions.

7.5 Toxicity Assessment on *Oryzias latipes*

The assessment of toxicity under exposure to OptiPrep of Medaka larvae was kindly performed by Colin Lischik. For these experiments the fish were dechorionated with hatching enzyme at stage 30 and subjected to different concentrations of OptiPrep. Dead and swimming larva were

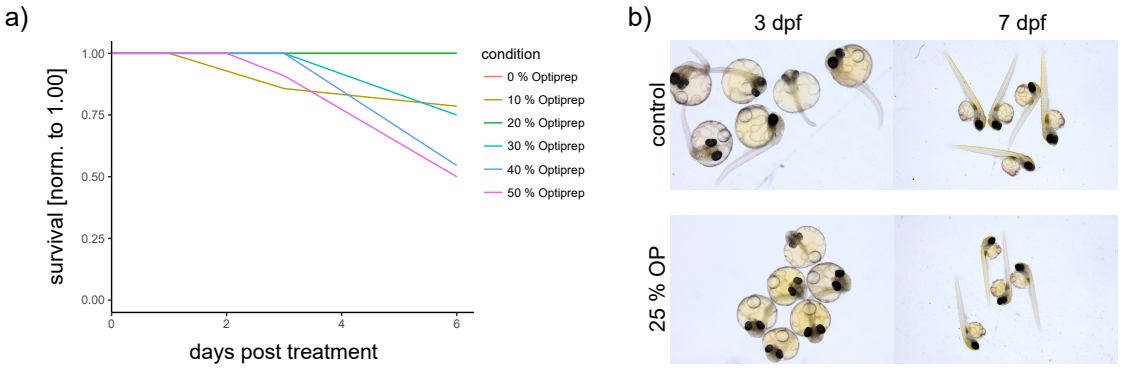

Figure 7.3: Toxicity assessment of *Oryzias latipes* larvae. Medaka larvae from 3 dpf tolerated OptiPrep up to a period of two days and up to a percentage of 50 % without lethal effects. Prolonged exposure to OptiPrep on the other hand affected development and lead to lethal effects in correlation with the percentage of OptiPrep in the media. This is illustrated in the graph in a). The four images in b) show larvae in the control group (upper row) and in the group that was exposed to an OptiPrep concentration of 25 % (lower row). Please note that the images in b) are from a separate experiment. No images were acquired from the experiment shown in a). [Graph and images kindly provided by Colin Lischik.]

noted. The data is presented in the graph in Fig. 7.3 a). Longer exposures to OptiPrep has an unmistakable negative effect on the Medaka's development and can lead to lethal effects. Shorter exposures to percentages up to 50 % however, are tolerated by the larvae, as well as lower concentrations over longer periods of time, e.g. 25 % over a period of 3-4 days. In terms of refractive indices, this corresponds to $n_{50\,\%\,\mathrm{OP}} \approx 1.37$ and $n_{25\,\%\,\mathrm{OP}} \approx 1.35$.

7.6 Effects on System's PSF for Beams of Different Lengths

In chapter 4.3.2 I showed simulations for a beam length of 50 μm. Here, I want to present the same simulations performed for beams of 100 μm and 20 μm length respectively. The results are overall similar between the length scales. Interestingly, at 20 μm beam length, the system's PSF is also positively affected by the regular Gaussian beam.

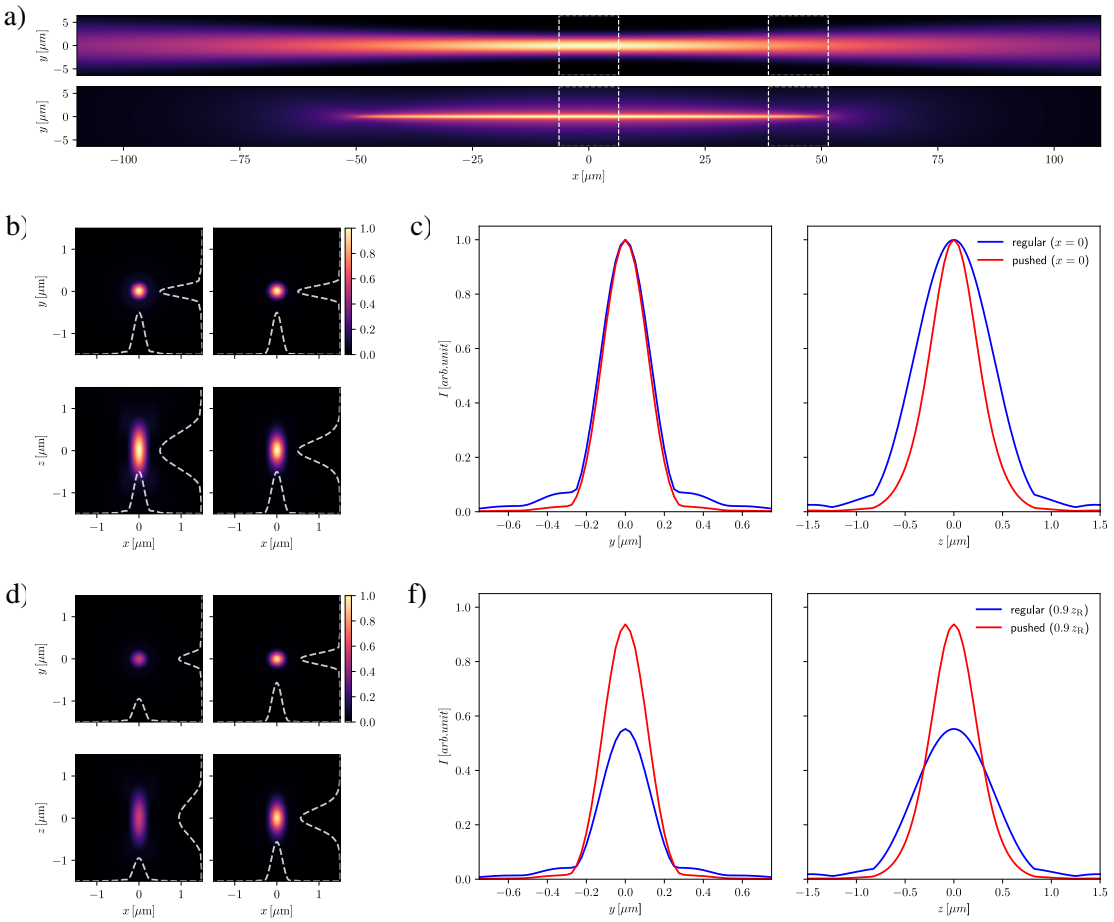

Figure 7.4: Regular Gaussian beam vs. pushed beam of $100\,\mu$m **length - effects on system's PSF.** Both simulated beams of $100\,\mu$m length are shown as sums along the z-axis in a). The dotted lines in the regular Gaussian beam (upper image) and the pushed beam (lower image) indicate the volume used for the downstream PSF simulations. The central region is located exactly at $x = 0$ while the second region is located around the Rayleigh length $x = 0.9z_R = 45\,\mu$m. The system's effective PSF at the center of the respective region is calculated via a multiplication of the light-sheet and detection PSF volumes as done in Fig. 4.9. Maximum intensity projections of the effective PSF for the center of the illumination beam is shown in b). The z-extent of the detection PSF is reduced from $\mathrm{FWHM}_{\mathrm{RegLS}} = 0.9\,\mu$m to $\mathrm{FWHM}_{\mathrm{PuLS}} = 0.6\,\mu$m. The cross-sectional intensity profiles are plotted in c). Maximum intensity projections of the PSF at $x = 0.9z_R = 45\,\mu$m are displayed in d). The Gaussian beam's intensity drop-off results in a clear reduction of the PSF's intensity. The pushed beam's intensity reduced by $\sim 10\,\%$ and the axial extent of effective PSF remains $\mathrm{FWHM}_{\mathrm{PuLS}} \approx 0.6\,\mu$m. All intensities were normalized to 1.0 arb unit at the center of the beam profiles. The PSF simulation volume was $[x, y, z] = 513 \times 513 \times 513$ voxel with a voxel size of $25\,\mathrm{nm}^3$.

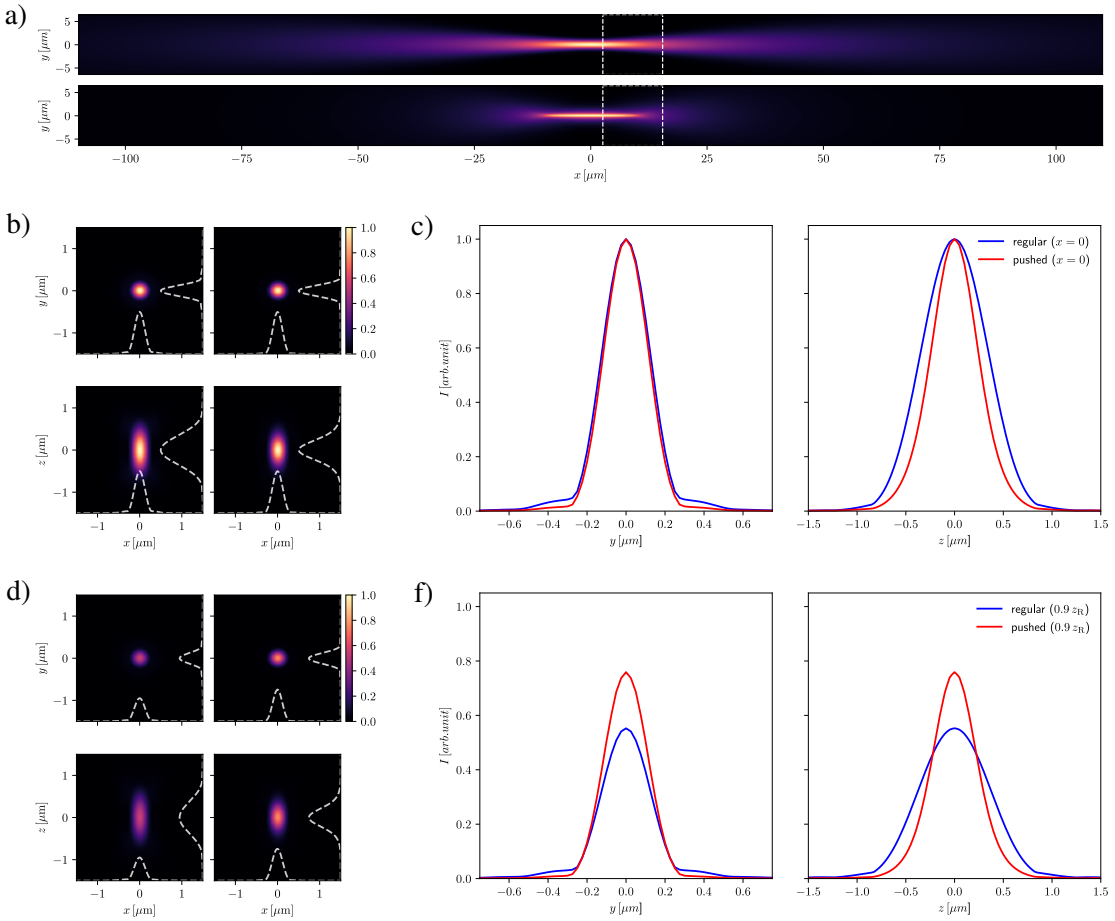

Figure 7.5: Regular Gaussian beam vs. pushed beam of $20\,\mu$m **length - effects on system's PSF.** Both simulated beams of $20\,\mu$m length are shown as sums along the z-axis in a). The dotted lines in the regular Gaussian beam (upper image) and the pushed beam (lower image) indicate the volume used for the downstream PSF simulations. The central region is located exactly at $x = 0$ (not marked) while the second region is located around the Rayleigh length $x = 0.9z_R = 9\,\mu$m. The system's effective PSF at the center of the respective region is calculated via a multiplication of the light-sheet and detection PSF volumes as done in Fig. 4.9. Maximum intensity projections of the effective PSF for the center of the illumination beam is shown in b). The z-extent of the detection PSF is reduced from $\mathrm{FWHM}_{\mathrm{RegLS}} = 0.8\,\mu$m to $\mathrm{FWHM}_{\mathrm{PuLS}} \approx 0.5\,\mu$m. The cross-sectional intensity profiles are plotted in c). Maximum intensity projections of the PSF at $x = 0.9z_R = 9\,\mu$m are displayed in d). The Gaussian beam's intensity drop-off results in a clear reduction of the PSF's intensity. The pushed beam's intensity reduced by $\sim 20\,\%$ and the axial extent of effective PSF remains $\mathrm{FWHM}_{\mathrm{PuLS}} \approx 0.5\,\mu$m. All intensities were normalized to 1.0 arb unit at the center of the beam profiles. The PSF simulation volume was $[x, y, z] = 513 \times 513 \times 513$ voxel with a voxel size of $25\,\mathrm{nm}^3$.

8 Acknowledgements

During my time in Heidelberg and at the EMBL, I have been lucky enough to interact with a great number of outstanding scientists which in one way or another all helped shape this PhD. After one year of living under the transformations of our everyday life under the pandemic, the day to day interactions that make EMBL such a unique environment and which have contributed to my understanding of what science is, are dearly missed. And through this current situation it becomes easier to point the finger onto exactly those moments that we otherwise might take for granted. The many Friday evening 'beer sessions', in person seminars, conferences, symposia, parties, retreats, coffees, and hallway chats all helped me to stay up to date with the science around me, form collaborations or simply exchange advice. At this point I truly wish that EMBL's social spirit will be revived soon, as I firmly believe that a functioning social environment greatly contributes to the quality of science.

During my scientific journey in Heidelberg, I had the luxury to work under and with not one, but three great mentors whom I would like to express my gratitude here. In chronological order:

Jochen Wittbrodt, I thank you deeply for introducing me to light-sheet microscopy, for personally putting me on the right track, inciting the love for science and its community with your own passion and example. It has been my greatest pleasure working with you and I consider myself very fortunate for having crossed your path at the right time.

Lars Hufnagel, thank you for giving me the opportunity to work in your group, for trusting me from the very beginning with important tasks, expensive material and ongoing collaborations, but also for always letting me establish my own collaborations. I am especially grateful for the numerous discussions on optics, microscope design, and biology. Thank you for being so open with your thoughts on projects and trends. I learned a great deal from you.

Jan Ellenberg, thank you for taking me under your wings at the beginning of the pandemic, for letting me be part of your lab and trusting me with the conception, design and construction of the InPuLS-SPIM. Without your support my PhD would not have been able to shape up the way it

did, and there would be one microscope less at the EMBL. I cherish the fruitful discussions with you and your group members. Not only did I learn a lot about mammalian cells and embryos, but also about how a comparatively large group as yours can function so well.

Beyond my direct supervision from the three gentlemen mentioned above, I was lucky enough to have regular interactions and collaborations with an inspirational group of PIs, among which I especially am grateful to:

Robert Prevedel, thank you for being part of my TAC, for always being there to discuss optics and other matters, for supporting me throughout the tougher period during my PhD, for letting me feel like a welcome guest in your group and for being a great role model.

Alexander Aulehla, thank you for completing my TAC, for always assessing my work and results critically, for supporting me with advise and action, and for being an active and great collaborator.

Steffen Lemke, I particularly enjoyed our collaboration on imaging *Megaselia abdita*, discovering new biology during that project and publishing it. Thank you for the support, the guidance, and excitement you maintained for me throughout the years. The Durian experiment shall not be discussed further here.

Maria Leptin, it has been a pleasure working together with you and your group. Your unique approach and energy are a true inspiration and I am grateful for having been able to contribute to some of the projects in your group as well as having received feedback on my own work.

Alexis Maizel, thank you for making it possible to expand my sample repertoire beyond insects, fish, and mammals to *Arabidopsis*. It has been a fun experience to work with you and your group, but also to see you regularly at the Heidelbergman.

Takashi Hiiragi, thank you for your support and trust throughout the last years. I am grateful for having been able to work with you and your group on the frontiers of mammalian imaging. I am very much looking forward to continue our collaboration in the Netherlands.

Nathalie Daigle, thank you for helping me transition to Jan's group, for always being there and for supporting me throughout all this time. The last two years would have been much harder without your presence and help.

Gustavo Glasner de Medeiros, thank you for teaching me the ways of SPIM, for inciting me with your passion for *Drosophila* and its rear parts, for showing me how collaborations can be built and maintained and for remaining a great friend and colleague past your departure from the institute. I cherish the fun moments and laughs during working hours and after. My experience at the EMBL would have been a very different one without you and I hope our paths will cross

again in the future.

Bálint Balázs, thank you for always being available to discuss ideas, help me on a programming or control challenge, or simply update the microscope software to my wishes. I am also thankful for having found a friend in you, who has made life at the EMBL more interesting, who made some conference visits extremely memorable and who always gladly joined for biking and swimming workouts.

Rajwinder Singh, it was a pleasure holding the fort in the end of the Hufnagel era with you. I cherish our times in the microscope room, discussing optics, our setups, or simply life. You made the last months more pleasant and I am happy to have gained you as a friend and colleague. Thank you for all your support throughout my PhD time. I hereby pass on the 'Hufnagel-torch' to you and hope it will light your path in the last months of your PhD.

Nils Norlin, I welcomed sharing office space with you throughout these years, discussing optics, experiments, and future directions. But also the many chats about cultural specifics, food, random knowledge, and Star Wars will remain a strong memory. I'm looking forward to collaborate in the future and stop by in Lund.

Ulla Maj-Fiuza, as a physicist I am particularly grateful for having shared office and lab space with you over the last few years. You taught me a number of good tricks and methods and always asked interesting questions about optics, some of which deepened my knowledge, too. Thank you for the good times and the many interesting discussion regarding work, science, politics, and culture.

Marvin Albert, Nils Wagner, Tatjana Schneidt, thank you for always keeping up the good vibe in and outside our group, as well as for always being there when needed. I hope our paths will cross again in the future.

Colin Lischik and Leonie Adelmann, thank you for helping me out with the refractive index matching experiments involving *Medaka* larvae. It has been lots of fun working alongside you, as well as exchanging ideas and laughs.

Henning Falk and Takehito Tomita, I thank you both for exploring refractive index matching in live mouse embryos with me, for being patient in explaining the biology and culturing methods, for performing various survival experiments and for always being responsive when needed.

Marion Louveaux, thank you for providing me with samples whenever needed, for thoroughly discussing and performing the survival experiments on *Arabidopsis* embryos and for being so patient in explaining plant biology to me. I enjoyed our collaboration greatly.

Silvija Svambaryte, muchas gracias por todo el tiempo conmigo. I truly enjoyed our *de novo*

mounting methods on *Medaka* embryos and am happy we were able to record a number of amazing time lapses. Thank you for teaching me about C.B. while remaining open to rock and metal during our imaging sessions.

Vladyslav Bondarenko, thank you for convincing me to implement a de novo mounting scheme for mouse peri-implantation imaging on our MuVi-SPIM with you. Despite the pandemic this turned out to be a incredibly fruitful collaboration of which I was gladly part of. I am happy that our collaboration transitioned to a friendship in these last months. The various political and philosophical discussions during and beyond our imaging sessions were a refreshing change to the scientific chatter. I am looking forward to see our work published and continue our collaboration beyond the borders of Germany.

Lucas Schütz, thank you for being an exceptional colleague and friend. I particularly enjoyed our furrow adventures with their imaging sessions, trying to unravel the mysteries of the cephalic furrow. The many dinners, coffees and photography chats are all memories I hold dear and hope to expand upon in the future.

Sourabh Bhide, Daniel Rios, Juan Elif, Benedikt Best, André Schwarz, Bernhard Hampoelz, I thank you all for making me part of the fly community at EMBL, for explaining various parts of the *Drosophila* development, for letting me record some of the most fascinating movies and images during my time at EMBL, and most importantly for making me have a great time at the institute. I will miss our interactions and collaborations.

Joran Deschamps, Rory Power, Yu Lin, Ling Wang, Lina Streich, Carlo Bevilacqua, Marco Lampe, Stefan Terjung, thank you all for the good times and chats around EMBL throughout the years. As my optics support team outside our lab, I am grateful for all the exchange we had around microscopy and hope to remain in touch with you.

Isabell Schneider, Marina Makharova, and Franziska Kundel, thank you for your help with mouse embryo imaging and for your patience with me when it came to the mouse biology.

I also want to give the meachanical workshop at the EMBL a big thank you. The realization of the InPuLS-SPIM would not have been possible without the help of the following gentlemen: Leo Burger, Tim Hettinger, Arthur Milberger, Henry Werner, Christian Handlos, Helmuth Schaar, and Benjamin Straub

A big thank you also goes out to the electronic workshop who has supported my work throughout my time at the EMBL. Thank you Vera Stankova, Alejandro Gil Ortiz, and Christian Kieser!

Elisabeth Kugler, thank you for your professional manuscript reading and feedback on the early drafts, as well as moral support.

Next to the strong scientific support, the support outside of the lab was also crucial for the completion of this work. Especially, some of my closest friends have been upholding my spirit.

A big pillar of support was always given by the famous GW27 community: Marta F., thank you for all the moral support, the many laughs, the creative science discussions, and teaching me the Mediterranean mindset as a special type of problem solver. Marc S., Michael S., Jenny H., Teona G., Lisa H., and Lukas H., thank you for making life in Heidelberg and in GW27 more fun and pleasant. I cherish the numerous memories with you and hope to create new ones, no matter where. The moral support throughout my PhD time was most welcome.

Franz K., Lennart A., Everardo G., Allyson R., and Savannah J., I am happy to have found such great friends in you over the past decade. Not only were you always there for me, made life in Heidelberg more colourful, but as great scientists yourself, gave me a great opportunity to discuss ideas and receive valuable feedback. I'm looking forward to the chapter beyond Heidelberg.

Marta G.M., I thank you deeply for all your support and patience throughout these years with me. Thank you for never doubting me, for encouraging me, for always being available for science talk, but also for distracting me from it at the right times.

And finally, I want to thank my family for their love, support, advice, belief and encouragement throughout my time at the EMBL.

9 Bibliography

[1] R. Hooke, J. Allestry, and J. Martyn, *Micrographia, or, Some physiological descriptions of minute bodies made by magnifying glasses: with observations and inquiries thereupon*. London: Printed by Jo. Martyn and Ja. Allestry, printers to the Royal Society, 1665. https://www.biodiversitylibrary.org/bibliography/904.

[2] J. James, "Van Leeuwenhoek's discoveries of 1677–1678: A look too far," *Micron*, vol. 25, no. 1, pp. 1–4, 1994.

[3] E. Abbe, "Beiträge zur Theorie des Mikroskops und der mikroskopischen Wahrnehmung," *Archiv für Mikroskopische Anatomie*, vol. 9, pp. 413–418, Dec. 1873.

[4] J. Smiles, "Ultraviolet Microscopy," *Journal of Applied Bacteriology*, vol. 21, no. 1, pp. 137–142, 1958.

[5] P. Kirkpatrick and A. V. Baez, "Formation of Optical Images by X-Rays," *J. Opt. Soc. Am.*, vol. 38, pp. 766–774, Sep 1948.

[6] M. Knoll and E. Ruska, "Das Elektronenmikroskop," *Zeitschrift für Physik*, vol. 78, pp. 318–339, May 1932.

[7] T. H. Maiman, "Stimulated Optical Radiation in Ruby," *Nature*, vol. 187, pp. 493–494, Aug 1960.

[8] O. Shimomura, F. H. Johnson, and Y. Saiga, "Extraction, Purification and Properties of Aequorin, a Bioluminescent Protein from the Luminous Hydromedusan, Aequorea," *Journal of Cellular and Comparative Physiology*, vol. 59, no. 3, pp. 223–239, 1962.

[9] E. Deltcheva, K. Chylinski, C. M. Sharma, K. Gonzales, Y. Chao, Z. A. Pirzada, M. R. Eckert, J. Vogel, and E. Charpentier, "Crispr rna maturation by trans-encoded small rna and host factor rnase iii," *Nature*, vol. 471, p. 602—607, March 2011.

[10] M. Jinek, K. Chylinski, I. Fonfara, M. Hauer, J. A. Doudna, and E. Charpentier, "A programmable dual-rna-guided dna endonuclease in adaptive bacterial immunity," *Science*, vol. 337, no. 6096, pp. 816–821, 2012.

[11] M. Minsky, "Memoir on inventing the confocal scanning microscope," *Scanning*, vol. 10, no. 4, pp. 128–138, 1988.

[12] S. W. Hell and J. Wichmann, "Breaking the diffraction resolution limit by stimulated emission: stimulated-emission-depletion fluorescence microscopy," *Opt. Lett.*, vol. 19, pp. 780–782, Jun 1994.

[13] E. Betzig, G. H. Patterson, R. Sougrat, O. W. Lindwasser, S. Olenych, J. S. Bonifacino, M. W. Davidson, J. Lippincott-Schwartz, and H. F. Hess, "Imaging intracellular fluorescent proteins at nanometer resolution," *Science*, vol. 313, no. 5793, pp. 1642–1645, 2006.

[14] J. Huisken, J. Swoger, F. Del Bene, J. Wittbrodt, and E. H. K. Stelzer, "Optical sectioning deep inside live embryos by selective plane illumination microscopy," *Science*, vol. 305, no. 5686, pp. 1007–1009, 2004.

[15] H. Siedentopf and R. Zsigmondy, "Über Sichtbarmachung und Größenbestimmung ultramikoskopischer Teilchen, mit besonderer Anwendung auf Goldrubingläser," *Annalen der Physik*, vol. 315, no. 1, pp. 1–39, 1902.

[16] P. J. Keller, A. D. Schmidt, J. Wittbrodt, and E. H. K. Stelzer, "Reconstruction of Zebrafish Early Embryonic Development by Scanned Light Sheet Microscopy," *Science*, vol. 322, pp. 1065–1069, Nov. 2008.

[17] Y. Wu, A. Ghitani, R. Christensen, A. Santella, Z. Du, G. Rondeau, Z. Bao, D. Colón-Ramos, and H. Shroff, "Inverted selective plane illumination microscopy (ispim) enables coupled cell identity lineaging and neurodevelopmental imaging in caenorhabditis elegans," *Proceedings of the National Academy of Sciences*, vol. 108, no. 43, pp. 17708–17713, 2011.

[18] T. A. Planchon, L. Gao, D. E. Milkie, M. W. Davidson, J. A. Galbraith, C. G. Galbraith, and E. Betzig, "Rapid three-dimensional isotropic imaging of living cells using Bessel beam plane illumination," *Nat Meth*, vol. 8, pp. 417–423, May 2011.

[19] L. Gao, L. Shao, C. D. Higgins, J. S. Poulton, M. Peifer, M. W. Davidson, X. Wu, B. Goldstein, and E. Betzig, "Noninvasive imaging beyond the diffraction limit of 3d dynamics in thickly fluorescent specimens," *Cell*, vol. 151, pp. 1370–1385, Dec. 2012.

[20] P. Paiè, F. Bragheri, A. Bassi, and R. Osellame, "Selective plane illumination microscopy on a chip," *Lab Chip*, vol. 16, pp. 1556–1560, 2016.

[21] W. Jahr, B. Schmid, C. Schmied, F. O. Fahrbach, and J. Huisken, "Hyperspectral light sheet microscopy," *Nature Communications*, vol. 6, p. 7990, Sep 2015.

[22] T. Chakraborty, M. K. Driscoll, E. Jeffery, M. M. Murphy, P. Roudot, B.-J. Chang, S. Vora, W. M. Wong, C. D. Nielson, H. Zhang, V. Zhemkov, C. Hiremath, E. D. De La Cruz, Y. Yi, I. Bezprozvanny, H. Zhao, R. Tomer, R. Heintzmann, J. P. Meeks, D. K. Marciano, S. J. Morrison, G. Danuser, K. M. Dean, and R. Fiolka, "Light-sheet microscopy of cleared tissues with isotropic, subcellular resolution," *Nature Methods*, vol. 16, pp. 1109–1113, Nov 2019.

[23] H. W. Babcock, "The Possibility of Compensating Astronomical Seeing," *Publications of the Astronomical Society of the Pacific*, vol. 65, no. 386, pp. 229–236, 1953.

[24] P. Kern, P. Lena, P. Gigan, J.-C. Fontanella, G. Rousset, F. Merkle, and J.-P. Gaffard, "Come-On: An Adaptive Optics Prototype Dedicated To Infrared Astronomy," in *New Technologies for Astronomy* (J.-P. Swings, ed.), vol. 1130, pp. 17 – 28, International Society for Optics and Photonics, SPIE, 1989.

[25] T. Boothe, L. Hilbert, M. Heide, L. Berninger, W. B. Huttner, V. Zaburdaev, N. L. Vastenhouw, E. W. Myers, D. N. Drechsel, and J. C. Rink, "A tunable refractive index matching medium for live imaging cells, tissues and model organisms," *eLife*, vol. 6, p. e27240, jul 2017.

[26] J. Swoger, P. Verveer, K. Greger, J. Huisken, and E. H. Stelzer, "Multi-view image fusion improves resolution in three-dimensional microscopy," *Opt. Express*, vol. 15, pp. 8029–8042, Jun 2007.

[27] S. Preibisch, S. Saalfeld, J. Schindelin, and P. Tomancak, "Software for bead-based registration of selective plane illumination microscopy data," *Nature methods*, vol. 7, pp. 418–9, 06 2010.

[28] U. Krzic, *Multiple-view microscopy with light-sheet based fluorescence microscope*. PhD thesis, Ruprecht-Karls-Universität Heidelberg, 2009.

[29] M. R. Young, "Principles and Technique of Fluorescence Microscopy," *Journal of Cell Science*, vol. s3-102, pp. 419–449, 12 1961.

[30] F. C. Zanacchi, P. Bianchini, and G. Vicidomini, "Fluorescence microscopy in the spotlight," *Microscopy Research and Technique*, vol. 77, pp. 479–482, July 2014.

[31] A. H. Coons, H. J. Creech, and R. N. Jones, "Immunological Properties of an Antibody Containing a Fluorescent Group," *Proceedings of the Society for Experimental Biology and Medicine*, vol. 47, no. 2, pp. 200–202, 1941.

[32] S. Inouye and F. I. Tsuji, "Aequorea green fluorescent protein: Expression of the gene and fluorescence characteristics of the recombinant protein," *FEBS Letters*, vol. 341, no. 2, pp. 277–280, 1994.

[33] M. Chalfie, Y. Tu, G. Euskirchen, W. W. Ward, and D. C. Prasher, "Green fluorescent protein as a marker for gene expression," *Science*, vol. 263, no. 5148, pp. 802–805, 1994.

[34] A. Jablonski, "Efficiency of anti-stokes fluorescence in dyes," *Nature*, vol. 131, pp. 839–840, Jun 1933.

[35] T. J. Lambert, "Fpbase: a community-editable fluorescent protein database," *Nature Methods*, vol. 16, pp. 277–278, Apr 2019.

[36] N. C. Shaner, R. E. Campbell, P. A. Steinbach, B. N. G. Giepmans, A. E. Palmer, and R. Y. Tsien, "Improved monomeric red, orange and yellow fluorescent proteins derived from discosoma sp. red fluorescent protein," *Nature Biotechnology*, vol. 22, pp. 1567–1572, Dec 2004.

[37] J. W. Lichtman and J.-A. Conchello, "Fluorescence microscopy," *Nature Methods*, vol. 2, pp. 910–919, Dec. 2005.

[38] D. Kromm, T. Thumberger, and J. Wittbrodt, "Chapter 5 - An eye on light-sheet microscopy," in *The Zebrafish* (H. W. Detrich, M. Westerfield, and L. I. Zon, eds.), vol. 133 of *Methods in Cell Biology*, pp. 105–123, Academic Press, 2016.

[39] M. Born and E. Wolf, *Principles of Optics: 60th Anniversary Edition*. Cambridge University Press, 7 ed., 2019.

[40] P. Török and F.-J. Kao, *Optical Imaging and Microscopy: Techniques and Advanced Systems*, vol. 87. Springer, Berlin, Heidelberg, 01 2003.

[41] G. Airy, "On the Diffraction of an Object Glass with Circular Aperture," *Transactions of the Cambridge Philosophical Society*, vol. 5, p. 283, 01 1835.

[42] L. R. F.R.S., "XXXI. Investigations in optics, with special reference to the spectroscope," *The London, Edinburgh, and Dublin Philosophical Magazine and Journal of Science*, vol. 8, no. 49, pp. 261–274, 1879.

[43] S. Grill and E. H. K. Stelzer, "Method to calculate lateral and axial gain factors of optical setups with a large solid angle," *J. Opt. Soc. Am. A*, vol. 16, pp. 2658–2665, Nov 1999.

[44] C. J. Engelbrecht and E. H. Stelzer, "Resolution enhancement in a light-sheet-based microscope (SPIM)," *Optics Letters*, vol. 31, pp. 1477–1479, May 2006.

[45] E. H. Stelzer and S. Lindek, "Fundamental reduction of the observation volume in far-field light microscopy by detection orthogonal to the illumination axis: confocal theta microscopy," *Optics Communications*, vol. 111, no. 5–6, pp. 536 – 547, 1994.

[46] T. A. Klar and S. W. Hell, "Subdiffraction resolution in far-field fluorescence microscopy," *Opt. Lett.*, vol. 24, pp. 954–956, Jul 1999.

[47] M. J. Rust, M. Bates, and X. Zhuang, "Sub-diffraction-limit imaging by stochastic optical reconstruction microscopy (storm)," *Nature Methods*, vol. 3, pp. 793–796, Oct 2006.

[48] Nobelprize.org, "The nobel prize in chemistry 2014," 2014. [accessed online on 15.08.2015].

[49] A. H. Voie, D. H. Burns, and F. A. Spelman, "Orthogonal-plane fluorescence optical sectioning: Three-dimensional imaging of macroscopic biological specimens," *Journal of Microscopy*, vol. 170, no. 3, pp. 229–236, 1993.

[50] J. Huisken, *Multi-view microscopy and multi-beam manipulation for high-resolution optical imaging*. PhD thesis, Albert-Ludwigs-Universität Freiburg im Breisgau, 2004.

[51] P. J. Keller and E. H. Stelzer, "Quantitative in vivo imaging of entire embryos with digital scanned laser light sheet fluorescence microscopy," *Current Opinion in Neurobiology*, vol. 18, no. 6, pp. 624–632, 2008.

[52] A. Maizel, D. von Wangenheim, F. Federici, J. Haseloff, and E. H. Stelzer, "High-resolution live imaging of plant growth in near physiological bright conditions using light sheet fluorescence microscopy," *The Plant Journal*, vol. 68, no. 2, pp. 377–385, 2011.

[53] J. Huisken and D. Y. R. Stainier, "Even fluorescence excitation by multidirectional selective plane illumination microscopy (mspim)," *Opt. Lett.*, vol. 32, pp. 2608–2610, Sep 2007.

[54] C. P. Newswire, "Bruker introduces dedicated light-sheet microscope for highly multiplexed 3d cell culture live imaging," 2019. [accessed online on 10.07.2021].

[55] U. Krzic, S. Gunther, T. E. Saunders, S. J. Streichan, and L. Hufnagel, "Multiview light-sheet microscope for rapid in toto imaging," *Nat Meth*, vol. 9, pp. 730–733, July 2012.

[56] R. Tomer, K. Khairy, F. Amat, and P. Keller, "Quantitative high-speed imaging of entire developing embryos with simultaneous multiview light-sheet microscopy," *Nature methods*, vol. 9, pp. 755–63, 06 2012.

[57] R. Chhetri, F. Amat, Y. Wan, B. Höckendorf, W. Lemon, and P. Keller, "Whole-animal functional and developmental imaging with isotropic spatial resolution," *Nature methods*, vol. 12, 10 2015.

[58] Y. Wu, P. Chandris, P. Winter, E. KIM, V. Jaumouillé, A. Kumar, M. Guo, J. LEUNG, C. Smith, I. REY-SUAREZ, H. Liu, C. Waterman-Storer, K. Ramamurthi, P. La Riviere, and H. SHROFF, "Simultaneous multiview capture and fusion improves spatial resolution in wide-field and light-sheet microscopy," *Optica*, vol. 3, pp. 897–910, 08 2016.

[59] J. D. Manton and E. J. Rees, "trispim: light sheet microscopy with isotropic super-resolution," *Optics Letters*, vol. 41, p. 4170, Sept. 2016.

[60] P. Strnad, S. Günther, J. Reichmann, U. Krzic, B. Balázs, G. Quintas Glasner de Medeiros, N. Norlin, T. Hiiragi, L. Hufnagel, and J. Ellenberg, "Inverted light-sheet microscope for imaging mouse pre-implantation development," *Nature methods*, vol. 13, 12 2015.

[61] A. Glaser, N. Reder, Y. Chen, C. Yin, L. Wei, S. Kang, L. Barner, W. Xie, E. McCarty, C. Mao, A. Halpern, C. Stoltzfus, J. Daniels, M. Gerner, P. Nicovich, J. Vaughan, L. True, and J. Liu, "Multi-immersion open-top light-sheet microscope for high-throughput imaging of cleared tissues," *Nature Communications*, vol. 10, 07 2019.

[62] A. Kumar, Y. Wu, R. Christensen, P. Chandris, W. Gandler, E. McCreedy, A. Bokinsky, D. A. Colón-Ramos, Z. Bao, M. McAuliffe, G. Rondeau, and H. Shroff, "Dual-view plane illumination microscopy for rapid and spatially isotropic imaging," *Nature protocols*, vol. 9, p. 2555—2573, November 2014.

[63] C. Dunsby, "Optically sectioned imaging by oblique plane microscopy," *Opt. Express*, vol. 16, pp. 20306–20316, Dec 2008.

[64] M. B. Bouchard, V. Voleti, C. S. Mendes, C. Lacefield, W. B. Grueber, R. S. Mann, R. M. Bruno, and E. M. C. Hillman, "Swept confocally-aligned planar excitation (scape) microscopy for high-speed volumetric imaging of behaving organisms," *Nature Photonics*, vol. 9, pp. 113–119, Feb 2015.

[65] E. Fuchs, J. Jaffe, R. Long, and F. Azam, "Thin laser light sheet microscope for microbial oceanography," *Opt. Express*, vol. 10, pp. 145–154, Jan 2002.

[66] L. A. Royer, W. C. Lemon, R. K. Chhetri, and P. J. Keller, "A practical guide to adaptive light-sheet microscopy," *Nature Protocols*, vol. 13, pp. 2462–2500, Nov 2018.

[67] K. McDole, L. Guignard, F. Amat, A. Berger, G. Malandain, L. A. Royer, S. C. Turaga, K. Branson, and P. J. Keller, "In toto imaging and reconstruction of post-implantation mouse development at the single-cell level," *Cell*, vol. 175, no. 3, pp. 859–876.e33, 2018.

[68] B.-C. Chen, W. R. Legant, K. Wang, L. Shao, D. E. Milkie, M. W. Davidson, C. Janetopoulos, X. S. Wu, J. A. Hammer, Z. Liu, B. P. English, Y. Mimori-Kiyosue, D. P. Romero, A. T. Ritter, J. Lippincott-Schwartz, L. Fritz-Laylin, R. D. Mullins, D. M. Mitchell, J. N. Bembenek, A.-C. Reymann, R. Bohme, S. W. Grill, J. T. Wang, G. Seydoux, U. S. Tulu, D. P. Kiehart, and E. Betzig, "Lattice light-sheet microscopy: Imaging molecules to embryos at high spatiotemporal resolution," *Science*, vol. 346, pp. 1257998–1257998, Oct. 2014.

[69] A. Alladin, L. Chaible, L. Garcia del Valle, R. Sabine, M. Loeschinger, M. Wachsmuth, J.-K. Hériché, C. Tischer, and M. Jechlinger, "Tracking cells in epithelial acini by light sheet microscopy reveals proximity effects in breast cancer initiation," *eLife*, vol. 9, p. e54066, jul 2020.

[70] R. McGorty, H. Liu, D. Kamiyama, Z. Dong, S. Guo, and B. Huang, "Open-top selective plane illumination microscope for conventionally mounted specimens," *Opt. Express*, vol. 23, pp. 16142–16153, Jun 2015.

[71] R. Mcgorty, D. Xie, and B. Huang, "High-na open-top selective-plane illumination microscopy for biological imaging," *Opt. Express*, vol. 25, pp. 17798–17810, Jul 2017.

[72] B. E. A. Saleh and M. C. Teich, *Fundamentals of Photonics (2nd Edition)*. Hoboken, New Jersey: John Wiley & Sons, Inc, 2007.

[73] G. Quintas Glasner de Medeiros, N. Norlin, S. Günther, M. Albert, L. Panavaite, U.-M. Fiuza, F. Peri, T. Hiiragi, U. Krzic, and L. Hufnagel, "Confocal multiview light-sheet microscopy," *Nature Communications*, vol. 6, p. 8881, 11 2015.

[74] T.-L. Liu, S. Upadhyayula, D. E. Milkie, V. Singh, K. Wang, I. A. Swinburne, K. R. Mosaliganti, Z. M. Collins, T. W. Hiscock, J. Shea, A. Q. Kohrman, T. N. Medwig, D. Dambournet, R. Forster, B. Cunniff, Y. Ruan, H. Yashiro, S. Scholpp, E. M. Meyerowitz, D. Hockemeyer, D. G. Drubin, B. L. Martin, D. Q. Matus, M. Koyama, S. G. Megason, T. Kirchhausen, and E. Betzig, "Observing the cell in its native state: Imaging subcellular dynamics in multicellular organisms," *Science*, vol. 360, no. 6386, 2018.

[75] B. Platt and R. Shack, "History and principles of shack-hartmann wavefront sensing," *Journal of refractive surgery (Thorofare, N.J. : 1995)*, vol. 17, no. 5, p. S573—7, 2001.

[76] T. V. Truong, W. Supatto, D. S. Koos, J. M. Choi, and S. E. Fraser, "Deep and fast live imaging with two-photon scanned light-sheet microscopy," *Nature Methods*, vol. 8, pp. 757–760, Sep 2011.

[77] F. Preusser, N. dos Santos, J. Contzen, H. Stachelscheid, r. T. Costa, P. Mergenthaler, and S. Preibisch, "Frc-qe: a robust and comparable 3d microscopy image quality metric for cleared organoids," *Bioinformatics*, vol. 37, pp. 3088–3090, 03 2021.

[78] B. Gul, S. Ashraf, S. Khan, H. Nisar, and I. Ahmad, "Cell refractive index: Models, insights, applications and future perspectives," *Photodiagnosis and Photodynamic Therapy*, vol. 33, p. 102096, 2021.

[79] Z. A. Steelman, W. J. Eldridge, J. B. Weintraub, and A. Wax, "Is the nuclear refractive index lower than cytoplasm? validation of phase measurements and implications for light scattering technologies," *Journal of Biophotonics*, vol. 10, no. 12, pp. 1714–1722, 2017.

[80] J. A. Kubby, *Adaptive optics for Biological imaging*. CRC press, 2013.

[81] J. Portilla and S. Barbero, "Accuracy of geometric point spread function estimation using the ray-counting method," in *Optical Systems Design 2012* (L. Mazuray, R. Wartmann, A. P. Wood, M. C. de la Fuente, J.-L. M. Tissot, J. M. Raynor, D. G. Smith, F. Wyrowski, A. Erdmann, T. E. Kidger, S. David, and P. Benítez, eds.), vol. 8550, pp. 12 – 23, International Society for Optics and Photonics, SPIE, 2012.

[82] M. SCHWERTNER, M. J. BOOTH, and T. WILSON, "Simulation of specimen-induced aberrations for objects with spherical and cylindrical symmetry," *Journal of Microscopy*, vol. 215, no. 3, pp. 271–280, 2004.

[83] J. V. Roey, J. van der Donk, and P. E. Lagasse, "Beam-propagation method: analysis and assessment," *J. Opt. Soc. Am.*, vol. 71, pp. 803–810, Jul 1981.

[84] F. O. Fahrbach, P. Simon, and A. Rohrbach, "Microscopy with self-reconstructing beams," *Nat Photon*, vol. 4, pp. 780–785, Nov. 2010.

[85] M. Weigert, K. Subramanian, S. T. Bundschuh, E. W. Myers, and M. Kreysing, "Biobeam—multiplexed wave-optical simulations of light-sheet microscopy," *PLOS Computational Biology*, vol. 14, pp. 1–11, 04 2018.

[86] G. de Medeiros, D. Kromm, B. Balazs, N. Norlin, S. Günther, E. Izquierdo, P. Ronchi, S. Komoto, U. Krzic, Y. Schwab, F. Peri, S. de Renzis, M. Leptin, M. Rauzi, and L. Hufnagel, "Cell and tissue manipulation with ultrashort infrared laser pulses in light-sheet microscopy," *Scientific Reports*, vol. 10, p. 1942, Feb 2020.

[87] C. Shannon, "Communication in the Presence of Noise," *Proceedings of the IRE*, vol. 37, pp. 10–21, jan 1949.

[88] U. Krämer, "The natural history of model organisms: Planting molecular functions in an ecological context with *Arabidopsis thaliana*," *eLife*, vol. 4, p. e06100, mar 2015.

[89] F. Laibach, "Arabidopsis thaliana (l.) heynh. als objekt für genetische und entwicklungsphysiologische untersuchungen," *Bot. Archiv*, vol. 44, pp. 439–455, 1943.

[90] L. Dolan, K. Janmaat, V. Willemsen, P. Linstead, S. Poethig, K. Roberts, and B. Scheres, "Cellular organisation of the Arabidopsis thaliana root," *Development*, vol. 119, pp. 71–84, 09 1993.

[91] D. J. Cosgrove, "How do plant cell walls extend?," *Plant Physiology*, vol. 102, pp. 1–6, 05 1993.

[92] H. W. Gausman, W. A. Allen, and D. E. Escobar, "Refractive index of plant cell walls," *Appl. Opt.*, vol. 13, pp. 109–111, Jan 1974.

[93] J. Gierten, C. Pylatiuk, O. T. Hammouda, C. Schock, J. Stegmaier, J. Wittbrodt, J. Gehrig, and F. Loosli, "Automated high-throughput heartbeat quantification in medaka and zebrafish embryos under physiological conditions," *Scientific Reports*, vol. 10, p. 2046, Feb 2020.

[94] C. Q. Lischik, L. Adelmann, and J. Wittbrodt, "Enhanced in vivo-imaging in medaka by optimized anaesthesia, fluorescent protein selection and removal of pigmentation," *PLOS ONE*, vol. 14, pp. 1–19, 03 2019.

[95] J. Reichmann, B. Nijmeijer, M. J. Hossain, M. Eguren, I. Schneider, A. Z. Politi, M. J. Roberti, L. Hufnagel, T. Hiiragi, and J. Ellenberg, "Dual-spindle formation in zygotes keeps parental genomes apart in early mammalian embryos," *Science*, vol. 361, no. 6398, pp. 189–193, 2018.

[96] J. A. Rivera-Pérez, V. Jones, and P. P. Tam, "Chapter 11 - Culture of Whole Mouse Embryos at Early Postimplantation to Organogenesis Stages: Developmental Staging and Methods," in *Guide to Techniques in Mouse Development, Part A: Mice, Embryos, and Cells, 2nd Edition* (P. M. Wassarman and P. M. Soriano, eds.), vol. 476 of *Methods in Enzymology*, pp. 185–203, Academic Press, 2010.

[97] D. Sweeton, S. Parks, M. Costa, and E. F. Wieschaus, "Gastrulation in drosophila: the formation of the ventral furrow and posterior midgut invaginations.," *Development*, vol. 112 3, pp. 775–89, 1991.

[98] Z. Kam, J. Minden, D. Agard, J. Sedat, and M. Leptin, "Drosophila gastrulation: analysis of cell shape changes in living embryos by three-dimensional fluorescence microscopy," *Development*, vol. 112, pp. 365–370, 06 1991.

[99] M. Mavrakis, R. Rikhy, M. Lilly, and J. Lippincott-Schwartz, "Fluorescence imaging techniques for studying drosophila embryo development," *Current Protocols in Cell Biology*, vol. 39, no. 1, pp. 4.18.1–4.18.43, 2008.

[100] M. Rauzi, U. Krzic, T. E. Saunders, M. Krajnc, P. Ziherl, L. Hufnagel, and M. Leptin, "Embryo-scale tissue mechanics during drosophila gastrulation movements," *Nature communications*, vol. 6, no. 1, pp. 1–12, 2015.

[101] S. Bhide, D. Gombalova, G. Mönke, J. Stegmaier, V. Zinchenko, A. Kreshuk, J. M. Belmonte, and M. Leptin, "Mechanical competition alters the cellular interpretation of an endogenous genetic program," *Journal of Cell Biology*, vol. 220, 08 2021. e202104107.

[102] J. Chu, R. D. Haynes, S. Y. Corbel, P. Li, E. González-González, J. S. Burg, N. J. Ataie, A. J. Lam, P. J. Cranfill, M. A. Baird, M. W. Davidson, H.-L. Ng, K. C. Garcia, C. H. Contag, K. Shen, H. M. Blau, and M. Z. Lin, "Non-invasive intravital imaging of cellular differentiation with a bright red-excitable fluorescent protein," *Nature Methods*, vol. 11, pp. 572–578, May 2014.

[103] S. Aldaz, L. M. Escudero, and M. Freeman, "Live imaging of drosophila imaginal disc development," *Proceedings of the National Academy of Sciences*, vol. 107, no. 32, pp. 14217–14222, 2010.

[104] C. Vinegoni, C. Pitsouli, D. Razansky, N. Perrimon, and V. Ntziachristos, "In vivo imaging of drosophila melanogaster pupae with mesoscopic fluorescence tomography," *Nature Methods*, vol. 5, pp. 45–47, Jan 2008.

[105] R. E. Ward, P. Reid, A. Bashirullah, P. P. D'Avino, and C. S. Thummel, "GFP in living animals reveals dynamic developmental responses to ecdysone during drosophila metamorphosis," *Developmental Biology*, vol. 256, no. 2, pp. 389–402, 2003.

[106] A. Arranz, D. Dong, S. Zhu, C. Savakis, J. Tian, and J. Ripoll, "In-vivo optical tomography of small scattering specimens: time-lapse 3d imaging of the head eversion process in drosophila melanogaster," *Scientific Reports*, vol. 4, p. 7325, Dec 2014.

[107] S. P. Bainbridge and M. Bownes, "Staging the metamorphosis of Drosophila melanogaster," *Development*, vol. 66, pp. 57–80, 12 1981.

[108] J. Schindelin, I. Arganda-Carreras, E. Frise, V. Kaynig, M. Longair, T. Pietzsch, S. Preibisch, C. Rueden, S. Saalfeld, B. Schmid, J.-Y. Tinevez, D. J. White, V. Hartenstein, K. Eliceiri, P. Tomancak, and A. Cardona, "Fiji: an open-source platform for biological-image analysis," *Nature Methods*, vol. 9, pp. 676–682, Jul 2012.

[109] C. R. Harris, K. J. Millman, S. J. van der Walt, R. Gommers, P. Virtanen, D. Cournapeau, E. Wieser, J. Taylor, S. Berg, N. J. Smith, R. Kern, M. Picus, S. Hoyer, M. H. van Kerkwijk, M. Brett, A. Haldane, J. F. del Río, M. Wiebe, P. Peterson, P. Gérard-Marchant, K. Sheppard, T. Reddy, W. Weckesser, H. Abbasi, C. Gohlke, and T. E. Oliphant, "Array programming with NumPy," *Nature*, vol. 585, pp. 357–362, Sept. 2020.

[110] E. Jones, T. Oliphant, P. Peterson, *et al.*, "SciPy: Open source scientific tools for Python," 2001–.

[111] I. Schneider, M. de Ruijter-Villani, M. J. Hossain, T. A. Stout, and J. Ellenberg, "Dual spindles assemble in bovine zygotes despite the presence of paternal centrosomes," *Journal of Cell Biology*, vol. 220, 09 2021. e202010106.

[112] L. A. Barner, A. K. Glaser, H. Huang, L. D. True, and J. T. C. Liu, "Multi-resolution open-top light-sheet microscopy to enable efficient 3d pathology workflows," *Biomed. Opt. Express*, vol. 11, pp. 6605–6619, Nov 2020.

[113] EMBL, "Embl spin-off company luxendo acquired by bruker," 2017. [accessed online on 10.07.2021].

[114] D. Serra, U. Mayr, A. Boni, I. Lukonin, M. Rempfler, L. Meylan, M. Stadler, P. Strnad, P. Papasaikas, D. Vischi, A. Waldt, G. Roma, and P. Liberali, "Self-organization and symmetry breaking in intestinal organoid development," *Nature*, vol. 569, pp. 1–7, 05 2019.

[115] S. by Venturelab Ltd., "Viventis microscopy sàrl - light sheet microscope systems for long-term live-imaging.," 2017. [accessed online on 11.07.2021].

[116] S. Preibisch, F. Amat, E. Stamataki, M. Sarov, R. Singer, E. Myers, and P. Tomancak, "Efficient bayesian-based multiview deconvolution," *Nature methods*, vol. 11, 04 2014.

[117] B. Schmid and J. Huisken, "Real-time multi-view deconvolution," *Bioinformatics*, vol. 31, pp. 3398–3400, 06 2015.

[118] B. Balázs, *A new angle on light-sheet microscopy and real-time image processing*. PhD thesis, Pázmány Péter Catholic University, Budapest, 2018.

[119] T. Vettenburg, H. Dalgarno, J. Nylk, C. Coll-Lladó, D. Ferrier, T. Čižmár, F. Gunn-Moore, and K. Dholakia, "Light-sheet microscopy using an airy beam," *Nature methods*, vol. 11, 04 2014.

[120] A. Chmielewski, A. Kyrsting, P. Mahou, M. Wayland, L. Muresan, J. F. Evers, and C. Kaminski, "Fast imaging of live organisms with sculpted light sheets," *Scientific Reports*, vol. 5, 04 2015.

[121] L. Gao, "Extend the field of view of selective plan illumination microscopy by tiling the excitation light sheet," *Opt. Express*, vol. 23, pp. 6102–6111, Mar 2015.

[122] K. M. Dean and R. Fiolka, "Uniform and scalable light-sheets generated by extended focusing," *Opt. Express*, vol. 22, pp. 26141–26152, Oct 2014.

[123] M. Duocastella, B. Sun, and C. B. Arnold, "Simultaneous imaging of multiple focal planes for three-dimensional microscopy using ultra-high-speed adaptive optics," *Journal of Biomedical Optics*, vol. 17, no. 5, pp. 1 – 4, 2012.

[124] T.-H. Chen, J. Ault, H. Stone, and C. Arnold, "High-speed axial-scanning wide-field microscopy for volumetric particle tracking velocimetry," *Experiments in Fluids*, vol. 58, 04 2017.

[125] W. Zong, J. Zhao, X. Chen, Y. Lin, H. Ren, Y. Zhang, M. Fan, Z. Zhou, H. Cheng, Y. Sun, and L. Chen, "Large-field high-resolution two-photon digital scanned light-sheet microscopy," *Cell research*, vol. 25, 09 2014.

[126] R. Power and J. Huisken, "Adaptable, illumination patterning light sheet microscopy," *Scientific Reports*, vol. 8, 06 2018.

[127] E. McLeod, A. B. Hopkins, and C. B. Arnold, "Multiscale bessel beams generated by a tunable acoustic gradient index of refraction lens," *Opt. Lett.*, vol. 31, pp. 3155–3157, Nov 2006.

[128] E. McLeod and C. B. Arnold, "Optical analysis of time-averaged multiscale bessel beams generated by a tunable acoustic gradient index of refraction lens," *Appl. Opt.*, vol. 47, pp. 3609–3618, Jul 2008.

[129] J. Li, F. Xue, and T. Blu, "Fast and accurate three-dimensional point spread function computation for fluorescence microscopy," *J. Opt. Soc. Am. A*, vol. 34, pp. 1029–1034, Jun 2017.

[130] F. O. Fahrbach, F. F. Voigt, B. Schmid, F. Helmchen, and J. Huisken, "Rapid 3d light-sheet microscopy with a tunable lens," *Opt. Express*, vol. 21, pp. 21010–21026, Sep 2013.

[131] I. Sbalzarini and P. Koumoutsakos, "Feature point tracking and trajectory analysis for video imaging in cell biology," *Journal of Structural Biology*, vol. 151, no. 2, pp. 182–195, 2005.

[132] S. Pertuz, D. Puig, and M. A. Garcia, "Analysis of focus measure operators for shape-from-focus," *Pattern Recognition*, vol. 46, no. 5, pp. 1415–1432, 2013.

[133] D. M. Chandler, "Seven challenges in image quality assessment: Past, present, and future research," *ISRN Signal Processing*, vol. 2013, p. 905685, Feb 2013.